



Title	The Nature of Ultralong C–C Bonds : Demonstration of the Longest Csp ³ –Csp ³ Single Bond beyond 1.8 Å and Discovery of Flexible Covalent Bonds
Author(s)	SHIMAJIRI, Takuya
Citation	北海道大学. 博士(理学) 甲第14902号
Issue Date	2022-03-24
DOI	10.14943/doctoral.k14902
Doc URL	http://hdl.handle.net/2115/85243
Type	theses (doctoral)
File Information	SHIMAJIRI_Takuya.pdf



[Instructions for use](#)

Doctoral Dissertation

**The Nature of Ultralong C–C Bonds: Demonstration
of the Longest Csp^3 – Csp^3 Single Bond beyond 1.8 Å
and Discovery of Flexible Covalent Bonds**

(極度に長い C–C 結合の性質：1.8 Å を超える世界最長の
 Csp^3 – Csp^3 単結合の実証と共有結合の柔軟性の発見)

Takuya SHIMAJIRI

Graduate School of Chemical Sciences and Engineering,
Hokkaido University

2022

Table of Contents

Chapter 1.

General Introduction

1-1. C–C Covalent Bond	5
1-2. Unusual Bonding Interaction	7
1-3. Short and Long C–C Single Bond	8
1-5. Contents of This Dissertation	11
1-4. References	13

Chapter 2.

Creation and Demonstration of the Longest C–C Single Bond with a Bond Length beyond 1.8 Å

2-1. Introduction	16
2-2. Results and Discussion	
2-2-1. Design Concept	17
2-2-2. Theoretical Examination for Molecular Design	19
2-2-3 Preparation of hydrocarbon 1a-1c	23
2-2-4. Raman Spectroscopy	24
2-2-5. Experimentally Determined Bond Length by X-Ray Analyses	26
2-2-6. Stability of the Hydrocarbon 1c with a Very Weak C–C Bond	29
2-2-7. Theoretical analysis for the nature of ultralong C–C single bond	32
2-3. Conclusion	35
2-4. Experimental Section	
General Procedures	36
Preparation	38
X-ray analyses	43
2-5. References	49

Chapter 3.

Discovery of Flexible Bonds Based on an Extremely Elongated C–C Single Bond

3-1. Introduction	52
3-2. Results and Discussion	
3-2-1. Intramolecular Photocyclization	54
3-2-2. Theoretical study	59
3-2-3. Single-Crystal-to-Single-Crystal Transformation	60
3-2-4. Redox Behavior	62
3-3. Conclusion	68
3-4. Experimental Section	
General Procedures	69
Preparation	70
X-ray analyses	83
3-5. References	88
Acknowledgments	92

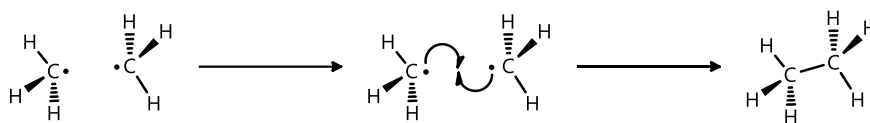
Chapter 1

General Introduction

1-1. C–C Covalent Bond

Organic chemists are studying on the organic compound, which is basically defined as the molecule containing one or more carbon (C) atom(s), excluding carbon oxides (CO and CO₂), inorganic cyanides (XCN), and carbonates (X_nCO₃). Such organic compounds are mainly constructed by covalent bonds between atoms. Covalent bond, in which two atoms are connected by sharing two electrons, is a class of chemical bonding, as proposed by Lewis (Scheme 1). Then, Pauling systematized the chemical bond theory including covalent bond.^[1] Currently, covalent bond is interpreted as "a region of relatively high electron density between nuclei which arises at least partly from sharing of electrons and gives rise to an attractive force and characteristic internuclear distance" by IUPAC.^[2]

Scheme 1. C–C covalent bond



In this context, the C–C covalent bond is the most basic concept of organic compounds. In general, carbon atom has an electronic configuration of $[1s]^2[2s]^2[2p]^2$, and the four valence electrons in $2s$ and $2p$ orbitals of carbon atom are involved in chemical bond and reactions. By promotion of an electron from $2s$ orbital to $2p$ orbital, the valence state was formed, and then $2s$ and $2p$ orbitals are hybridized to make new orbitals (hybridized orbital). By the formation of hybridized orbitals, there are three types of C–C covalent bond such as C–C single bond, C=C double bond and C≡C triple bond (Figure 1). Depending on the bonding manners, these electron states of carbon atoms are described as follows; sp^3 hybridization for C–C single bond, sp^2 hybridization for C=C double bond and sp hybridization for C≡C triple bond, corresponding to the ratio between s -orbital and p -orbitals (e.g., sp^3 ; s -orbital character : p -orbital character = 1 : 3). When two hybridized C atoms are closing to each other, they form a strong bond overlapped by a head-on manner along the axis of the atoms, called σ -bond. In the case of sp^2 - or sp -hybridization, unhybridized p -orbitals still remain, so that they are interacting with each other by sideways overlap to form a second or third bond (π -bond). The electrons in a σ -bond occupy the central region between nuclei, while the electrons in a π -bond occupy the regions on either side of a line between nuclei. Due to the large overlap integral of σ -bond, bonding energy of the σ -bond is larger than that of π -bond.

With regard to the structural parameters, the standard bond length is 1.54 Å for C–C single bond with sp^3 hybridization, 1.33 Å for C=C double bond with sp^2 hybridization and 1.20 Å for C≡C triple bond with sp hybridization. The C=C double bond and C≡C triple bond often show expansion or contraction since the π -bond is sensitive to the electronic environment around the bond. However, the C–C single bond does not change because deviation from the standard causes a large loss of bonding energy.

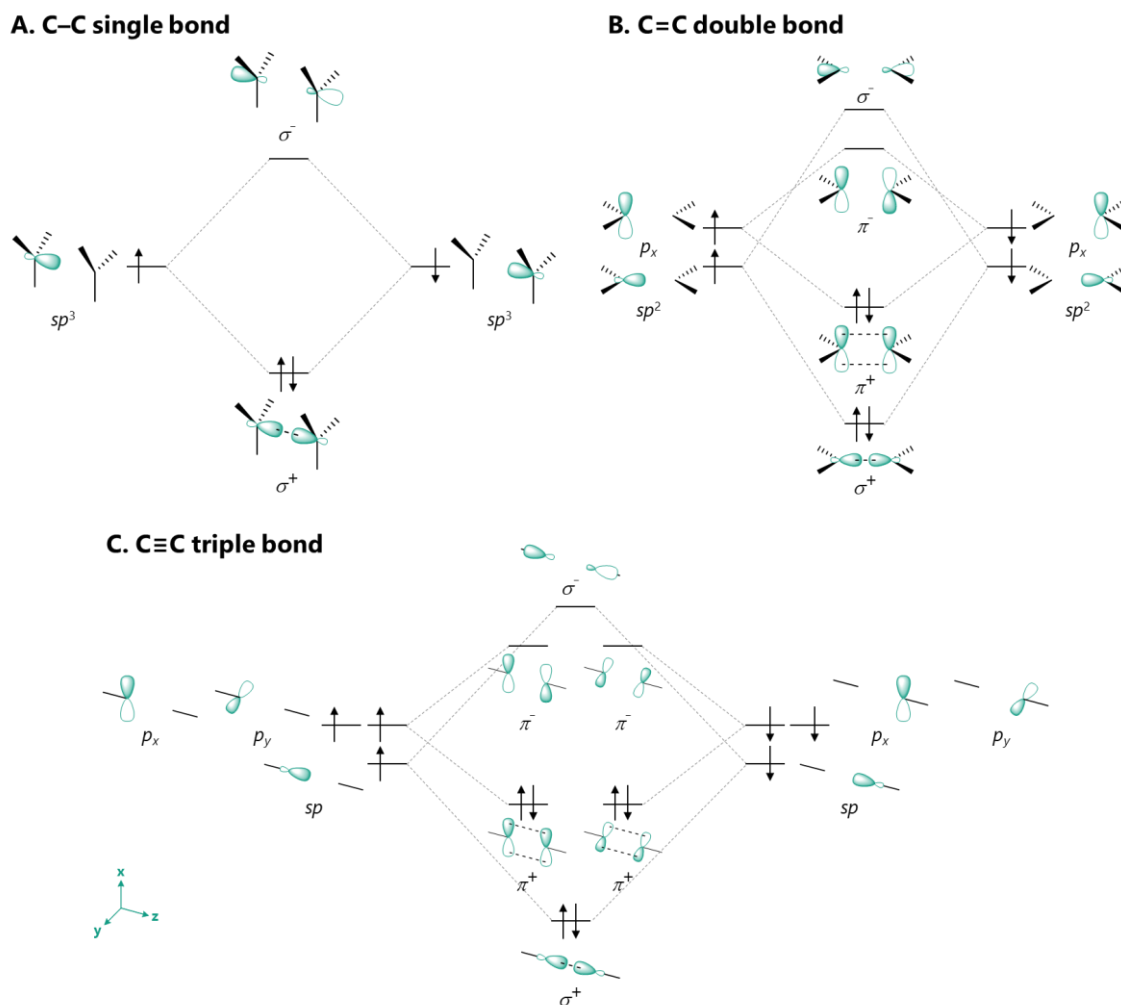


Figure 1. Energy diagram of C–C covalent bond.

1-2. Unusual Bonding Interaction

As mentioned above, the structural parameters such as bond length, bond angle, and torsion angle among carbon atoms are nearly constant on the basis of their hybrid orbitals (Figure 2). On the other hand, unusual geometrical parameters have been reported for highly strained molecules, such as sterically congested and/or curved polycyclic aromatic hydrocarbons^[3–10] as well as cyclic π -conjugated molecules, including cycloparaphenylenes,^[11–19] which are endowed with special properties that the ordinary hydrocarbons do not have.

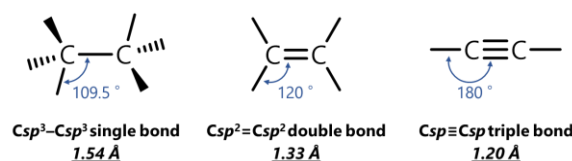


Figure 2. Standard bond length and bond angles of C–C bonds.

In terms of the C–C bond, several attempts have been taken to make molecules with an unusual chemical bonding. For example, some molecules such as cyclic 1,3-diyl diradical were reported to have the π -single bonding without σ -bond, although C–C single bond is basically constructed by σ -bond. (Figure 2).^[20–22]

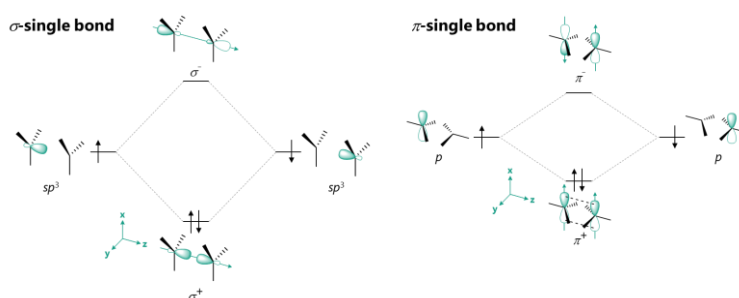


Figure 2. Energy diagram of σ - and π -single bonding.

From another point of view, atoms such as carbon obey the octet rule and can make four covalent bonds with two electrons in each bond. However, some atoms can form more than four bonds, which are known as hypervalent bond. Actually, such bond is well-studied in compounds containing heavier main-group elements, but very rare in carbon-based compounds. Akiba and Yamamoto *et. al.* reported that the anthracene derivatives have the pentacoordinate and hexacoordinate carbocations (Figure 3).^[23–25] These results are supported by X-ray analyses and theoretical study.

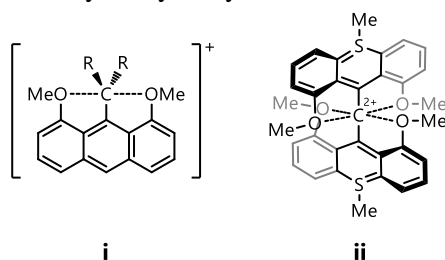


Figure 3. Compounds with hypervalent pentacoordinate or hexacoordinate carbon atom.

1-3. Short and Long C–C Single Bond

The Csp^3-Csp^3 single bond length is generally 1.54 Å, as in the case of ethane. This standard bond length is observed in almost all compounds.^[26] On the other hand, strained compounds may exhibit unusual bonding states. For example, cyclopropane, an equilateral triangular-shaped cyclic hydrocarbon, has the bond angle of 60°, which is far different from the ideal bond angle around Csp^3 atom (109.5°), and the distance between the carbon atoms is 1.51 Å (Figure 4).^[27] This is because the orbital of the C–C bonds is distributed out of the three-membered ring, resulting in a bent shape of the bond, which is called as the bent bond or the banana bond. As a result, the *s*-character (25%) of the C–C bond of cyclopropane is depleted to 18%, which is corresponding to " $sp^{4.5}$ " hybridization. On the other hand, the hybridization of the C–H bond outside the ring is expressed as " sp^2 ", which results in shorter C–H bond.

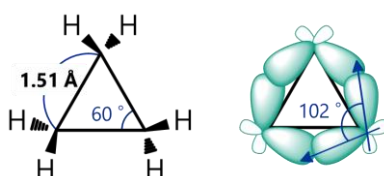


Figure 4. Bond length, bond angle and bond orbitals of cyclopropane.

By using this strategy shortening the bond outside of the ring structure, unusual short C1–C2 bond has been reported in the dimer of tetrahydrones **iii** regarded as a cluster of cyclopropanes with caged structure (Figure 5).^[28] In addition, contracted bond has been also achieved by steric compression of the C–C bond in caged molecule **iv**.^[29] Despite the approximately 0.1 Å contraction of the C–C single bond, both C1 and C2 atoms still form four covalent bonds.

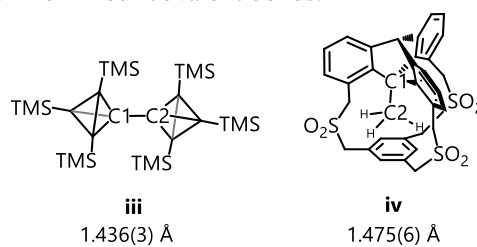


Figure 5. Examples of the molecule with short C-C bond.

In contrast, a longer C1–C2 bond was predicted for hexaphenylethane (HPE) **v** as a result of large steric repulsion among its six phenyl groups.^[30] However, the parent HPE **v** is not stable because of facile fission of the C1–C2 bond to generate two triphenylmethyl radicals, which finally produces the *α,p*-dimer, the more stable isomer of HPE (Figure 6).^[31]

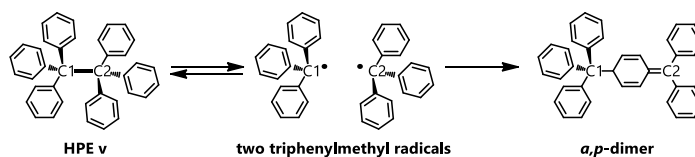


Figure 6. The isomerization mechanism of HPE **v**.

By preventing α,p -dimer formation, Mislow *et al.* obtained HPE derivative **vi** with bulky *tert*-butyl groups, which is in equilibrium with the bond-dissociated triarylmethyl radical in solution. The length of the C1–C2 bond (d_I) was determined to be 1.67(3) Å by an X-ray crystal structural analysis.^[32] Schreiner *et al.* indicated that bulky *tert*-butyl groups not only suppress the isomerization from partially generated bond cleavage species by Pauli repulsion but also increase thermodynamic stabilization of bonded species by van der Waals dispersion interaction (Figure 7).^[33,34]

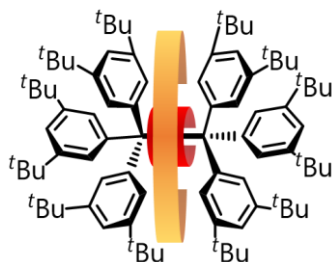


Figure 7. Pauli repulsion (red) and dispersion effect (orange) around the C1–C2 of HPE **vi**.

Although methano[10]annulene (bisorcaradiene)^[35] and anthracene-based [2,2]paracyclophane^[36] have been reported to have much longer C–C bonds, those values were later proven to be artifacts because of the coexistence of a bond-dissociated valence isomer. Herges *et al.*^[37] and Toda *et al.*^[38] synthesized **vii** and **viii**, which can be regarded as stabilized HPE derivatives that do not undergo valence isomerization (Figure 8). They are stable compounds because C1–C2 bond fission is suppressed due to sharing of two benzene rings of the HPE framework despite much greater d_I values [1.713(2) and 1.734(5) Å, respectively] than in HPE **vi**. The author's group has reported that fused-type HPEs **ix–xi** have an elongated C–C single bond. Especially, dispiro(acridan)-substituted pyracene (**DSAP**) exhibits the greatest value of the bond length [1.791(3) Å] at 413 K in a single crystal. Not only the HPE-type hydrocarbon **vii** but also caged-alkane dimers can possess an expanded bond, as demonstrated by Schreiner *et al.*^[39] A d_I value of 1.704(4) Å has been reported for the cross-dimer of triamantane with diamantane **xii**. For these caged-alkane dimers, bond dissociation was hampered by attractive dispersion interactions,^[39,40] and the dimers are stable even at high temperature. Theoretical calculations for these alkane dimers suggested that there is a certain limit for d_I (1.803 Å),^[41] because bond dissociation energy (BDE) becomes zero when the two carbon nuclei are separated beyond this distance. The data analysis for relationship between C–C single bond length and BDE also predicted the limit of C–C single bond [1.748 Å].^[42] In contrast, the shortest non-bonded C···C contact [1.80(2) Å] was observed in [1.1.1]propellane analogue **xiii**.^[43]

Thus, on the surface, it seems impossible to synthesize a stable hydrocarbon with a bond of d_I beyond 1.8 Å. Very recently, the molecules with a bond length beyond 1.9 Å have been reported. For instance, diaminocarborane **xiv** contains a C–C three-center two-electron (3c-2e) bonding with a bond length of 1.932(2) Å. In hydrocarbon **xv**, a bonding interaction beyond 2.0 Å consisting of two *p*-orbitals of

C1 and C2 was observed by Kubo *et. al.* However, these examples are not considered as the pure Csp^3-Csp^3 single bond composed of two electrons, and thus the nature of an extremely elongated Csp^3-Csp^3 single bond is unclarified yet.

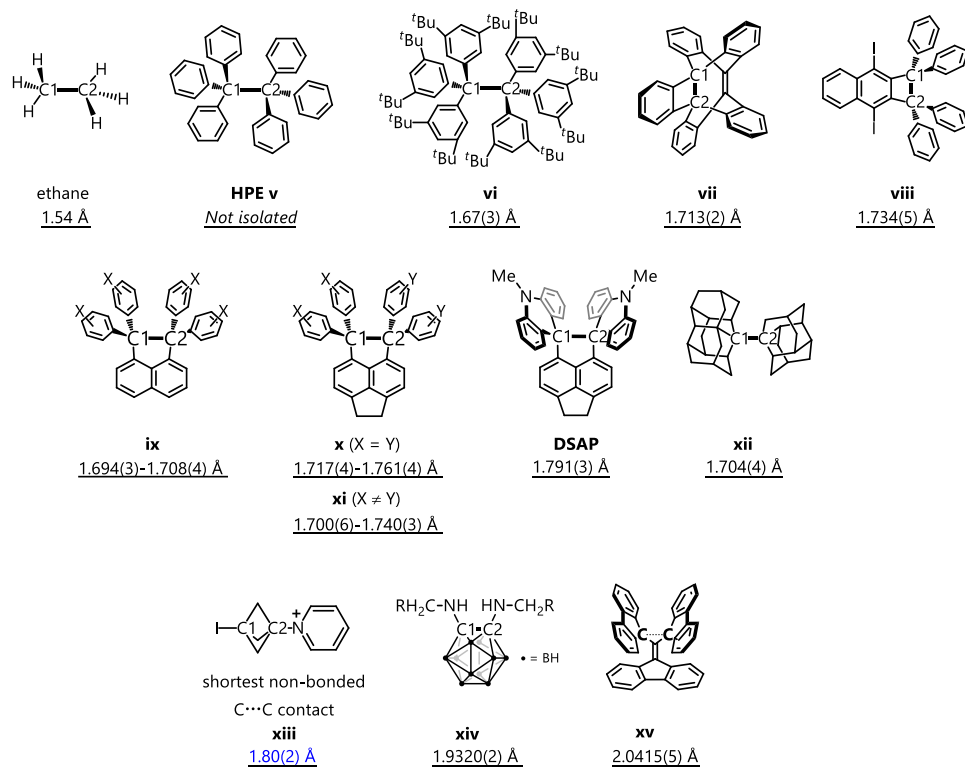


Figure 8. Examples with an unusual distance between C1 and C2 atoms.

1-4. Contents of This Dissertation

In chapter 1, the author described the feature of the covalent bond related to carbon atoms. Chemical bonding is one of the most fundamental concepts in organic chemistry. The elucidation of its nature is important in further understanding of chemical phenomena. Previously, several attempts have been taken to prepare the molecules with an unusual chemical bonding. Focusing on the expansion of C–C single bond, a few examples with a bond length beyond 1.7 Å have been reported. However, the Csp^3-Csp^3 bond length beyond 1.8 Å, which is the limit predicted by theoretical study,^[41,42] is still unexplored area. In this dissertation, the author focuses on the creation and demonstration of the C–C single bond beyond 1.8 Å and on discovery of its unique nature.

In chapter 2, the author succeeded in the synthesis of a series of dispiro(dibenzocycloheptatriene)-type HPE derivatives **1a-1c** with an extremely expanded C–C single bond based on the intramolecular core-shell strategy. Among these spiro-DBCHT, **1c** has the hyper covalent bond with a bond length beyond 1.8 Å, and the presence of the ultralong bond was demonstrated by Raman spectroscopy and X-ray analysis (Figure 9). The accurately determined bond length [1.806(2) Å] was greater than both the shortest non-bonded C··C contact [1.80(2) Å]^[43] and the theoretically predicted limit for C–C single bond (1.803 Å)^[41], indicating that the long-assumed linear correlation between bond length and BDE for covalent bond is invalid in greater bond lengths. The extensive theoretical studies identified that an extremely elongated C–C bond of **1a-1c** has a small bond index but keeps pure σ -bonded character with two electrons. Therefore, the covalently bonded state and non-bonded state would be seamlessly connected in terms of the interatomic distance.

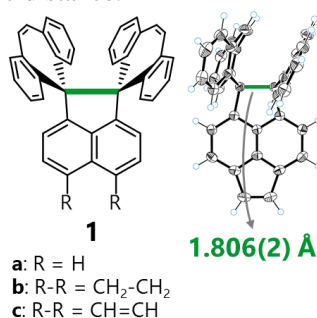


Figure 9. ORTEP drawing of spiro-DBCHT **1c** at 400 K.

In chapter 3, the author considered that such an extremely elongated bond should be endowed a unique bond flexibility. Thus, the author focused on the interconversion between spiro-DBCHT **1** and caged molecules **2** induced by light and heat. As a result, unprecedented and reversible bond expansion and contraction were observed by formation and cleavage of the cyclobutane ring (Figure 10). Since formation of the cyclobutane ring and contraction of the C–C bond induce lowering of the HOMO level, oxidative properties can be deactivated and activated by light and heat. Furthermore, single-

crystal to single-crystal transformation of **1b** and **2b** upon photoirradiation and heating was accomplished because of similarity of crystal packing and lattice parameters, leading to detailed analyses of intermediates to visualize the unprecedented expansion and contraction of the elongated C–C bond.

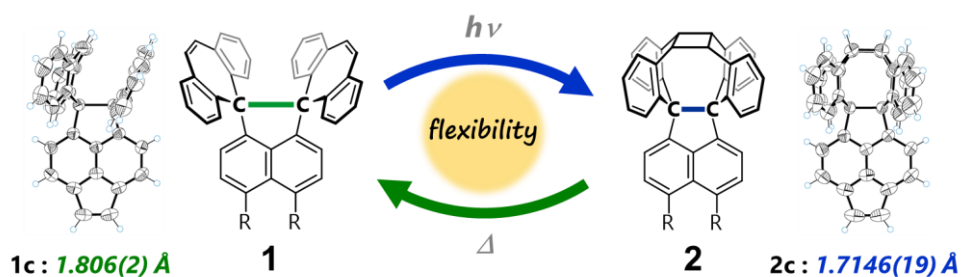


Figure 10. Interconversion between spiro-DBCHT **1** and caged molecule **2**.

In this dissertation, the author has investigated the nature of ultralong Csp^3 – Csp^3 bonds beyond 1.8 Å by experimental and theoretical study, and revealed that such C–C bonds exhibit flexibility, which is a new facet of covalent bonds.

3-5. References

- [1] L. Pauling, *The Nature of the Chemical Bond, 3rd Ed.*, Cornell University Press, Ithaca, NY, **1960**.
- [2] *Compendium of Chemical Terminology Gold Book*, International Union Of Pure And Applied Chemistry, **2014**.
- [3] J. Lu, D. M. Ho, N. J. Vogelaar, C. M. Kraml, R. A. Pascal, *J. Am. Chem. Soc.* **2004**, *126*, 11168–11169.
- [4] C. N. Feng, M. Y. Kuo, Y. T. Wu, *Angew. Chem. Int. Ed.* **2013**, *52*, 7791–7794.
- [5] Y. Sakamoto, T. Suzuki, *J. Am. Chem. Soc.* **2013**, *135*, 14074–14077.
- [6] H. Kashiwara, T. Asada, K. Kamikawa, *Chem. - A Eur. J.* **2015**, *21*, 6523–6527.
- [7] T. Fujikawa, Y. Segawa, K. Itami, *J. Am. Chem. Soc.* **2015**, *137*, 7763–7768.
- [8] X. Gu, H. Li, B. Shan, Z. Liu, Q. Miao, *Org. Lett.* **2017**, *19*, 2246–2249.
- [9] Y. T. Wu, J. S. Siegel, *Chem. Rev.* **2006**, *106*, 4843–4867.
- [10] A. Sygula, P. W. Rabideau, in *Carbon-Rich Compd.* (Eds.: M. Haley., R. Tykwinski.), Wiley-VCH Verlag GmbH & Co. KGaA, Weinheim, FRG, **2006**, pp. 529–565.
- [11] S. Yamago, E. Kayahara, T. Iwamoto, in *Chem. Rec.*, John Wiley And Sons Inc., **2014**, pp. 84–100.
- [12] T. Iwamoto, E. Kayahara, N. Yasuda, T. Suzuki, S. Yamago, *Angew. Chem. Int. Ed.* **2014**, *53*, 6430–6434.
- [13] E. R. Darzi, R. Jasti, *Chem. Soc. Rev.* **2015**, *44*, 6401–6410.
- [14] P. Li, L. N. Zakharov, R. Jasti, *Angew. Chem. Int. Ed.* **2017**, *56*, 5237–5241.
- [15] H. Isobe, T. Suenaga, Z. Sun, M. Kotani, P. Sarkar, S. Sato, *Proc. Natl. Acad. Sci.* **2016**, *113*, 8109–8114.
- [16] K. Ikemoto, R. Kobayashi, S. Sato, H. Isobe, *Angew. Chem. Int. Ed.* **2017**, *56*, 6511–6514.
- [17] S. Hitosugi, S. Sato, T. Matsuno, T. Koretsune, R. Arita, H. Isobe, *Angew. Chem. Int. Ed.* **2017**, *56*, 9106–9110.
- [18] Y. Segawa, A. Yagi, K. Matsui, K. Itami, *Angew. Chem. Int. Ed.* **2016**, *55*, 5136–5158.
- [19] G. Povie, Y. Segawa, T. Nishihara, Y. Miyauchi, K. Itami, *Science* **2017**, *356*, 172–175.
- [20] S. L. Buchwalter, G. L. Closs, *J. Am. Chem. Soc.* **1975**, *97*, 3857–3858.
- [21] M. Abe, H. Furunaga, D. Ma, L. Gagliardi, G. J. Bodwell, *J. Org. Chem.* **2012**, *77*, 7612–7619.
- [22] Z. Wang, R. Akisaka, S. Yabumoto, T. Nakagawa, S. Hatano, M. Abe, *Chem. Sci.* **2021**, *12*, 613–625.
- [23] M. Yamashita, Y. Yamamoto, K. Akiba, D. Hashizume, F. Iwasaki, N. Takagi, S. Nagase, *J. Am. Chem. Soc.* **2005**, *127*, 4354–4371.
- [24] K. Akiba, M. Yamashita, Y. Yamamoto, S. Nagase, *J. Am. Chem. Soc.* **1999**, *121*, 10644–10645.

- [25] T. Yamaguchi, Y. Yamamoto, D. Kinoshita, K. Akiba, Y. Zhang, C. A. Reed, D. Hashizume, F. Iwasaki, *J. Am. Chem. Soc.* **2008**, *130*, 6894–6895.
- [26] D. G. Watson, L. Brammer, A. G. Orpen, O. Kennard, F. H. Allen, R. Taylor, *J. Chem. Soc. Perkin Trans. 2* **2004**, S1.
- [27] A. de Meijere, *Angew. Chem. Int. Ed. Engl.* **1979**, *18*, 809–826.
- [28] M. Tanaka, A. Sekiguchi, *Angew. Chem. Int. Ed.* **2005**, *44*, 5821–5823.
- [29] Q. Song, D. M. Ho, R. A. Pascal, *J. Am. Chem. Soc.* **2005**, *127*, 11246–11247.
- [30] W. D. Hounshell, D. A. Dougherty, J. P. Hummel, K. Mislow, *J. Am. Chem. Soc.* **1977**, *99*, 1916–1924.
- [31] J. M. McBride, *Tetrahedron* **1974**, *30*, 2009–2022.
- [32] B. Kahr, D. Van Engen, K. Mislow, *J. Am. Chem. Soc.* **1986**, *108*, 8305–8307.
- [33] S. Rösel, C. Balestrieri, P. R. Schreiner, *Chem. Sci.* **2016**, *8*, 405–410.
- [34] S. Rösel, J. Becker, W. D. Allen, P. R. Schreiner, *J. Am. Chem. Soc.* **2018**, *140*, 14421–14432.
- [35] R. Bianchi, G. Morosi, A. Mugnoli, M. Simonetta, *Acta Crystallogr. Sect. B Struct. Crystallogr. Cryst. Chem.* **1973**, *29*, 1196–1208.
- [36] M. Ehrenberg, *Acta Crystallogr.* **1966**, *20*, 182–186.
- [37] S. Kammermeier, R. Herges, P. G. Jones, *Angew. Chem. Int. Ed. Engl.* **1997**, *36*, 1757–1760.
- [38] K. Tanaka, N. Takamoto, Y. Tezuka, M. Kato, F. Toda, in *Tetrahedron*, **2001**, pp. 3761–3767.
- [39] E. Y. Tikhonchuk, R. M. K. Carlson, J. E. P. Dahl, S. Schlecht, M. Serafin, A. A. Fokin, P. A. Gunchenko, H. Hausmann, L. V. Chernish, P. R. Schreiner, *Nature* **2011**, *477*, 308–311.
- [40] A. A. Fokin, L. V. Chernish, P. A. Gunchenko, E. Y. Tikhonchuk, H. Hausmann, M. Serafin, J. E. P. Dahl, R. M. K. Carlson, P. R. Schreiner, *J. Am. Chem. Soc.* **2012**, *134*, 13641–13650.
- [41] D. Cho, Y. Iwabata, T. Yoshikawa, Y. L. Jin, H. Nakai, *Bull. Chem. Soc. Jpn.* **2015**, *88*, 1636–1641.
- [42] A. A. Zavitsas, *J. Phys. Chem. A* **2003**, *107*, 897–898.
- [43] J. L. Adcock, A. A. Gakh, J. L. Pollitte, C. Woods, *J. Am. Chem. Soc.* **1992**, *114*, 3980–3981.

Chapter 2

Creation and Demonstration of the Longest C–C Single Bond with a Bond Length beyond 1.8 Å

2-1. Introduction

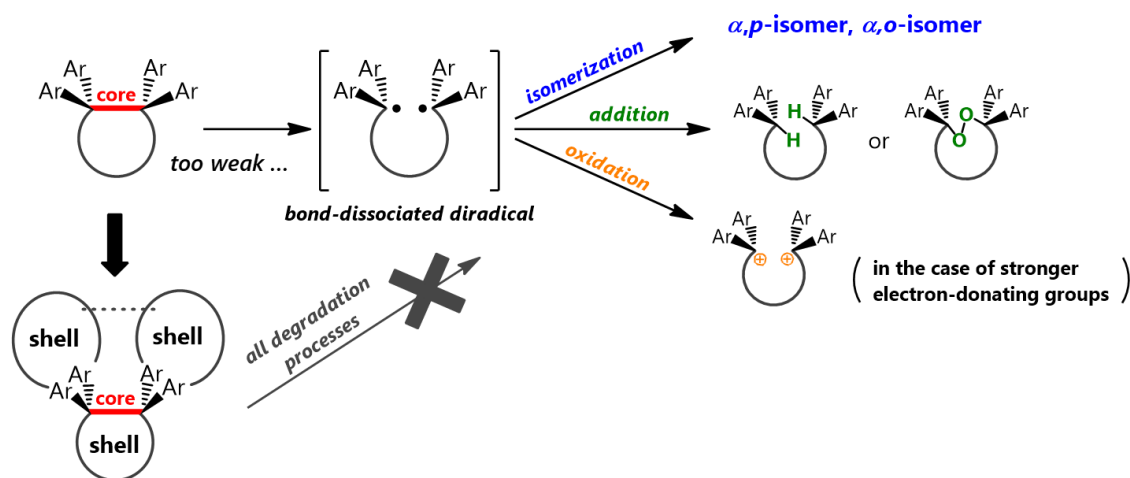
On the basis of the “expandability” of the extremely expanded C–C bonds found in other types of hexaphenylethane derivatives (HPEs) **ix** and **x**,^[1,2] the author envisaged that much longer C–C bonds could be realized by proper molecular design. The theoretical limit for the C–C bond length d_l was estimated by supposing a linear correlation between bond length and bond dissociation energy (BDE).^[3,4] However, it has been known for years that through-bond coupling can weaken the bond without changing the bond length.^[5,6] Furthermore, to describe the BDE of an expanded C–C bond, the Lennard-Jones-type potential may be more appropriate rather than a simple linear correlation. Thus, the change in BDE with an increase in the length of pre-strained weak C–C bonds (>1.7 Å) should be smaller than the energy required to lengthen a normal C–C bond (1.54 Å) to the same degree. The author’s group recently found that the expanded bond in some tetraarylpyracenes **xi** (X = OMe, Y = F; X = OMe, Y = H) exhibited quite different values in their pseudo-polymorphs because the bond length can be altered upon the application of a very slight energy change that is compensated by the crystal packing force rather than by the electronic factors of the substituents.^[7] The change in the C–C bond length of **DSAP** with a bond length beyond 1.7 Å in a single crystal induced by thermal stimulus was also observed.^[2] Therefore, it is highly likely that a C–C bond longer than the theoretically predicted value^[3,4] or the shortest non-bonded C ⋯ C contact [1.80(2) Å] in [1.1.1]propellane **xii**^[8] can be found when HPE derivatives with greater steric repulsion could be synthesized as stable entities. Herein, to obtain an extremely elongated C–C bond, the author newly proposes the intramolecular “core-shell strategy”: the weak Csp^3 – Csp^3 bond (core) is surrounded and protected by the shape-persistent and chemically inert Csp^2 fused rings (shell) which suppress the dissociation of the expanded bond by π – π interaction between shells. In this chapter, the author designed and synthesized dispiro(dibenzocycloheptatriene)-type HPEs **1a–1c**, where all degradation processes of the weak Csp^3 – Csp^3 bond are hampered to enable their isolation, and thus finally found the longest C–C bond among neutral hydrocarbons.

2-2. Results and Discussion

2-2-1. Design Concept

Based on the above mentioned background, the author sets three key points for the molecular design to create novel hydrocarbons with an unprecedented C–C bond length beyond 1.80 Å, so that the compounds could maintain their chemical stability despite the presence of a very weak C–C bond. To make the compounds stable, all degradation processes, such as isomerization, bond-dissociative addition, bond-dissociative ionization, and diradical formation have to be suppressed. Thus, the author newly proposed an intramolecular core-shell strategy as the first key concept because degradation reactions never occur when the degradation products have higher energy than the compound with an expanded bond. In the intramolecular core-shell strategy, HPE derivatives with a very weak bond (core) could be stabilized by a shape-persistent framework (shell) composed of rigid Csp^2 fused-rings (Scheme 1).

Scheme 1. Intramolecular core-shell strategy could suppress all degradation processes.



The intramolecular core-shell strategy applied on the HPE derivatives also favors bond expansion, because the rigid and bulky "shell" structure is directly connected with the "core". By increasing the steric repulsion between the shell units, the C–C bond of the core is more expanded. In addition, the author's group has shown that a "scissor effect" is a reliable structural modification for further expanding the "expandable" weak bond in fused HPE derivatives. The greater bond lengths were observed not only for the C1–C2 bond in **xi** or **xii** than in **x** but also for the C–O bond in **xvii** or **xviii** than in **xvi**^[9] in a single crystal, which can be rationalized by considering the angle strain caused by the ethano or etheno bridge at the opposite peri position (Figure 1). Thus, the author decided to apply the scissor effect as the second key concept to expand the central C–C bond by attaching the fused

ring at the terminal part of the shell.

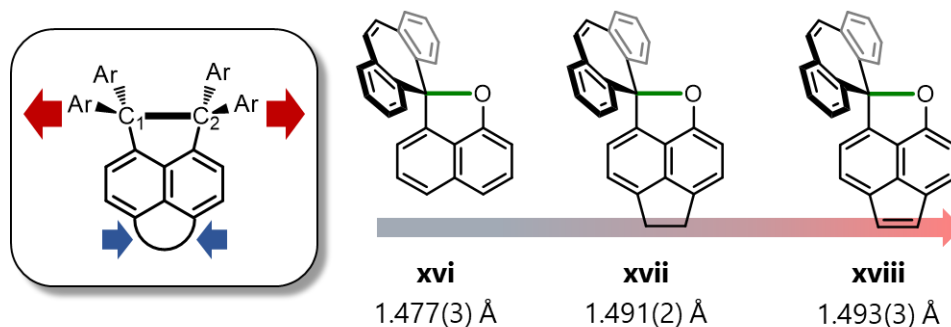


Figure 1. Scissor effect contributes the bond elongation.

Restriction of the HPE skeleton to a highly eclipsed conformation ($\alpha \approx 0$) to gain greater ‘‘eclipseness’’ is the third key concept to realize a greater d_I value, as demonstrated in **ix-xi**: a more eclipsed molecule in the crystal has a greater bond length than a less eclipsed geometry.^[1] Bridging of the two phenyl rings of the shell structure to form a spiro ring is an effective way for favoring the eclipsed conformation to restrict a rotation of phenyl rings that can lead to the skewed conformation with a less expanded bond by relaxing a steric repulsion. Since **DSAP** in crystal form adopts a nearly eclipsed geometry,^[2] the precisely determined d_I value has been considered the longest Csp^3-Csp^3 bond [1.791(3) Å at 413 K] among neutral organic compounds for a while. However, a single crystal of **DSAP** contains another crystallographically independent molecule with a skewed conformation and a smaller d_I value of 1.719(3) Å. Thus, the more elongated Csp^3-Csp^3 bond should be realized by introducing a larger ring into the shell structures because a large steric hindrance between a naphthalene ring and inner protons of the shells could force the molecule to adopt the more eclipsed conformation (Figure 2).

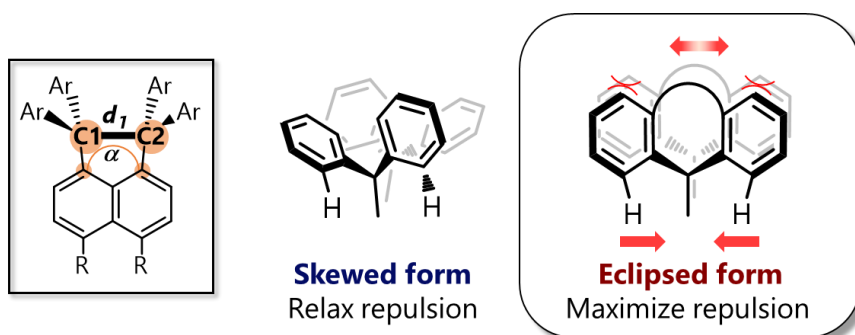


Figure 2. Eclipsed conformation maximizes the steric repulsion to elongate the C-C bond.

2-2-2. Theoretical Examination for Molecular Design

Before preparation, the author performed density functional theory (DFT) calculations at the M06-2X/6-31G* level of theory, which includes dispersion correction. The calculations of **DSAP** revealed that the skewed conformer is only the stable form and the eclipsed conformer is not found even as metastable state upon full optimization (Figure 3, Table 1), and thus spiro-cyclization alone is not enough to assure restriction to the eclipsed conformation.

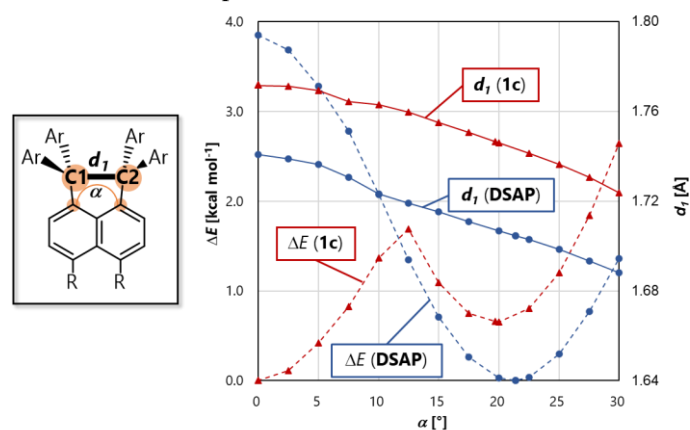


Figure 1. Energy potentials (dotted lines) and d_1 values (solid lines) for **1c** (red) and **DSAP** (blue) were calculated by varying the torsion angle α in steps of 2.5 ° and by considering metastable ($\Delta E = 0.66$ kcal mol⁻¹ for **1c**) or the most stable conformations.

Table 1. Torsion angles α and d_1 values of optimized structures for **1a-1c** and **DSAP** predicted by DFT calculations (M06-2X/6-31G*).

	1a	1b	1c		DSAP	
			(eclipsed)	(skewed)	(eclipsed)	(skewed)
α [°]	0	0	0	19.7	(0)	21.4
d_1 [Å]	1.730	1.767	1.771	1.746	(1.741)	1.705

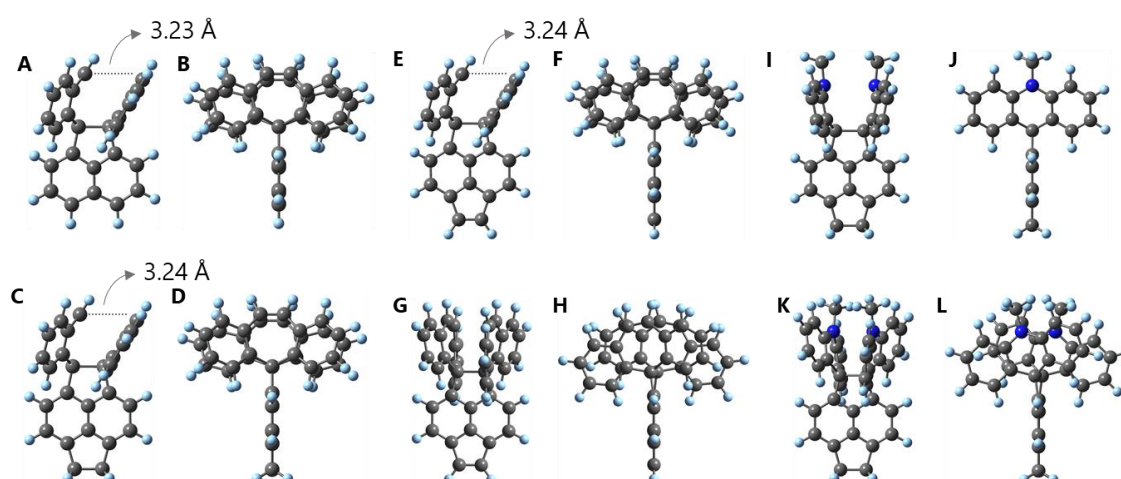


Figure 3. Optimized structures by DFT calculations (M06-2X/6-31G*) for **1a** [(A) front and (B) side views], **1b** [(C) front and (D) side views], **1c** [(E) front and (F) side views], metastable skewed conformer for **1c**; (K) front, (L) side views, eclipsed conformer in **DSAP**; (G) front, (H) side views, and skewed conformer in **DSAP**;

After a detailed theoretical examination of a series of compounds, the author found that spiro-fused dibenzocycloheptatriene (DBCHT) is a special shell framework that can favor the eclipsed form of HPEs (Figure 3, 4, Table 1). With all the above three concept, the author designed acenaphthene **1a**, pyracene **1b**, and dihydropyrycene **1c** as novel hydrocarbons. According to DFT calculations at the M06-2X/6-31G* level of theory, they all adopt a completely eclipsed conformation (Figures 4B, 4D, 4F) with large d_I values (Table 1) of 1.730, 1.767, and 1.771 Å, respectively. The largest value for **1c** and the larger value for **1b** than for **1a** is due to the scissor effect, because the shorter bridge at the opposite peri position induces greater angle strain on the naphthalene nucleus.

In contrast to the preference for the skewed conformer in **DSAP**, the eclipsed conformer is more stable for **1a-1c** (Figure 3, Table 1), which is due to the DBCHT unit based on the core-shell strategy. A series of calculations, in which the torsion angle of **1c** was fixed, predicted a preference for the eclipsed conformation as well as a greater d_I value for a more eclipsed conformation. These calculations showed that an unsymmetrical bent geometry for the two spiro rings of the shell structure, which is the outstanding structural feature of spiro-DBCHT **1a-1c**. One spiro ring adopts the well-known folded geometry (containing C1 atom). The concave face of the tub-shaped seven-membered ring faces another spiro unit, which is almost planar geometry (containing C2 atom). In this way, the two spiro units are overlapped in proximity to gain stabilization through π - π interaction (shortest C \cdots C contact between the vinylic carbons of DBCHT units: 3.23 Å for **1a**, 3.24 Å for **1b**, and 3.24 Å for **1c**, Figure 4A, 4C, 4E). Because of the folded and compact shape of the shell, any torsional displacement increases the steric repulsion between them and causes some loss of π - π stabilization. This is the reason why spiro-DBCHT **1a-1c** prefer a completely eclipsed geometry.

Such an overlapped geometry of the shells is also the key to maintaining chemical stability. Upon homolytic dissociation of the C1-C2 bond, DBCHT units have to adopt a planar geometry that cannot form a face-to-face stacking arrangement with π - π interaction between the vinylic carbons. The origin of the highly eclipsed conformation was supported by the noncovalent interaction (NCI) plots^[10] for the optimized structure of **1c** calculated at M06-2X/6-31G* level of theory, which visualizes the presence of both the attractive and repulsive interactions between neighboring units (Figure 5). The NCI plots exhibit a green surface corresponding to van der Waals (mainly $\pi\cdots\pi$) interactions between two DBCHT units, and a red surface involving a steric hindrance between a naphthalene ring and inner protons of the shells, which indicated that two DBCHT units are interacting to each other not only in attractive but also repulsive manners to stabilize and elongate the central C-C bond.

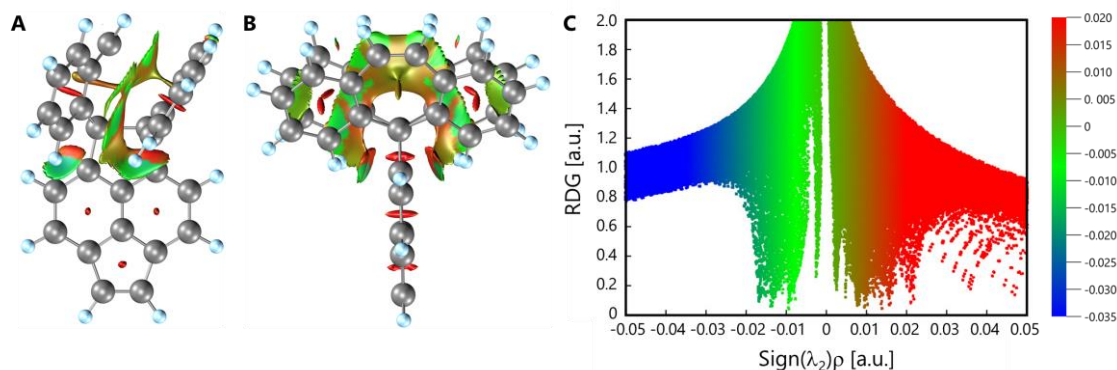


Figure 5. Top (A) and side (B) views of NCI plots (isovalue=0.5 a.u.) and reduced density gradient (RDG) scattering map (C) for **1c** optimized at M06-2X/6-31G* level of theory. Color online: blue represents strong attractive interactions, green indicates van der Waals interactions and red indicates repulsive/steric interactions.

Thus, upon conversion of single-bonded **1a-1c** to the corresponding diradicals, not only the BDE but also the stabilization energy through π - π interaction would be lost, making “diradical formation” less favorable. UM06-2X calculations suggest that the bond-dissociated triplet diradical corresponding to **1c** has a higher energy by 20.43 kcal mol⁻¹ without π - π interaction between the vinylic carbons (Figure 6A). Moreover, the diradical of the singlet state has no energy minimum for **1c**, because the DFT calculations started from a bond-dissociated species (C \cdots C distance >3.0 Å) as the initial structure converged to a single-bonded closed-shell species (Figure 6B).

Furthermore, for bridged triphenylmethyl radicals, the formation of peroxide or hydrogen abstraction is a representative degradation process (“bond-dissociative addition”).^[11,12] However, the shell structure of spiro-DBCHT **1a-1c** does not have enough space to accommodate two oxygen bridge or two C-H groups at the peri position between the two DBCHT units. According to DFT calculations, the spiro skeleton induces greater steric repulsion in the corresponding α,α -type isomer ($\Delta E = 22.16$ kcal mol⁻¹; Figure 6C) for **1c**, and thus the “isomerization” of **1c** would not occur because of the shape persistency of the shell. Unlike **DSAP**, which readily undergoes air oxidation to the corresponding bond-dissociated dication,^[13] the shell structure without any heteroatoms in **1a-1c** is chemically inert and exhibits only limited electron-donating ability, and thus “bond-dissociative oxidation” is less probable.

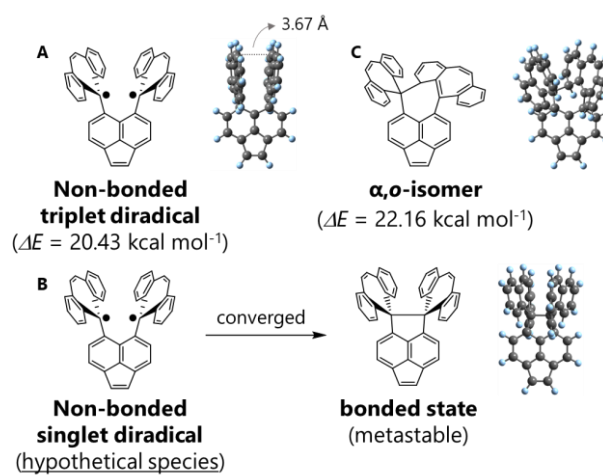
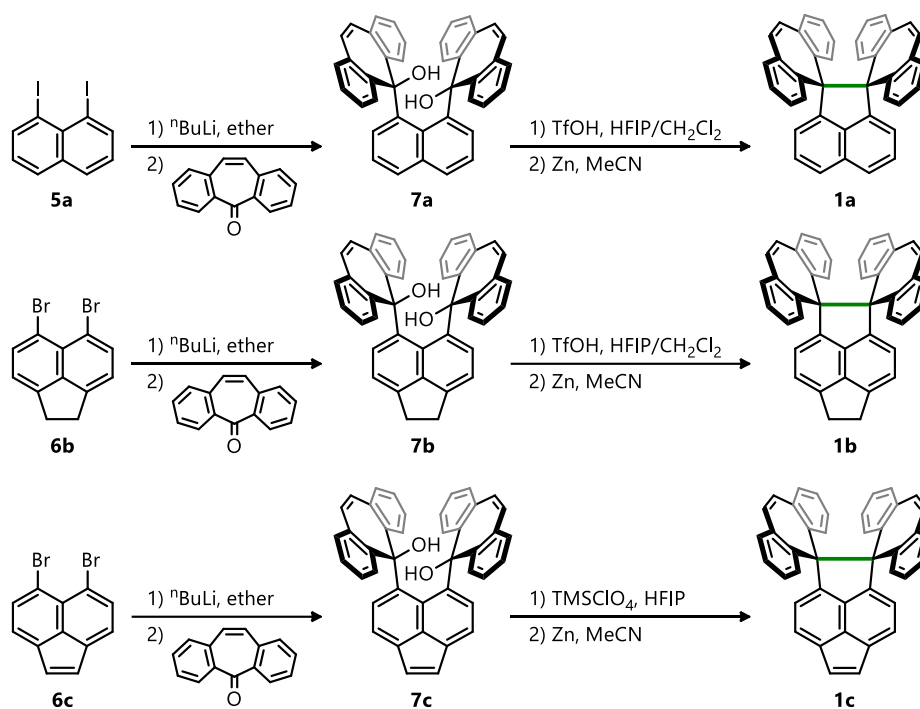


Figure 6. The optimized structures and relative energies of degradation products related to **1c** predicted by DFT calculations (UM06-2X/6-31G*).

2-2-3 Preparation of hydrocarbon **1a-1c**

Based on the above molecular design process assisted by DFT calculations, synthetic studies on spiro-DBCHT **1a-1c** have started. As shown in Scheme 1, diols **7a-7c** were obtained in 43%-73% yield by lithiation of the corresponding dihalo derivatives **5a-6c** followed by the addition of dibenzosuberone. Diols **7a-7c** were then exposed to acidic conditions^[14] in the presence of 1,1,1,3,3,3-hexafluoro-2-propanol (HFIP), and resulting precursor dications **3a²⁺-3c²⁺** were reduced with Zn powder to give desired hydrocarbons **1a-1c** in 50%-91% yield as colorless crystals for **1a** and **1b** and as an orange crystal for **1c** (Scheme 1). The formation of spiro-DBCHT **1a-1c** was confirmed by ¹H NMR and ¹³C NMR spectra, which show sharp signals assigned to singlet closed-shell species, and high-resolution mass spectra. They all are thermally stable compounds that can be kept under air at ambient temperature; thus, the validity of the intramolecular core-shell strategy the author designed was confirmed regarding the chemical stability.

Scheme 2. Preparation of spiro-DBCHT **1a-1c**.



2-2-4. Raman Spectroscopy

The author first investigated the stretching vibration of the expanded C1–C2 bond by Raman spectroscopy with single crystals of spiro-DBCHT **1a-1c** at 298 K, which gives direct information regarding the force constant of the bond. The experimentally obtained and simulated Raman spectra for these hydrocarbons are shown in Figure 7A, 7B, 7C. The calculated spectra by DFT method very nicely reproduce the experimental results, especially when the B3LYP calculated spectra are scaled with a factor^[15] of 0.9613 to consider anharmonicity (Figures 7D, 7E, 7F). The simulated absorption of symmetric C1–C2 stretching vibration in **1c** predicted to have the longest C–C bond among newly prepared hydrocarbons **1a-1c** appeared at 658 cm⁻¹ in Figure 7L (M06-2X/6-31G*), which corresponds to the normal mode with the greatest amplitude along the trajectory of the stretching vibration. The observed Raman shift for the central C–C bond in **1c** is 587 cm⁻¹, which represents a large shift compared with that (993 cm⁻¹) in ethane,^[16] because the extremely elongated C–C single bond has a much smaller force constant than the ordinary C–C bond (Figure 7C); the estimated force constants (108.3 N m⁻¹ for **1c** and 441.0 N m⁻¹ for ethane) were obtained as second derivatives of the energy to the bond length by DFT calculations (M06-2X/6-31G*) (Figure 8).^[17]

As in the case of **1c**, observed Raman shifts for **1a** and **1b** (650 cm⁻¹ and 582 cm⁻¹, respectively) are in good agreement with the frequencies for the stretching vibration of the C1–C2 bond determined by M06-2X/6-31G* calculations (724 cm⁻¹ for **1a** and 655 cm⁻¹ for **1b**) (Figures 7A-7D and 7E-7H). The Raman experiments demonstrated that all spiro-DBCHT **1a-1c** have a very weak C1–C2 bond, as predicted by DFT calculations.

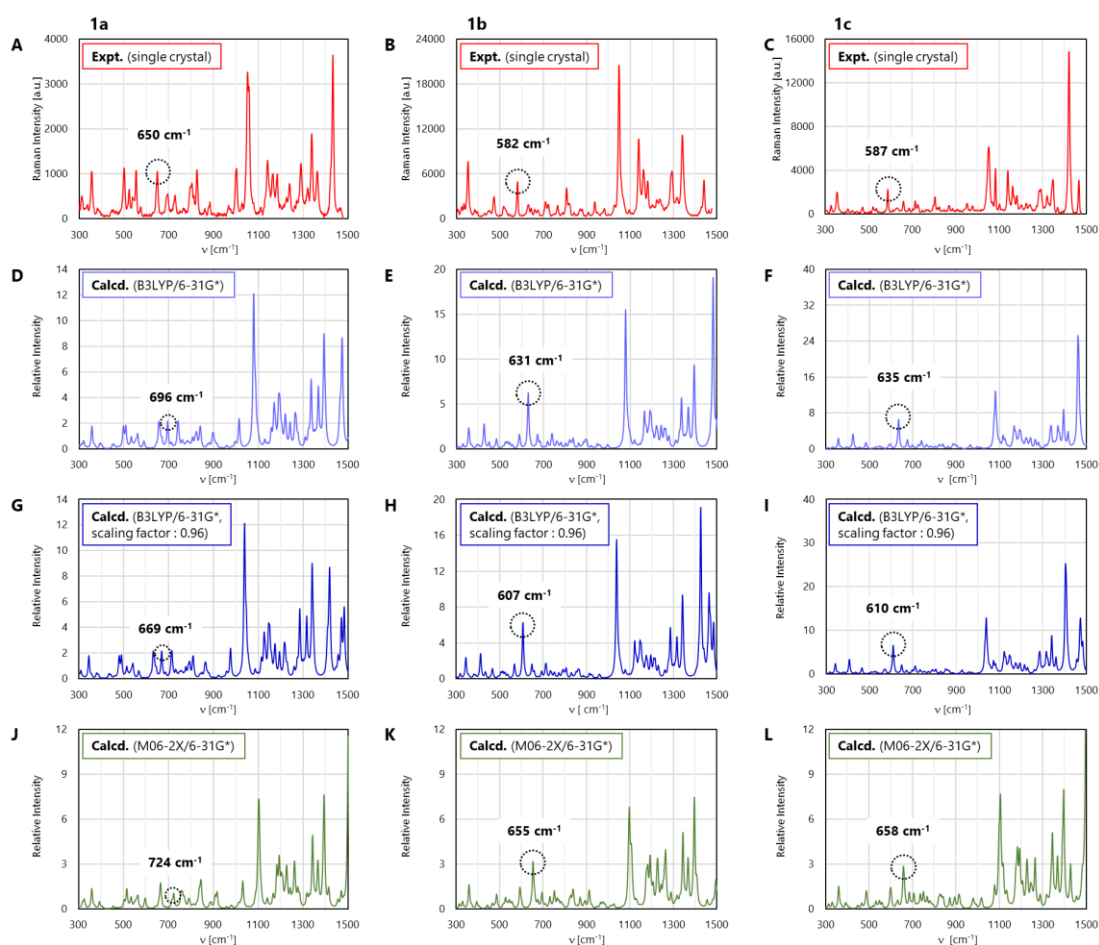


Figure 7. Raman spectra (red) measured by using a single crystal for (A) **1a**, (B) **1b** and (C) **1c** at 298 K. Simulated spectra predicted by DFT calculations at B3LYP/6-31G* level without scaling (light blue) for (D) **1a**, (E) **1b** and (F) **1c**, at B3LYP/6-31G* level under scaling (blue) for (G) **1a**, (H) **1b** and (I) **1c**, and at M06-2X/6-31G* level without scaling (green) for (J) **1a**, (K) **1b** and (L) **1c**.

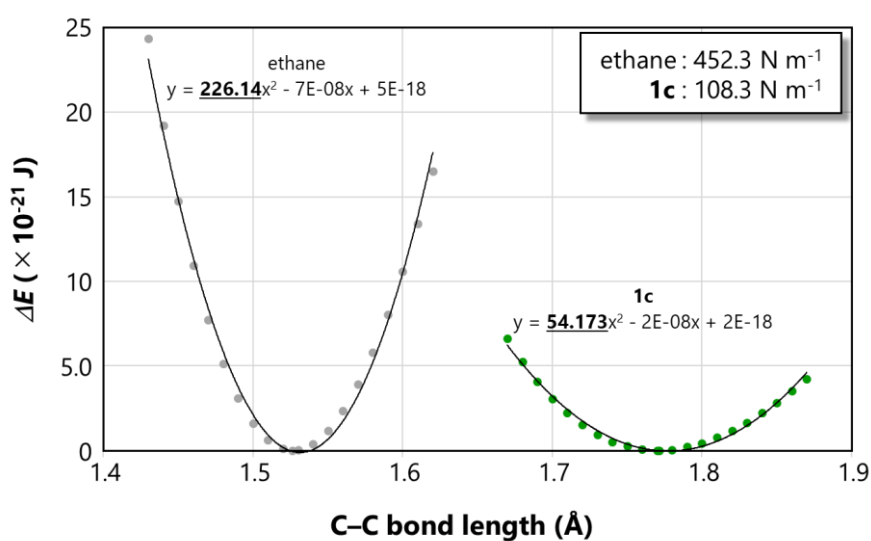


Figure 8. Energy potentials for ethane (black) and **1c** (green) calculated by varying the C1–C2 bond length d_1 in steps of 0.01 Å and by considering the most stable conformation (M06-2X/6-31G*).

2-2-5. Experimentally Determined Bond Length by X-Ray Analyses

Next, the author determined the d_I values in the crystal of these stable hydrocarbons by single-crystal X-ray diffraction. Firstly, X-ray analyses were performed at 200 K to elucidate the precise bond lengths. For **1a**, three crystallographically independent molecules are apparent, all of which adopt a quite similar eclipsed conformation with unsymmetrically bent geometries for the two DBCHT units (Figures 9A-9F). The X-ray structure looks very similar to the optimized structure obtained by the above-mentioned DFT calculations. The less symmetrical bent geometry was also observed in crystals of **1b** and **1c** [Figures 9G-9J ; shortest C...C contact between the vinylic carbons of DBCHT units: 3.25(1), 3.16(1), and 3.23(1) Å for **1a**, 3.19(1) Å for **1b**, and 3.21(1) Å for **1c**]. The d_I values at 200 K are 1.720(2), 1.723(2), and 1.742(2) Å for **1a**, 1.773(3) Å for **1b**, and 1.7980(18) Å for **1c** (Table 2). The value observed in **1c** is greater than that [1.791(3) Å at 413 K] in **DSAP**, which is the previously reported largest value.

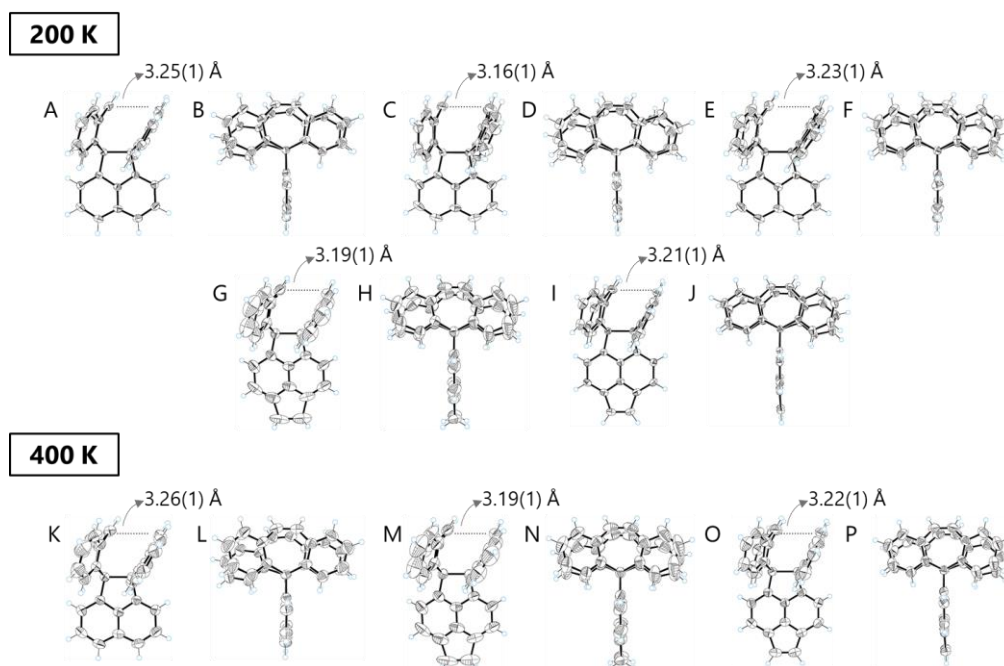
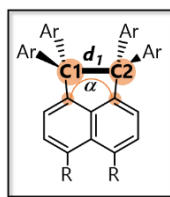


Figure 9. ORTEP drawings at 200 K for **1a** (A,C,E) front, (B,D,F) side views of three crystallographically independent molecules, **1b**; (G) front, (H) side views and **1c**; (I) front, (J) side views, and at 400 K for **1a** (K) front, (L) side views, **1b**; (M) front, (N) side views and **1c**; (O) front, (P) side views. At 400 K, three independent molecules of **1a** adopt similar structure, so the other two molecules are omitted for clarity. Thermal ellipsoids are shown at the 50% probability level.

Table 2. Torsion angles α and d_I values of X-ray structures for **1a–1c**.

Temp.		1a			1b	1c
200 K	α [°]	-3.50(13)	-3.44(14)	0.38(15)	0.24(18)	2.48(10)
	d_I [Å]	1.746(3)	1.720(2)	1.723(2)	1.773(3)	1.7980(18)
400 K	α [°]	-3.40(16)	-3.20(17)	0.35(17)	0.17(18)	2.68(12)
	d_I [Å]	1.746(3)	1.723(3)	1.726(3)	1.771(3)	1.806(2)



As shown in Figure 10 and Table 3, the values of bond angles around the C1 and C2 atoms clearly show that these carbon atoms are in the class of a standard sp^3 hybridization. By considering the π -orbital axis vector (POAV) angles ($\theta_{\sigma\pi}$), which are more often used as an indicator for a structural deformation analysis of a sp^2 carbon atom from planarity,^[18,19] these angles of both C1 and C2 atoms are similar to those of the standard Csp^3 carbon, as represented by ethane (109.5 °). These results indicate that the C1 and C2 atoms maintain the normal sp^3 hybridization despite their unsymmetrical geometries.

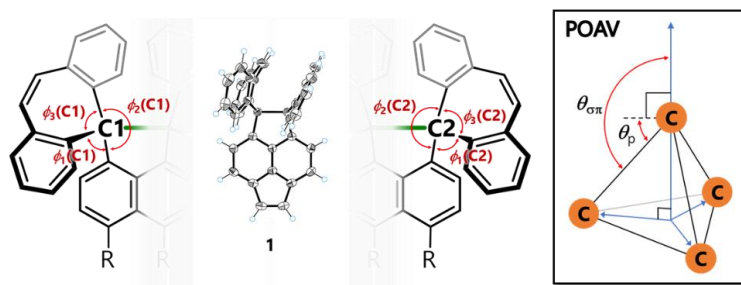


Figure 10. Definition of each angle.

Table 3. Bond angles ϕ [°] and average of POAV angles $\theta_{\sigma\pi}$ [°] of X-ray structures for **1a–1c**.

		C1				C2				
		ϕ_1	ϕ_2	ϕ_3	$\theta_{\sigma\pi}$	ϕ_1	ϕ_2	ϕ_3	$\theta_{\sigma\pi}$	
1a	200 K	mol. 1	110.52(13)	110.89(13)	110.00(12)	108.45	106.04(11)	104.53(13)	122.22(13)	107.76
		mol. 2	108.35(12)	109.19(13)	112.71(13)	108.84	105.94(14)	105.80(13)	119.99(13)	108.20
		mol. 3	110.55(14)	110.07(14)	110.58(12)	108.53	104.42(12)	105.65(13)	121.25(14)	108.29
	400 K	mol. 1	110.62(15)	111.04(14)	109.71(14)	108.47	105.97(13)	104.85(15)	122.11(15)	107.72
		mol. 2	108.56(14)	108.83(16)	112.87(15)	108.84	106.49(16)	105.84(16)	119.62(15)	108.14
		mol. 3	110.48(17)	109.91(17)	110.62(15)	108.59	104.38(15)	105.79(16)	121.44(16)	108.19
1b	200 K	110.97(17)	111.69(16)	110.30(15)	107.91	105.17(16)	105.41(15)	122.13(15)	107.80	
	400 K	111.0(2)	111.5(2)	110.28(17)	107.97	105.11(17)	105.31(16)	122.19(18)	107.83	
1c	200 K	110.95(10)	110.32(9)	111.53(10)	107.97	106.50(9)	105.85(10)	122.1(1)	107.20	
	400 K	111.03(12)	110.28(12)	111.81(12)	107.85	106.60(12)	106.07(12)	121.92(13)	107.16	

The Fo-Fc map,^[20,21] which visualizes the distribution of electron density based on the X-ray diffraction data, obviously indicates the presence of bonding electrons between C1 and C2 atoms in **1c** (Figure 11A). Although the trends of the bond lengths and their structures by X-ray analyses are in good agreement with those by DFT calculations, the d_I values in the X-ray structures of **1a–1c** are greater than those in the optimized structures. The observed expansion would be accounted for by the shallow energy potential (Figure 8) of the elongated and weak bond with a small BDE.

To investigate the stability of these hydrocarbons in crystal form at elevated temperature, the author carried out variable-temperature (VT) X-ray analyses (from 200 to 400 K every 40 K) by using the same single crystals of **1a–1c** (at 400 K: Figures 9K–9P). No degradation was suggested in any of the measurements. Even when the X-ray analyses of **1a–1c** were conducted at 400 K, the estimated standard deviations of the C1–C2 bond length were less than 0.003 Å, indicating that the measurement

was highly accurate even at high temperature (Table 3).

Moreover, the Fo-Fc map indicates the presence of bonding electrons between C1 and C2 in **1c** even at 400 K (Figure 11B) because of the high accuracy of the X-ray measurements. The thermal ellipsoids of the carbon atoms are still small at 400 K, particularly in **1c** (Figures 9O, 9P), yet the C1–C2 bonds marginally expand upon heating. Thus, the greatest d_I value of 1.806(2) Å in **1c** was determined at 400 K, which is impressive for an accurately determined C–C bond length. Therefore, the assumed limit for the C–C bond length (1.803 Å)^[4] by supposing a linear correlation between the bond length and BDE was proven to be invalid in other types of hydrocarbons including the present examples.

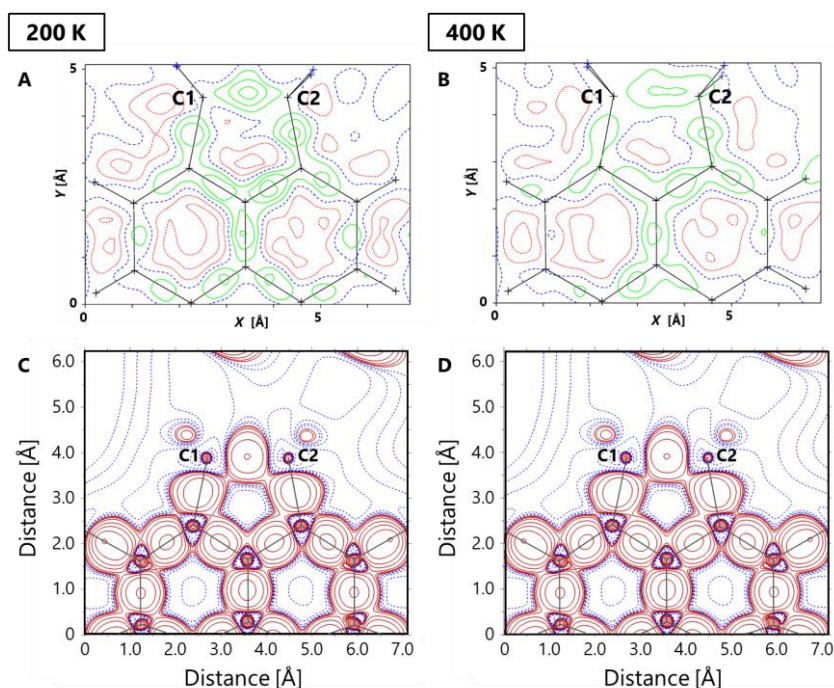
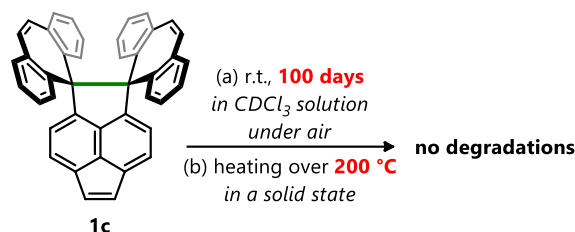


Figure 11. Experimentally obtained Fo-Fc maps around the ultralong C1–C2 bond in **1c** at (A) 200 K and (B) 400 K. The contour interval is $0.05 \text{ e}\text{\AA}^{-3}$: solid lines are positive values (green), and dotted lines are zero (blue) and negative values (red). Theoretically electron deformation maps (B3LYP-D3/6-311+G**) at (C) 200 K and (D) 400K: red solid lines represent positive value from 0.01 to $0.05 \text{ e}\text{\AA}^{-3}$ in steps of $0.01 \text{ e}\text{\AA}^{-3}$ and from 0.10 to $0.50 \text{ e}\text{\AA}^{-3}$ in steps of $0.05 \text{ e}\text{\AA}^{-3}$. The blue dashed lines represent negative contours from -0.05 to -0.50 in steps of $-0.05 \text{ e}\text{\AA}^{-3}$.

2-2-6. Stability of the Hydrocarbon **1c** with a Very Weak C–C Bond

To gain insight into the stability of weak bonds of d_I greater than 1.80 Å, the author conducted ^1H NMR spectroscopy on **1a–1c** in solution. The ^1H NMR spectrum of **1c** in CDCl_3 at 296 K (Figure 12B) is similar to those of **1a** and **1b**. The spectrum did not change when the solution was left to stand at ambient temperature for 100 days under air (Scheme 3 and Figure 12A). Furthermore, no signs of line broadening and decomposition were observed for signals in the ^1H NMR spectrum of **1c** in $\text{C}_6\text{D}_5\text{Br}$ even at 400 K (Figure 12C), which are assigned to a single species in the singlet state. The spectrum consists of peaks that can be assigned to a single species with C_{2v} symmetry despite the unsymmetrically bent structure in the solid state because a thermal equilibrium with the skewed conformation predicted by the DFT calculations (Figure 3, Table 1) is faster than the NMR timescale. No broadening or peak separation occurred even at 190 K in CD_2Cl_2 (Figure 12D), indicating a rapid degenerated conformational change in solution on the NMR timescale.

Scheme 3. Investigation of the stability of **1c**.



The same conclusion was reached when the author investigated the ^{13}C NMR spectra of **1a–1c** in CDCl_3 . The spectra showed the signals assigned to the carbon atoms involved in the ultralong bond, which appeared in the quaternary C_{sp^3} region (81.82 ppm for **1a**, 86.30 ppm for **1b**, and 87.46 ppm for **1c**). A slight downfield shift was observed with an increase in the C–C bond length, which keeps the carbon nuclei away from bonding electrons. If the central bond was cleaved, the author would have seen an obvious upfield shift, which was caused by a shielding effect as a result of bond-dissociated radicals.

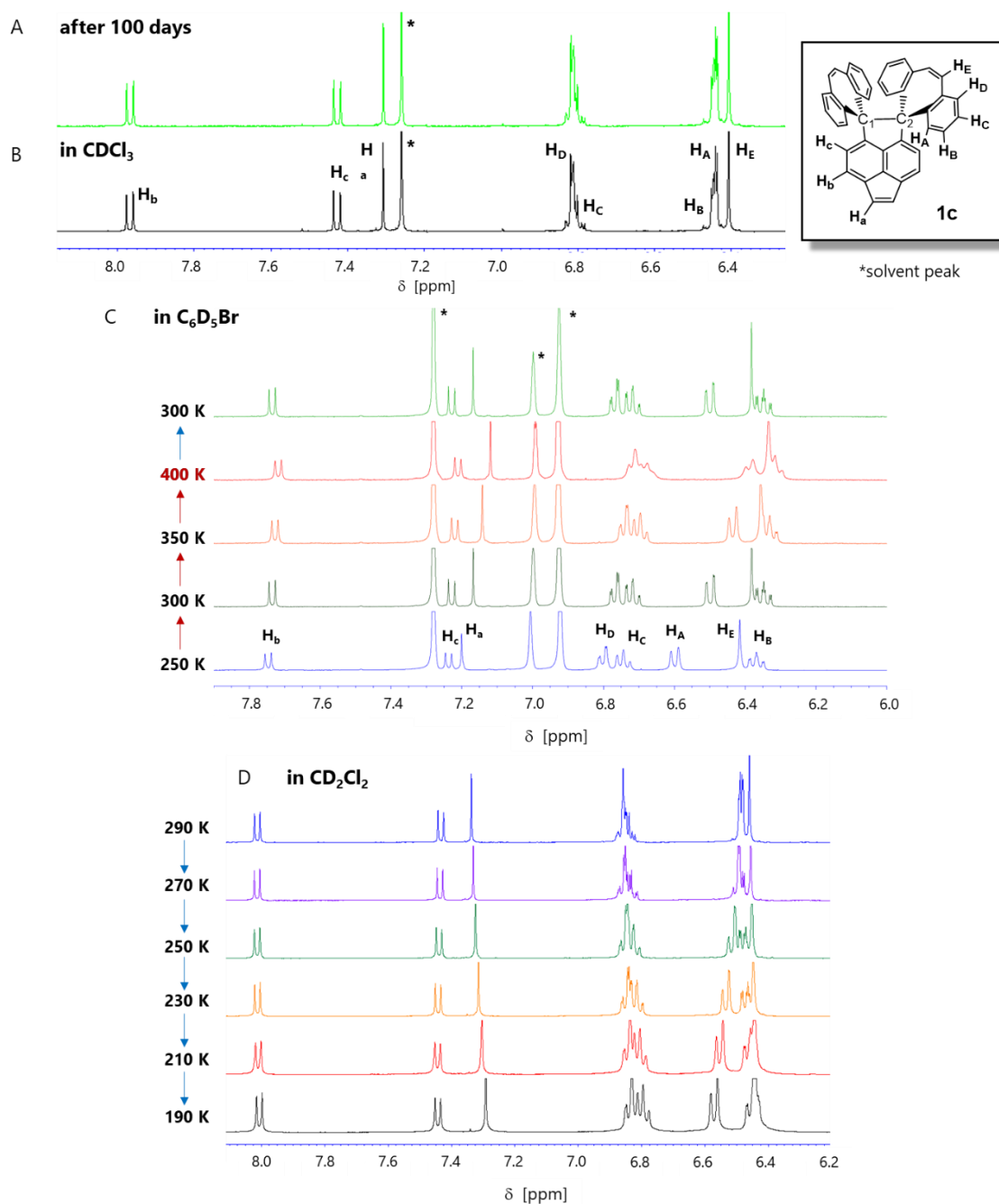
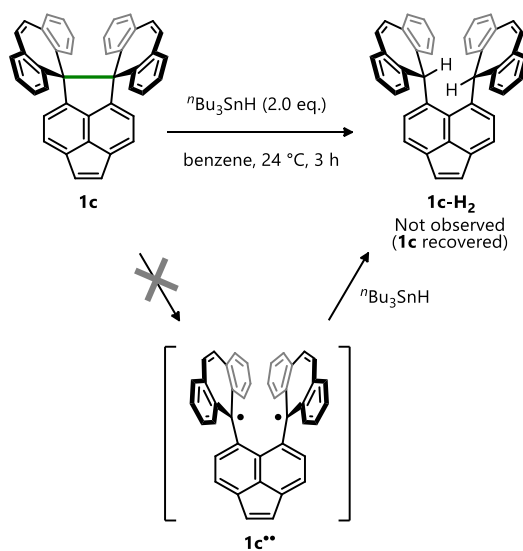


Figure 12. ^1H NMR Spectra of **1c** in CDCl_3 at 296 K (A) after the solution was allowed to stand at ambient temperature for 100 days under air, and (B) before standing. A VT ^1H -NMR spectra of **1c** (C) in $\text{C}_6\text{D}_5\text{Br}$ at higher temperatures and (D) in CD_2Cl_2 at lower temperatures.

Absence of diradical contribution was also confirmed by the reaction of **1c** with ${}^n\text{Bu}_3\text{SnH}$. If there is a diradical character of the long C–C bond in **1c**, the hydrocarbon would react with ${}^n\text{Bu}_3\text{SnH}$ to produce hydrogen adducts.^[22] Actually, the starting material was completely recovered, meaning that spiro-DBCHT **1c** does not have a diradical character in solution (Scheme 4). These experimental results of ${}^1\text{H}$ and ${}^{13}\text{C}$ NMR spectroscopies and the reaction with ${}^n\text{Bu}_3\text{SnH}$ demonstrated that hydrocarbon **1c** with the ultralong C1–C2 bond is extremely stable both kinetically and thermodynamically, even in solution.

Scheme 4. Attempts to trap the bond dissociated species.



2-2-7. Theoretical analysis for the nature of ultralong C–C single bond

The nature of the ultralong C–C single bond beyond 1.80 Å is of interest because this is the first example of demonstrating the presence of such an elongated bond. The electronic interaction between C1 and C2 atoms was investigated by atoms in molecules (AIM),^[23] electron localization function (ELF),^[24] and natural bond orbital (NBO) analyses. The results of AIM analysis for **1a-1c** revealed that there is a path of maximum electron density (bond path) between C1 and C2 atoms, partitioned in parts of equal lengths by bond critical points (BCPs; Figure 13). The topological parameters of the BCPs between C1 and C2 atoms for **1a-1c** indicate slightly reduced electron density ρ , negative total energy H , and negative Laplacian $\nabla^2\rho$, corresponding to shared-shell interaction (Table 4).^[25] Maps of the Laplacian of the electron density related to valence electron for **1c**, which were calculated at B3LYP-D3/6-311+G** level of theory by using the crystal structure as the initial structure, obviously indicate the presence of the bonding electrons between C1 and C2 atoms (Figure 14B, 14F). As shown in Figure 15A, 15B, the presence of the C1–C2 bond is also described by ELF analysis, which shows the localization of electrons: in the regions where Pauli repulsion is strong (atomic shells, chemical bonds, lone electron pairs *etc.*), the ELF value is close to 1, whereas in the regions where the probability of the same-spin electrons being close is high, the ELF value is close to 0. The maximum value of ELF along the C1–C2 axis is 0.93, indicating the localization of electrons on the ultralong C–C bond (Figure 15C, 15D).

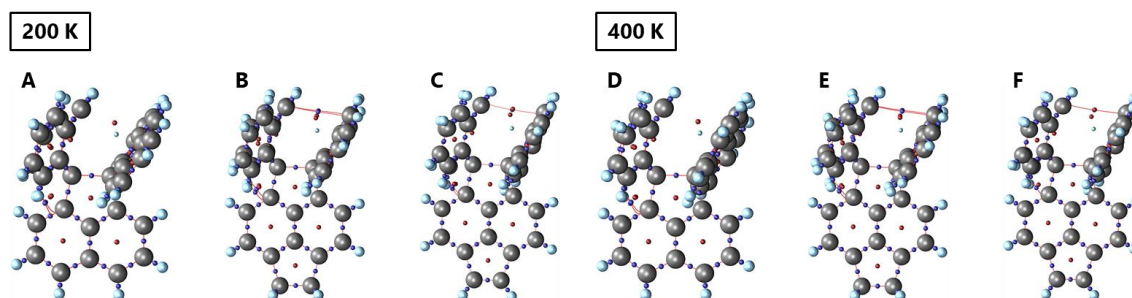


Figure 13. Molecular graphs of (A,D) **1a**, (B,E) **1b** and (C,F) **1c** based on the atom in molecules (AIM) analyses calculated by B3LYP-D3/6-311+G** level of theory at each temperatures. Color dots are corresponding to bond critical points (BCPs; blue), ring critical points (RCPs; red) and cage critical points (CCPs; light blue). Crystal structures were elected as an initial structure. Three independent molecules of **1a** adopt similar structure, so the molecule with the longest C–C bond was selected as a representative structure.

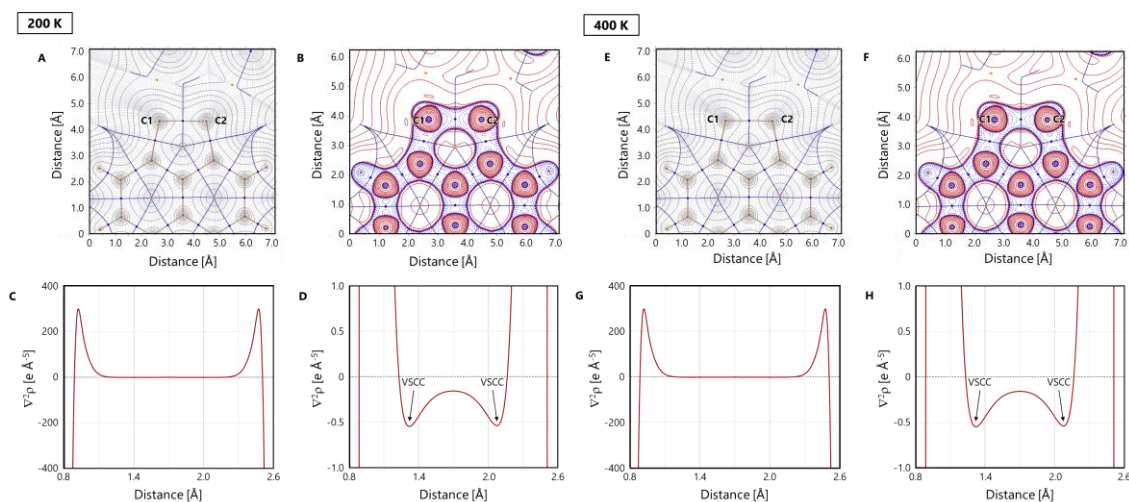


Figure 14. (A,E) Electron density map, and (B,F) 2D- and (C,D,G,H) 1D-Laplacian profiles of electron density $\nabla^2\rho$ around the C1–C2 bond of **1c**. Red solid lines are positive values and blue dotted lines represent negative values.

Table 4. Topological parameters of the BCPs highlighted in Figure 9. Crystal structure of **1a-1c** and optimized ethane were used for calculations (B3LYP-D3/6-311+G**).

	200 K			400 K			ethane
	NAP	ANE	ANY	NAP	ANE	ANY	
Bond length [Å]	1.742(2)	1.773(3)	1.7980(18)	1.746(3)	1.771(3)	1.806(2)	1.531
Density of all electrons : ρ_b	0.1629	0.1538	0.1469	0.1616	0.1544	0.1444	0.2373
Energy density : $H(r)$	-0.08810	-0.07893	-0.07234	-0.08682	-0.07958	-0.07013	-0.1864
Laplacian of electron density : $\nabla^2\rho$	-0.2105	-0.1825	-0.1625	-0.2066	-0.1845	-0.1555	-0.5288
Electron localization function (ELF)	0.9392	0.9354	0.9319	0.9387	0.9357	0.9303	0.9587
Localized orbital locator (LOL)	0.7972	0.7920	0.7872	0.7966	0.7923	0.7851	0.8282
Ellipticity of electron density ε	0.01822	0.01302	0.01073	0.01751	0.01301	0.01054	0.0000

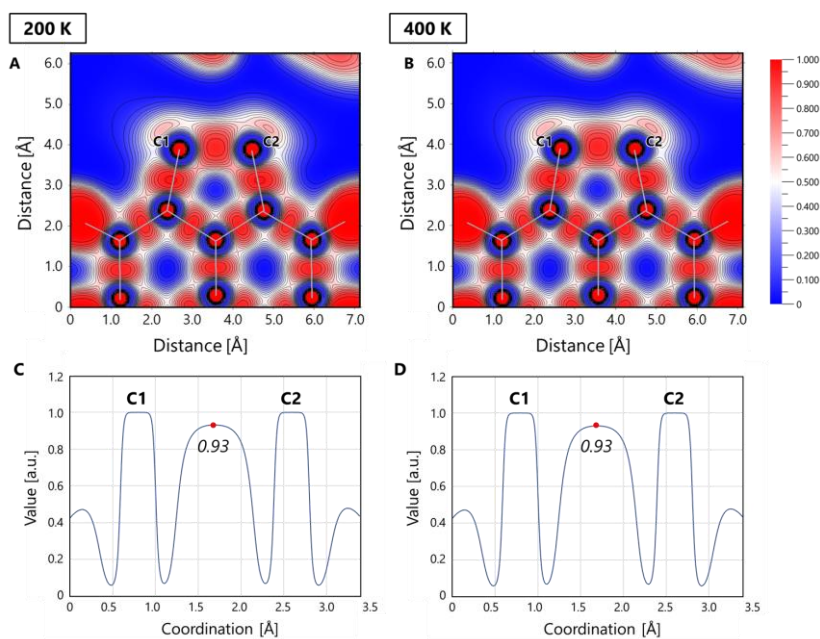


Figure 15. Electron localization function (ELF) maps of **1c** at (A) 200 K and (B) 400 K. 1D-ELF profiles along the C1–C2 bond path of **1c** at (C) 200 K and (D) 400 K.

In addition, the C1–C2 bonding orbital was visualized by NBO analysis based on the DFT calculations for **1a-1c** at the B3LYP-D3/6-311+G** level of theory. The bonding orbital of the C1–C2 bond for **1a-1c** is distributed on the C1–C2 axis, which is consistent with that the C1–C2 bond path obtained by AIM linearly connects each atom and certainly exhibits the σ -bonding property. As shown in Table 5, each of predicted Wiberg bond index (WBI) of 0.87 for **1a**, 0.86 for **1b**, and 0.85 for **1c**, respectively, is smaller than that for ethane (WBI: 1.04). On the other hand, the NBO analysis revealed that the occupancy of the C1–C2 bonding orbital for **1a-1c** is in the range of 1.92-1.93 e, which is only a small depletion (~4%) compared to the ideal value (2.00 e for ethane). The s -character of the C1 and C2 atoms for C1–C2 single bond is 20% for **1a**, 19-20% for **1b**, and 19% for **1c**, respectively. In addition, CASSCF(2,2)/6-311+G** calculation of **1c** based on single crystal structures at both 200 K and 400 K gave a small natural orbital occupancy number (NOON)^[26] of 0.076 and 0.076, respectively (diradical index $y_0 = 7.6\%$ and 7.6% , respectively) for the lowest unoccupied natural orbital (LUNO). It can be rationalized by an increased contribution of the p -orbitals away from the nucleus due to the formation of longer bonds. Thus, the extremely elongated C–C bond of **1a-1c** is weak, but it still maintains the covalently bonding properties with two electrons.

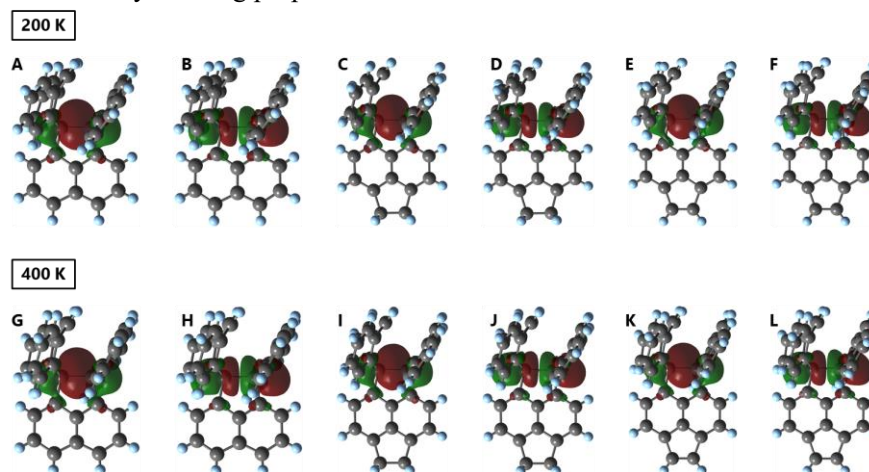


Figure 16. Calculated NBOs between C1 and C2 atoms of **1a** (A,B,G,H), **1b** (C,D,I,J) and **1c** (E,F,K,L) at the B3LYP-D3/6-311+G** level of theory. Crystal structures were elected as an initial structure. Three independent molecules of **1a** adopt similar structure, so the molecule with the longest C–C bond was selected as a representative structure.

Table 5. NBO analysis parameters of the bonding orbital between C1 and C2 atoms for **1a-1c** at the B3LYP-D3/6-311+G**.

	200 K			400 K			
	NAP	ANE	ANY	NAP	ANE	ANY	
Bond length [Å]	1.742(2)	1.773(3)	1.7980(18)	1.746(3)	1.771(3)	1.806(2)	
Occupancy	1.919	1.912	1.910	1.919	1.912	1.908	
WBI	0.8604	0.8416	0.8345	0.8594	0.8427	0.8302	
s -character [%]	C1	20.40	19.47	19.16	20.36	19.55	18.83
	C2	20.05	19.15	18.64	19.92	19.22	18.43
NBO-energy [eV]	<i>bonding</i>	-11.65	-11.16	-11.12	-11.59	-11.65	-11.01
	<i>anti-bondng</i>	5.551	5.491	4.922	5.852	5.551	4.816

2-3. Conclusion

On the basis of the proposed intramolecular core-shell strategy to make a weak and elongated bond stable enough, the author has designed a series of dispiro(dibenzocycloheptatriene)-type HPE derivatives, **1a-1c**. The weak bond in the hydrocarbons the author prepared is expanded by the forced adoption of an eclipsed conformation, which can maximize the steric repulsion around the central C–C bond. For dihydropyracylene derivative **1c**, further expansion was achieved through a scissor effect. The very small Raman shift corresponding to the C–C stretching vibration as well as the greatest d_I value accurately determined by X-ray analysis revealed that **1c** has a very weak C–C bond. The extensive theoretical studies identified that an extremely elongated C–C bond of **1a-1c** has a small bond index but keeps pure σ -bonded character with two electrons. Nonetheless, **1c** and other dispiro(dibenzocycloheptatriene)s are kinetically and thermodynamically stable entities with no signs of diradical contribution even in solution.

Because the observed value is greater than the shortest non-bonded contact in the [1.1.1]propellane derivative,^[8] the covalently bonded state and non-bonded state would be seamlessly connected in terms of the interatomic distance. According to the present results, it is highly likely that the author could find an even longer C-C bond (“hyper covalent bond” with a bond length greater than the distance of the shortest non-bonded C···C contact) under the proper molecular design following the intramolecular core-shell strategy.

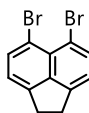
2-4. Experimental Section

General Procedures

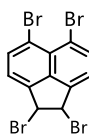
All reactions were carried out under an argon atmosphere. All commercially available compounds were used without further purification unless otherwise indicated. Dry MeCN was obtained by distillation from CaH₂ prior to use. Column chromatography was performed on silica gel I-6-40 (YMC) of particle size 40-63 μm or a silica gel 60N (Kanto, spherical neutral, 40-50 μm). ¹H and ¹³C NMR spectra were recorded on a BRUKER Ascend™ 400 (¹H/400 MHz and ¹³C/100 MHz) spectrometer. IR spectra were measured as a KBr pellet on a JEOL JIR-WINSPEC100 FT/IR spectrophotometer. Mass spectra were recorded on a JEOL JMS-T100GCV spectrometer in FD mode (GC-MS&NMR Laboratory, Research Faculty of Agriculture, Hokkaido University). Melting points were measured on a Yamato MP-21 melting point apparatus and are uncorrected. The analysis of Raman spectroscopy was carried out with in Via Reflex at the OPEN FACILITY, Hokkaido University Sousei Hall. DFT calculations were performed with the Gaussian 09W^[27] and 16W^[28] program package. The geometries of the compounds were optimized by using the M06-2X method in combination with the 6-31G* basis set unless otherwise indicated. Diradical character (y_0) was predicted by CASSCF (2,2) with 6-311+G** basis set performed by ORCA 4.2.1.^[29,30] Version 3.8 of the Multiwfn software^[31] was used for topological analysis of the electron density that is obtained by DFT calculations. The NBO analyses were performed with the Version 7.0 of the NBO^[32] which was implemented in the Gaussian 16W program. The atomic coordinates were obtained from crystal structures of **1a-1c** at each temperature and the wave function was calculated at B3LYP-D3/6-311+G** for Laplacian maps, AIM, NBO and ELF analyses.

Preparation

- Preparation of hydrocarbons **1a-1c**

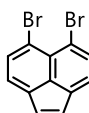
5,6-Dibromoacenaphthene **6b**.**6b**

To a suspension of acenaphthene (5.00 g, 32.4 mmol) in DMF (20 mL) was added a suspension of N-bromosuccinimide (NBS, 12.7 g, 71.5 mmol) in DMF (20 mL) at 0 °C. The mixture was stirred at 23 °C for 21 h in the dark, cooled to 0 °C, and filtered to obtain the crude product. To the crude solid was added EtOH (30 mL), and the suspension was refluxed for 21 h. After cooling to 22 °C, the resulting precipitates were filtered and washed with EtOH to give **13b** (1.58 g, 16%) as a pink solid. ¹H NMR data were identical to those in literature. [33]

1,2,5,6-Tetrabromoacenaphthene **6b-Br₂**.**13b-Br₂**

A mixture of **13b** (1.00 g, 3.21 mmol), NBS (1.26 g, 7.05 mmol) and benzoyl peroxide (201 mg, 858 μmol) in CHCl₃ (40 mL) was refluxed for 5 h. After cooling to 25 °C, the resulting solution was diluted with water and extracted with CHCl₃. The organic layer was washed with water, saturated NaHCO₃ aq. and brine, and dried over MgSO₄. After filtration, the solvent was concentrated under reduced pressure. The residue was purified by column chromatography on silica gel (hexane only) to give **13b-Br₂** (872 mg, 58%) as a yellow solid.

¹H NMR data were identical to those in literature. [34]

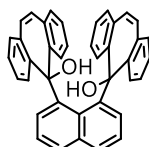
1,8-Dibromoacenaphthylene **6c**.**6c**

A mixture of **13b-Br₂** (2.00 g, 4.26 mmol) and nonactivated Zn powder (835 mg, 12.8 mmol) in AcOH (200 mL) was refluxed for 1 h. After cooling to 24 °C, the resulting suspension was diluted with water and extracted with CHCl₃. The organic layer was washed with water, saturated NaHCO₃ aq. and brine,

and dried over MgSO_4 . After filtration, the solvent was concentrated under reduced pressure. The residue was purified by column chromatography on silica gel (hexane only) to give **13c** (1.24 g, 94%) as a yellow solid.

^1H NMR data were identical to those in literature. ^[34]

1,8-Bis(5-hydroxydibenzo[*a,d*]cycloheptatrien-5-yl)naphthalene 7a.



7a

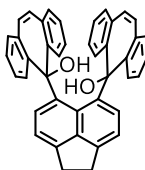
To a suspension of 1,8-diiodonaphthalene **13a** (999 mg, 2.63 mmol) in dry ether (100 mL) was added $n\text{-BuLi}$ in hexane (1.55 M, 4.07 mL, 6.31 mmol) at 24 °C. After stirring for 1 h at 24 °C, dibenzosuberone (1.30 g, 6.31 mmol) was added and the mixture was refluxed for 4 h. Then, the mixture was cooled to 24 °C, and diluted with water. The resulting mixture was extracted with CHCl_3 . The organic layer was washed with water and brine, and dried over MgSO_4 . After filtration, the solvent was concentrated under reduced pressure. The residue was purified by reprecipitation (CHCl_3 /hexane) and column chromatography on silica gel (CHCl_3 /hexane = 1.5) to give **14a** (844 mg, 59%) as a colorless solid.

mp: 282-288 °C (decomp.); ^1H NMR (CDCl_3): δ 8.04 (dd, $J = 1.2, 8.0$ Hz, 2H), 7.93 (dd, $J = 1.3, 8.1$ Hz, 2H), 7.72 (ddd, $J = 1.3, 8.0, 8.6$ Hz, 2H), 7.41 (ddd, $J = 1.2, 7.6, 8.6$ Hz, 2H), 7.36 (dd, $J = 1.1, 7.5$ Hz, 2H), 7.23 (ddd, $J = 1.4, 8.1, 8.6$ Hz, 2H), 7.06 (dd, $J = 1.3, 7.6$ Hz, 2H), 6.98 (ddd, $J = 1.3, 7.5, 8.6$ Hz, 2H), 6.90 (t, $J = 7.5$ Hz, 2H), 6.74 (dd, $J = 1.4, 7.5$ Hz, 2H), 6.70 (dd, $J = 1.1, 7.5$ Hz, 2H), 5.63 (d, $J = 11.4$ Hz, 2H), 5.56 (d, $J = 11.4$ Hz, 2H), 1.25 (s, 2H); ^{13}C NMR (CDCl_3): δ 149.11, 139.33, 138.93, 134.64, 133.03, 132.66, 132.00, 131.87, 129.94, 129.59, 128.18, 128.11, 127.71, 127.68, 127.42, 126.79, 125.90, 125.34, 122.81, 121.73, 79.39; IR (KBr): 3551, 3061, 3048, 1920, 1621, 1595, 1482, 1433, 1312, 1219, 1152, 1119, 1050, 1038, 1002, 813, 801, 789, 769, 755, 743, 648 cm^{-1} ; LR-MS (FD) m/z (%): 542.19 (10), 541.19 (46), 540.19 (M^+ , bp); HR-MS (FD): [M^+] calcd. for $\text{C}_{40}\text{H}_{28}\text{O}_2$, 540.20893; found, 540.20837.

Dispiro[(dibenzo[*a,d*]cycloheptatriene)-5,1'-acenaphthene-2',5''-(dibenzo[*a,d*]cycloheptatriene)] **1a**.**1a**

To a suspension of **1a** (99.9 mg, 185 μ mol) in dry CH_2Cl_2 (3 mL) and 1,1,1,3,3,3-hexafluoro-2-propanol (HFIP, 3 mL) was added trifluoromethanesulfonic acid (TfOH, 160 μ L, 1.81 mmol) at 25 $^\circ\text{C}$. The mixture was stirred for 1 h, and the solvent was evaporated. To the residue were added dry MeCN (10 mL) and activated Zn powder (1.81 g, 27.7 mmol) at 25 $^\circ\text{C}$. After stirring for 1 h at 25 $^\circ\text{C}$, the mixture was diluted with water, and extracted with CHCl_3 . The organic layer was washed with water and brine, and dried over MgSO_4 . After filtration, the solvent was concentrated under reduced pressure. The residue was purified by column chromatography on silica gel (hexane/ CHCl_3 = 5) to give **1a** (85.0 mg, 91%) as a colorless solid.

mp: 245-249 $^\circ\text{C}$ (decomp.); ^1H NMR (CDCl_3): δ 7.92 (dd, J = 0.7, 8.1 Hz, 2H), 7.69 (dd, J = 7.1, 8.1 Hz, 2H), 7.30 (dd, J = 0.7, 7.1 Hz, 2H), 6.83-6.78(m, 8H), 6.46 (ddd, J = 3.5, 5.0, 8.5 Hz, 4H), 6.39 (s, 4H), 6.38 (br. d, J = 8.5 Hz, 4H); ^{13}C NMR (CDCl_3): δ 152.48, 141.18, 138.15, 136.08, 134.04, 132.47, 130.80, 130.67, 128.41, 126.98, 126.11, 125.69, 123.53, 81.82; IR (KBr): 3107, 3048, 3029, 2925, 1944, 1620, 1594, 1581, 1495, 1489, 1431, 878, 806, 796, 766, 722, 645 cm^{-1} ; LR-MS (FD) m/z (%): 508.20 (9), 507.20 (43), 506.20 (M^+ , bp); HR-MS (FD): [M^+] calcd. for $\text{C}_{40}\text{H}_{26}$, 506.20345; found, 506.20193.

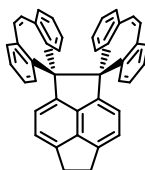
5,6-Bis(5-hydroxydibenzo[*a,d*]cycloheptatrien-5-yl)acenaphthene **7b**.**7b**

To a suspension of 5,6-dibromoacenaphthene **13b** (5.00 g, 16.0 mmol) in dry ether (200 mL) was added $n\text{BuLi}$ in hexane (1.60 M, 24.0 mL, 38.4 mmol) at 25 $^\circ\text{C}$. The mixture was stirred for 1 h at 25 $^\circ\text{C}$, and added dibenzosuberenone (7.94 g, 38.5 mmol) was added. After stirring for 18 h at 25 $^\circ\text{C}$, the mixture was diluted with water, and extracted with CH_2Cl_2 . The organic layer was washed with water and brine, and dried over Na_2SO_4 . After filtration, the solvent was concentrated under reduced pressure. The residue was purified by reprecipitation (CHCl_3 /hexane) and short column chromatography on silica gel (CH_2Cl_2) to give **14b** (6.66 g, 73%) as a colorless solid.

mp: 264-273 $^\circ\text{C}$ (decomp.); ^1H NMR (CDCl_3): δ 7.99 (dd, J = 1.2, 7.9 Hz, 2H), 7.94 (dd, J = 1.2, 7.9 Hz, 2H), 7.70 (ddd, J = 1.3, 7.9, 8.7 Hz, 2H), 7.39 (ddd, J = 1.2, 7.5, 8.7 Hz, 2H), 7.26 (ddd, J = 1.3,

7.9, 8.6 Hz, 2H), 7.07 (dd, $J = 1.3, 7.5$ Hz, 2H), 6.99 (ddd, $J = 1.2, 7.5, 8.6$ Hz, 2H), 6.77 (dd, $J = 1.3, 7.5$ Hz, 2H), 6.73 (d, $J = 7.4$ Hz, 2H), 6.62 (d, $J = 7.4$, 2H), 5.68 (d, $J = 11.4$ Hz, 2H), 5.59 (d, $J = 11.4$ Hz, 2H), 3.30-3.13 (m, 4H), 1.07 (s, 2H); ^{13}C NMR (CDCl_3): δ 149.59, 145.90, 139.70, 138.33, 135.49, 134.92, 134.34, 132.00, 131.39, 130.37, 129.19, 128.06, 127.69, 127.35, 126.60, 126.29, 125.20, 121.72, 116.94, 79.12, 29.83; IR (KBr): 3553, 3059, 3018, 3001, 2932, 1597, 1480, 1446, 1435, 1311, 1217, 1154, 1034, 1022, 790, 770, 763, 653 cm^{-1} ; LR-MS (FD) m/z (%): 568.21 (12), 567.20 (47), 566.20 (M^+ , bp); HR-MS (FD): [M^+] calcd. for $\text{C}_{42}\text{H}_{30}\text{O}_2$, 566.22458; found, 566.22575.

Dispiro[(dibenzo[*a,d*]cycloheptatriene)-5,1'-pyracene-2',5''-(dibenzo[*a,d*]cycloheptatriene)] **1b**.

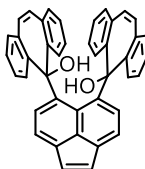


1b

To a suspension of **14b** (1.32 g, 2.32 mmol) in HFIP (5 mL) and dry CH_2Cl_2 (5 mL) was added TfOH (2.10 mL, 23.9 mmol) at 24 °C. The mixture was stirred for 2 h at 24 °C, and the solvent was evaporated. To the residue were added dry MeCN (20 mL), and activated Zn powder (22.8 g, 348 mmol). After stirring for 2 h at 24 °C, the mixture was diluted with water, and extracted with CH_2Cl_2 . The organic layer was washed with water and brine, and dried over Na_2SO_4 . After filtration, the solvent was concentrated under reduced pressure. The residue was purified by short column chromatography on silica gel (CH_2Cl_2) to give **1b** (1.07 g, 87%) as a colorless solid.

mp: 250-260 °C (decomp.); ^1H NMR (CDCl_3): δ 7.46 (d, $J = 7.0$ Hz, 2H), 7.27 (d, $J = 7.0$ Hz, 2H), 6.81-6.77 (m, 8H), 6.54 (br. d, $J = 8.4$ Hz, 4H), 6.46 (ddd, $J = 3.6, 4.9, 8.4$ Hz, 4H), 6.38 (s, 4H), 3.63 (s, 4H); ^{13}C NMR (CDCl_3): δ 147.22, 142.18, 141.19, 137.88, 136.65, 135.67, 133.76, 132.55, 130.48, 127.87, 126.13, 125.53, 121.25, 86.30, 31.83; IR (KBr): 3107, 3027, 2917, 1919, 1623, 1496, 1428, 1068, 877, 840, 808, 799, 769, 724, 690, 646 cm^{-1} ; LR-MS (FD) m/z (%): 534.21 (11), 533.20 (49), 532.20 (M^+ , bp); HR-MS (FD): [M^+] calcd. for $\text{C}_{42}\text{H}_{28}$, 532.21910; found, 532.21825.

5,6-Bis(5-hydroxydibenzo[*a,d*]cycloheptatrien-5-yl)acenaphthylene **7c**.



7c

To a suspension of 5,6-dibromoacenaphthylene **13c** (60.3 mg, 1.94 mmol) in dry ether (50 mL) was added $n\text{BuLi}$ in hexane (1.64 M, 2.80 mL, 4.67 mmol) at 25 °C. After stirring for 1 h at 25 °C, dibenzosuberenone (96.4 mg, 4.67 mmol) was added, and the mixture was refluxed for 5 h. Then, the mixture was cooled to 25 °C, and diluted with water. The resulting mixture was extracted with CHCl_3 .

The organic layer was washed with water and brine, and dried over MgSO₄. After filtration, the solvent was concentrated under reduced pressure. The residue was purified by reprecipitation (CHCl₃/hexane) and column chromatography on silica gel (hexane/EtOAc = 10) to give **14c** (46.9 mg, 43%) as a pale yellow solid.

mp: 281-290 °C (decomp.); ¹H NMR (CDCl₃): δ 7.99 (dd, J = 1.2, 8.0 Hz, 2H), 7.92 (dd, J = 1.2, 8.1 Hz, 2H), 7.71 (ddd, J = 1.3, 8.0, 8.7 Hz, 2H), 7.41 (ddd, J = 1.2, 7.5, 8.7, 2H), 7.27 (ddd, J = 1.3, 8.1, 8.6 Hz, 2H), 7.09 (dd, J = 1.3, 7.5 Hz, 2H), 7.02 (ddd, J = 1.2, 7.5, 8.6 Hz, 2H), 7.00 (d, J = 7.2 Hz, 2H), 6.80 (dd, J = 1.3, 7.5 Hz, 2H), 6.71 (s, 2H), 6.65 (d, J = 7.2 Hz, 2H), 5.73 (d, J = 11.4 Hz, 2H), 5.69 (d, J = 11.4 Hz, 2H), 1.11 (s, 2H); ¹³C NMR (CDCl₃): δ 149.11, 142.13, 139.73, 139.42, 134.60, 134.48, 132.04, 130.83, 130.24, 129.67, 128.756, 128.32, 128.09, 127.79, 127.51, 127.40, 126.84, 126.01, 125.44, 121.70, 121.46, 79.15; IR (KBr): 3558, 3059, 3018, 2922, 1620, 1596, 1477, 1434, 1315, 1218, 1152, 1132, 1037, 836, 792, 761, 746, 671, 656 cm⁻¹; LR-MS (FD) m/z (%): 566.20 (13), 565.20 (46), 564.19 (M⁺,bp), 547.18 (11), 546.18 (19); HR-MS (FD): [M⁺] calcd. for C₄₂H₂₈O₂, 564.20893; found, 564.20734.

Dispiro[(dibenzo[*a,d*]cycloheptatriene)-5,1'-(1',2'-dihydropyracylene)-2',5''-(dibenzo[*a,d*]cycloheptatriene)] **1c**.

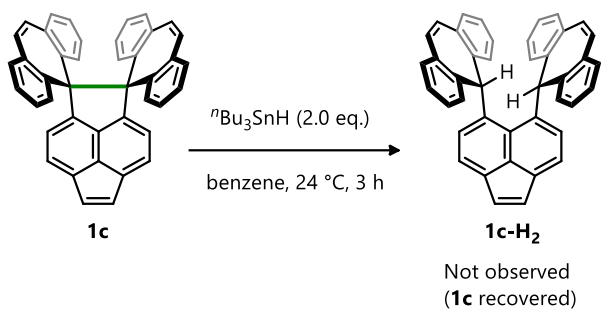


1c

To a suspension of **14c** (188 mg, 332 μmol) in HFIP (6 mL) was added TMSClO₄ in toluene (0.79 M, 1.70 mL, 1.33 mmol) at 24 °C. The mixture was stirred for 1 h at 24 °C, and the solvent was evaporated. To the residue were added dry MeCN (20 mL) and activated Zn powder (3.27 g). After stirring for 30 min at 24 °C, the mixture was diluted with water, and extracted with CHCl₃. The organic layer was washed with water and brine, and dried over MgSO₄. After filtration, the solvent was concentrated under reduced pressure. The residue was purified by reprecipitation (CHCl₃/MeOH) and column chromatography on silica gel (hexane/CHCl₃ = 5) to give **1c** (77.8 mg, 50%) as a yellow solid.

mp: 250-258 °C (decomp.); ¹H NMR (CDCl₃): δ 7.97 (d, J = 7.1 Hz, 2H), 7.43 (d, J = 7.1 Hz, 2H), 7.31 (s, 2H), 6.83-6.78 (m, 8H), 6.46-6.43 (m, 8H), 6.41 (s, 4H); ¹³C NMR (CDCl₃): δ 153.22, 140.70, 136.04, 135.66, 133.72, 132.57, 130.69, 129.43, 127.64, 127.01, 126.24, 125.99, 125.78, 87.46; ¹H NMR (CD₂Cl₂): δ 8.01 (d, J = 7.1 Hz, 2H), 7.43 (d, J = 7.1 Hz, 2H), 7.34 (s, 2H), 6.89-6.80 (m, 8H), 6.52-6.47 (m, 8H), 6.46 (s, 4H); ¹³C NMR (CD₂Cl₂): δ 153.18, 140.76, 136.14, 135.65, 133.65, 133.61, 132.52, 130.64, 129.37, 127.57, 126.85, 126.19, 126.02, 125.72, 87.30; IR (KBr): 3037, 2923, 2853, 1924, 1619, 1488, 1466, 1419, 1083, 953, 846, 835, 770, 724, 719, 677, 646 cm⁻¹; LR-MS (FD) m/z (%): 532.20 (12), 531.20 (M⁺, bp); HR-MS (FD): [M⁺] calcd. for C₄₂H₂₆, 530.20345; found, 530.20345.

- Attempts to trap the bond dissociated species.



To a suspension of **1c** (20.0 mg, 37.7 μmol) in benzene (4 mL) was added $n\text{Bu}_3\text{SnH}$ (20 μL , 744 μmol) at 24 $^\circ\text{C}$. The mixture was stirred for 3 h at 24 $^\circ\text{C}$, and the solvent was evaporated. The residue was purified by column chromatography on silica gel (hexane/ $\text{CHCl}_3 = 3$) to recover **1c** (19.7 mg, 99%) as a yellow solid.

X-ray analyses

Data collection was conducted with a Rigaku Mercury 70 diffractometer (Mo-K α radiation, $\lambda = 0.71075 \text{ \AA}$). The structure was solved by the direct method (SIR2007) and refined by the full-matrix least-squares method on F^2 with anisotropic temperature factors for non-hydrogen atoms. All the hydrogen atoms were located at the calculated positions and refined with riding.

Crystal data for 1a

Crystals were obtained by recrystallizing from CHCl₃/hexane. MF: C₄₀H₂₆, FW: 506.65, colorless platelet, 0.500 x 0.400 x 0.200 mm³

At 120 K

triclinic $P\bar{1}$, $a = 10.902(2) \text{ \AA}$, $b = 15.063(2) \text{ \AA}$, $c = 23.622(3) \text{ \AA}$, $\alpha = 98.955(3)^\circ$, $\beta = 90.783(2)^\circ$, $\gamma = 94.699(2)^\circ$, $V = 3817.7(9) \text{ \AA}^3$, $\rho(Z = 6) = 1.322 \text{ g/cm}^3$. A total of 29355 reflections ($2\theta_{\text{max}} = 55.0^\circ$) were measured at $T = 120 \text{ K}$. Numerical absorption correction was applied ($\mu = 0.748 \text{ cm}^{-1}$). The final $R1$ and $wR2$ values are 0.0488 ($I > 2\sigma I$) and 0.1247 (all data) for 14838 reflections and 1081 parameters. Estimated standard deviations are 0.002-0.004 \AA for bond length and 0.11-0.3 $^\circ$ for angles, respectively. CCDC 1586191

At 160 K

triclinic $P\bar{1}$, $a = 10.9156(4) \text{ \AA}$, $b = 15.0873(8) \text{ \AA}$, $c = 23.660(2) \text{ \AA}$, $\alpha = 98.975(4)^\circ$, $\beta = 90.724(3)^\circ$, $\gamma = 94.562(3)^\circ$, $V = 3835.4(4) \text{ \AA}^3$, $\rho(Z = 6) = 1.316 \text{ g/cm}^3$. A total of 29501 reflections ($2\theta_{\text{max}} = 55.0^\circ$) were measured at $T = 160 \text{ K}$. Numerical absorption correction was applied ($\mu = 0.744 \text{ cm}^{-1}$). The final $R1$ and $wR2$ values are 0.0485 ($I > 2\sigma I$) and 0.1257 (all data) for 14920 reflections and 1081 parameters. Estimated standard deviations are 0.002-0.004 \AA for bond length and 0.11-0.3 $^\circ$ for angles, respectively. CCDC 1586192

At 200 K

triclinic $P\bar{1}$, $a = 10.931(2) \text{ \AA}$, $b = 15.103(3) \text{ \AA}$, $c = 23.692(5) \text{ \AA}$, $\alpha = 98.979(4)^\circ$, $\beta = 90.644(3)^\circ$, $\gamma = 94.544(3)^\circ$, $V = 3850(2) \text{ \AA}^3$, $\rho(Z = 6) = 1.311 \text{ g/cm}^3$. A total of 29608 reflections ($2\theta_{\text{max}} = 55.0^\circ$) were measured at $T = 200 \text{ K}$. Numerical absorption correction was applied ($\mu = 0.741 \text{ cm}^{-1}$). The final $R1$ and $wR2$ values are 0.0507 ($I > 2\sigma I$) and 0.1322 (all data) for 14970 reflections and 1081 parameters. Estimated standard deviations are 0.002-0.004 \AA for bond length and 0.11-0.3 $^\circ$ for angles, respectively. CCDC 1567390

At 240 K

triclinic $P\bar{1}$, $a = 10.949(2) \text{ \AA}$, $b = 15.115(3) \text{ \AA}$, $c = 23.719(4) \text{ \AA}$, $\alpha = 98.957(3)^\circ$, $\beta = 90.541(3)^\circ$, $\gamma =$

94.657(2) °, $V = 3863.7(12) \text{ \AA}^3$, $\rho(Z = 6) = 1.306 \text{ g/cm}^3$. A total of 29835 reflections ($2\theta_{\text{max}} = 55.0^\circ$) were measured at $T = 240 \text{ K}$. Numerical absorption correction was applied ($\mu = 0.739 \text{ cm}^{-1}$). The final $R1$ and $wR2$ value are 0.0520 ($I > 2\sigma I$) and 0.1396 (all data) for 15037 reflections and 1081 parameters. Estimated standard derivatives are 0.002-0.005 Å for bond length and 0.12-0.3 ° for angles, respectively. CCDC 1567391

At 280 K

triclinic $P\bar{1}$, $a = 10.967(3) \text{ \AA}$, $b = 15.141(4) \text{ \AA}$, $c = 23.757(5) \text{ \AA}$, $\alpha = 98.935(5)^\circ$, $\beta = 90.513(5)^\circ$, $\gamma = 94.649(3)^\circ$, $V = 3883(2) \text{ \AA}^3$, $\rho(Z = 6) = 1.311 \text{ g/cm}^3$. A total of 29928 reflections ($2\theta_{\text{max}} = 55.0^\circ$) were measured at $T = 280 \text{ K}$. Numerical absorption correction was applied ($\mu = 0.735 \text{ cm}^{-1}$). The final $R1$ and $wR2$ value are 0.0522 ($I > 2\sigma I$) and 0.1423 (all data) for 14970 reflections and 1081 parameters. Estimated standard derivatives are 0.002-0.005 Å for bond length and 0.11-0.3 ° for angles, respectively. CCDC 1567392

At 320 K

triclinic $P\bar{1}$, $a = 10.976(2) \text{ \AA}$, $b = 15.158(3) \text{ \AA}$, $c = 23.792(5) \text{ \AA}$, $\alpha = 98.983(5)^\circ$, $\beta = 90.449(3)^\circ$, $\gamma = 94.482(3)^\circ$, $V = 3897(2) \text{ \AA}^3$, $\rho(Z = 6) = 1.295 \text{ g/cm}^3$. A total of 29993 reflections ($2\theta_{\text{max}} = 55.0^\circ$) were measured at $T = 320 \text{ K}$. Numerical absorption correction was applied ($\mu = 0.732 \text{ cm}^{-1}$). The final $R1$ and $wR2$ value are 0.0544 ($I > 2\sigma I$) and 0.1467 (all data) for 15175 reflections and 1081 parameters. Estimated standard derivatives are 0.002-0.005 Å for bond length and 0.12-0.3 ° for angles, respectively. CCDC 1567392

At 360 K

triclinic $P\bar{1}$, $a = 10.985(3) \text{ \AA}$, $b = 15.180(4) \text{ \AA}$, $c = 23.813(6) \text{ \AA}$, $\alpha = 98.959(7)^\circ$, $\beta = 90.456(5)^\circ$, $\gamma = 94.475(4)^\circ$, $V = 3910(2) \text{ \AA}^3$, $\rho(Z = 6) = 1.291 \text{ g/cm}^3$. A total of 30135 reflections ($2\theta_{\text{max}} = 55.0^\circ$) were measured at $T = 360 \text{ K}$. Numerical absorption correction was applied ($\mu = 0.730 \text{ cm}^{-1}$). The final $R1$ and $wR2$ value are 0.0553 ($I > 2\sigma I$) and 0.1591 (all data) for 15215 reflections and 1081 parameters. Estimated standard derivatives are 0.003-0.006 Å for bond length and 0.13-0.4 ° for angles, respectively. CCDC 1567394

At 400 K

triclinic $P\bar{1}$, $a = 11.009(3) \text{ \AA}$, $b = 15.203(4) \text{ \AA}$, $c = 23.865(6) \text{ \AA}$, $\alpha = 98.972(6)^\circ$, $\beta = 90.356(5)^\circ$, $\gamma = 94.448(4)^\circ$, $V = 3933(2) \text{ \AA}^3$, $\rho(Z = 6) = 1.283 \text{ g/cm}^3$. A total of 30269 reflections ($2\theta_{\text{max}} = 55.0^\circ$) were measured at $T = 400 \text{ K}$. Numerical absorption correction was applied ($\mu = 0.726 \text{ cm}^{-1}$). The final $R1$ and $wR2$ value are 0.0591 ($I > 2\sigma I$) and 0.1620 (all data) for 15305 reflections and 1081 parameters. Estimated standard derivatives are 0.003-0.006 Å for bond length and 0.13-0.4 ° for angles, respectively. CCDC 1567395

Crystal data for **1b**

Crystals were obtained by recrystallizing from CHCl₃/hexane. MF: C₄₂H₂₈, FW: 532.68, colorless block, 0.400 x 0.200 x 0.200 mm³

At 200 K

monoclinic $P2_1/c$, $a = 12.782(2)$ Å, $b = 9.228(2)$ Å, $c = 24.084(4)$ Å, $\beta = 100.159(3)$ °, $V = 2796.2(8)$ Å³, $\rho(Z = 4) = 1.265$ g/cm³. A total of 20262 reflections ($2\theta_{\max} = 55.0$ °) were measured at $T = 200$ K. Numerical absorption correction was applied ($\mu = 0.715$ cm⁻¹). The final R and $wR2$ value are 0.0633 ($I > 2\sigma I$) and 0.1968 (all data) for 5484 reflections and 379 parameters. Estimated standard derivatives are 0.003-0.006 Å for bond length and 0.14-0.4 ° for angles, respectively. CCDC 1567396

At 240 K

monoclinic $P2_1/c$, $a = 12.789(3)$ Å, $b = 9.229(2)$ Å, $c = 24.088(5)$ Å, $\beta = 100.106(3)$ °, $V = 2798.9(11)$ Å³, $\rho(Z = 4) = 1.264$ g/cm³. A total of 20447 reflections ($2\theta_{\max} = 55.0$ °) were measured at $T = 240$ K. Numerical absorption correction was applied ($\mu = 0.714$ cm⁻¹). The final R and $wR2$ value are 0.0711 ($I > 2\sigma I$) and 0.2379 (all data) for 5407 reflections and 379 parameters. Estimated standard derivatives are 0.003-0.008 Å for bond length and 0.15-0.5 ° for angles, respectively. CCDC 1567397

At 280 K

monoclinic $P2_1/c$, $a = 12.791(3)$ Å, $b = 9.230(2)$ Å, $c = 24.091(5)$ Å, $\beta = 100.153(3)$ °, $V = 2799.5(11)$ Å³, $\rho(Z = 4) = 1.264$ g/cm³. A total of 20755 reflections ($2\theta_{\max} = 55.0$ °) were measured at $T = 280$ K. Numerical absorption correction was applied ($\mu = 0.714$ cm⁻¹). The final R and $wR2$ value are 0.0684 ($I > 2\sigma I$) and 0.2052 (all data) for 5486 reflections and 379 parameters. Estimated standard derivatives are 0.003-0.007 Å for bond length and 0.14-0.4 ° for angles, respectively. CCDC 1567398

At 320 K

monoclinic $P2_1/c$, $a = 12.780(5)$ Å, $b = 9.232(3)$ Å, $c = 24.074(9)$ Å, $\beta = 100.101(5)$ °, $V = 2796(2)$ Å³, $\rho(Z = 4) = 1.265$ g/cm³. A total of 20388 reflections ($2\theta_{\max} = 55.0$ °) were measured at $T = 320$ K. Numerical absorption correction was applied ($\mu = 0.715$ cm⁻¹). The final R and $wR2$ value are 0.0702 ($I > 2\sigma I$) and 0.2455 (all data) for 5435 reflections and 379 parameters. Estimated standard derivatives are 0.003-0.008 Å for bond length and 0.15-0.5 ° for angles, respectively. CCDC 1567399

At 360 K

monoclinic $P2_1/c$, $a = 12.784(4)$ Å, $b = 9.232(3)$ Å, $c = 24.073(8)$ Å, $\beta = 100.091(5)$ °, $V = 2797(2)$ Å³, $\rho(Z = 4) = 1.265$ g/cm³. A total of 20693 reflections ($2\theta_{\max} = 55.0$ °) were measured at $T = 360$ K.

Numerical absorption correction was applied ($\mu = 0.715 \text{ cm}^{-1}$). The final R_I and wR_2 value are 0.0699 ($I > 2\sigma I$) and 0.2074 (all data) for 5486 reflections and 379 parameters. Estimated standard derivatives are 0.003–0.007 Å for bond length and 0.14–0.5 ° for angles, respectively. CCDC 1567400

At 400 K

monoclinic $P2_1/c$, $a = 12.781(5) \text{ Å}$, $b = 9.231(3) \text{ Å}$, $c = 24.071(9) \text{ Å}$, $\beta = 100.096(5)^\circ$, $V = 2796(2) \text{ Å}^3$, $\rho(Z = 4) = 1.265 \text{ g/cm}^3$. A total of 20734 reflections ($2\theta_{\text{max}} = 55.0^\circ$) were measured at $T = 400 \text{ K}$. Numerical absorption correction was applied ($\mu = 0.715 \text{ cm}^{-1}$). The final R_I and wR_2 value are 0.0700 ($I > 2\sigma I$) and 0.2228 (all data) for 5476 reflections and 379 parameters. Estimated standard derivatives are 0.003–0.008 Å for bond length and 0.15–0.5 ° for angles, respectively. CCDC 1567401

Crystal data for 1c

Crystals were obtained by recrystallizing from $\text{CHCl}_3/\text{hexane}$. MF: $\text{C}_{42}\text{H}_{26}$, FW: 530.67

At 100 K

orange platelet, $0.500 \times 0.200 \times 0.100 \text{ mm}^3$, orthorhombic $Pbca$, $a = 17.960(3) \text{ Å}$, $b = 15.813(3) \text{ Å}$, $c = 18.523(4) \text{ Å}$, $V = 5261(2) \text{ Å}^3$, $\rho(Z = 8) = 1.340 \text{ g/cm}^3$. A total of 37745 reflections ($2\theta_{\text{max}} = 55.0^\circ$) were measured at $T = 100 \text{ K}$. Numerical absorption correction was applied ($\mu = 0.758 \text{ cm}^{-1}$). The final R_I and wR_2 value are 0.0419 ($I > 2\sigma I$) and 0.1033 (all data) for 5162 reflections and 379 parameters. Estimated standard derivatives are 0.0018–0.003 Å for bond length and 0.10–0.15 ° for angles, respectively. CCDC 1586193

At 120 K

orange platelet, $0.500 \times 0.200 \times 0.100 \text{ mm}^3$, orthorhombic $Pbca$, $a = 17.960(3) \text{ Å}$, $b = 15.820(3) \text{ Å}$, $c = 18.509(3) \text{ Å}$, $V = 5259(2) \text{ Å}^3$, $\rho(Z = 8) = 1.340 \text{ g/cm}^3$. A total of 37892 reflections ($2\theta_{\text{max}} = 55.0^\circ$) were measured at $T = 120 \text{ K}$. Numerical absorption correction was applied ($\mu = 0.759 \text{ cm}^{-1}$). The final R_I and wR_2 value are 0.0395 ($I > 2\sigma I$) and 0.0986 (all data) for 5158 reflections and 379 parameters. Estimated standard derivatives are 0.0016–0.002 Å for bond length and 0.09–0.13 ° for angles, respectively. CCDC 1586194

At 160 K

orange platelet, $0.500 \times 0.200 \times 0.100 \text{ mm}^3$, orthorhombic $Pbca$, $a = 17.977(3) \text{ Å}$, $b = 15.846(3) \text{ Å}$, $c = 18.532(3) \text{ Å}$, $V = 5279(2) \text{ Å}^3$, $\rho(Z = 8) = 1.335 \text{ g/cm}^3$. A total of 18440 reflections ($2\theta_{\text{max}} = 55.0^\circ$) were measured at $T = 160 \text{ K}$. Numerical absorption correction was applied ($\mu = 0.756 \text{ cm}^{-1}$). The final R_I and wR_2 value are 0.0415 ($I > 2\sigma I$) and 0.1046 (all data) for 5162 reflections and 379 parameters. Estimated standard derivatives are 0.0018–0.003 Å for bond length and 0.10–0.15 ° for

angles, respectively. CCDC 1586195

At 200 K

orange platelet, $0.500 \times 0.200 \times 0.100 \text{ mm}^3$, orthorhombic $Pbca$, $a = 17.983(3) \text{ \AA}$, $b = 15.870(3) \text{ \AA}$, $c = 18.550(3) \text{ \AA}$, $V = 5294(2) \text{ \AA}^3$, $\rho(Z = 8) = 1.332 \text{ g/cm}^3$. A total of 38119 reflections ($2\theta_{\text{max}} = 55.0^\circ$) were measured at $T = 200 \text{ K}$. Numerical absorption correction was applied ($\mu = 0.754 \text{ cm}^{-1}$). The final $R1$ and $wR2$ value are 0.0415 ($I > 2\sigma I$) and 0.1032 (all data) for 5190 reflections and 379 parameters. Estimated standard derivatives are 0.0016-0.003 \AA for bond length and 0.09-0.15 $^\circ$ for angles, respectively. CCDC 1567402

At 240 K

orange platelet, $0.500 \times 0.200 \times 0.100 \text{ mm}^3$, orthorhombic $Pbca$, $a = 18.005(3) \text{ \AA}$, $b = 15.899(3) \text{ \AA}$, $c = 18.579(3) \text{ \AA}$, $V = 5318(2) \text{ \AA}^3$, $\rho(Z = 8) = 1.325 \text{ g/cm}^3$. A total of 18695 reflections ($2\theta_{\text{max}} = 55.0^\circ$) were measured at $T = 240 \text{ K}$. Numerical absorption correction was applied ($\mu = 0.750 \text{ cm}^{-1}$). The final $R1$ and $wR2$ value are 0.0429 ($I > 2\sigma I$) and 0.1092 (all data) for 5194 reflections and 379 parameters. Estimated standard derivatives are 0.0018-0.003 \AA for bond length and 0.10-0.16 $^\circ$ for angles, respectively. CCDC 1567403

At 280 K

orange platelet, $0.500 \times 0.200 \times 0.100 \text{ mm}^3$, orthorhombic $Pbca$, $a = 18.030(3) \text{ \AA}$, $b = 15.931(3) \text{ \AA}$, $c = 18.613(3) \text{ \AA}$, $V = 5346(2) \text{ \AA}^3$, $\rho(Z = 8) = 1.318 \text{ g/cm}^3$. A total of 19536 reflections ($2\theta_{\text{max}} = 55.0^\circ$) were measured at $T = 280 \text{ K}$. Numerical absorption correction was applied ($\mu = 0.746 \text{ cm}^{-1}$). The final $R1$ and $wR2$ value are 0.0445 ($I > 2\sigma I$) and 0.1146 (all data) for 5217 reflections and 379 parameters. Estimated standard derivatives are 0.0019-0.003 \AA for bond length and 0.10-0.17 $^\circ$ for angles, respectively. CCDC 1567404

At 320 K

orange platelet, $0.500 \times 0.200 \times 0.100 \text{ mm}^3$, orthorhombic $Pbca$, $a = 18.0425(8) \text{ \AA}$, $b = 15.9563(6) \text{ \AA}$, $c = 18.6292(8) \text{ \AA}$, $V = 5346.2(4) \text{ \AA}^3$, $\rho(Z = 8) = 1.314 \text{ g/cm}^3$. A total of 22457 reflections ($2\theta_{\text{max}} = 55.0^\circ$) were measured at $T = 320 \text{ K}$. Numerical absorption correction was applied ($\mu = 0.744 \text{ cm}^{-1}$). The final $R1$ and $wR2$ value are 0.0457 ($I > 2\sigma I$) and 0.1150 (all data) for 5241 reflections and 379 parameters. Estimated standard derivatives are 0.0019-0.003 \AA for bond length and 0.10-0.18 $^\circ$ for angles, respectively. CCDC 1567405

At 360 K

orange platelet, $0.500 \times 0.200 \times 0.100 \text{ mm}^3$, orthorhombic $Pbca$, $a = 18.054(3) \text{ \AA}$, $b = 15.970(3) \text{ \AA}$,

$c = 18.644(3) \text{ \AA}$, $V = 5375(2) \text{ \AA}^3$, $\rho(Z = 8) = 1.311 \text{ g/cm}^3$. A total of 23249 reflections ($2\theta_{\text{max}} = 55.0^\circ$) were measured at $T = 360 \text{ K}$. Numerical absorption correction was applied ($\mu = 0.742 \text{ cm}^{-1}$). The final $R1$ and $wR2$ value are 0.0465 ($I > 2\sigma I$) and 0.1179 (all data) for 5251 reflections and 379 parameters. Estimated standard derivatives are 0.0019-0.003 \AA for bond length and 0.11-0.19 $^\circ$ for angles, respectively. CCDC 1567406

At 400 K

red platelet, $0.500 \times 0.200 \times 0.100 \text{ mm}^3$, orthorhombic $Pbca$, $a = 18.076(3) \text{ \AA}$, $b = 15.999(3) \text{ \AA}$, $c = 18.676(4) \text{ \AA}$, $V = 5401(2) \text{ \AA}^3$, $\rho(Z = 8) = 1.305 \text{ g/cm}^3$. A total of 22281 reflections ($2\theta_{\text{max}} = 55.0^\circ$) were measured at $T = 400 \text{ K}$. Numerical absorption correction was applied ($\mu = 0.739 \text{ cm}^{-1}$). The final $R1$ and $wR2$ value are 0.0500 ($I > 2\sigma I$) and 0.1245 (all data) for 5280 reflections and 379 parameters. Estimated standard derivatives are 0.002-0.004 \AA for bond length and 0.11-0.2 $^\circ$ for angles, respectively. CCDC 1567407

2-5. References

- [1] T. Suzuki, Y. Uchimura, Y. Ishigaki, T. Takeda, R. Katoono, H. Kawai, K. Fujiwara, A. Nagaki, J. Yoshida, *Chem. Lett.* **2012**, *41*, 541–543.
- [2] T. Takeda, H. Kawai, R. Herges, E. Mucke, Y. Sawai, K. Murakoshi, K. Fujiwara, T. Suzuki, *Tetrahedron Lett.* **2009**, *50*, 3693–3697.
- [3] A. A. Zavitsas, *J. Phys. Chem. A* **2003**, *107*, 897–898.
- [4] D. Cho, Y. Ikabata, T. Yoshikawa, Y. L. Jin, H. Nakai, *Bull. Chem. Soc. Jpn.* **2015**, *88*, 1636–1641.
- [5] T. R. Battersby, R. VernonClark, J. S. Siegel, *J. Am. Chem. Soc.* **1997**, *119*, 7048–7054.
- [6] K. K. Baldrige, Y. Kasahara, K. Ogawa, J. S. Siegel, K. Tanaka, F. Toda, *J. Am. Chem. Soc.* **1998**, *120*, 6167–6168.
- [7] B. Kahr, C. A. Mitchell, J. M. Chance, R. V. Clark, P. Gantzel, K. K. Baldrige, J. S. Siegel, *J. Am. Chem. Soc.* **1995**, *117*, 4479–4482.
- [8] J. L. Adcock, A. A. Gakh, J. L. Pollitte, C. Woods, *J. Am. Chem. Soc.* **1992**, *114*, 3980–3981.
- [9] Y. Uchimura, T. Shimajiri, Y. Ishigaki, R. Katoono, T. Suzuki, *Chem. Commun.* **2018**, *54*, 10300–10303.
- [10] E. R. Johnson, S. Keinan, P. Mori-Sánchez, J. Contreras-García, A. J. Cohen, W. Yang, *J. Am. Chem. Soc.* **2010**, *132*, 6498–6506.
- [11] Y. Uchimura, T. Takeda, R. Katoono, K. Fujiwara, T. Suzuki, *Angew. Chem. Int. Ed.* **2015**, *54*, 4010–4013.
- [12] T. Suzuki, J. Nishida, M. Ohkita, T. Tsuji, *Angew. Chem. Int. Ed.* **2000**, *39*, 1804–1806.
- [13] H. Kawai, T. Takeda, K. Fujiwara, M. Wakeshima, Y. Hinatsu, T. Suzuki, *Chem. - A Eur. J.* **2008**, *14*, 5780–5793.
- [14] T. Saitoh, S. Yoshida, J. Ichikawa, *Org. Lett.* **2004**, *6*, 4563–4565.
- [15] M. W. Wong, *Chem. Phys. Lett.* **1996**, *256*, 391–399.
- [16] K. Van Helvoort, W. Knippers, R. Fantoni, S. Stolte, *Chem. Phys.* **1987**, *111*, 445–465.
- [17] S. Kammermeier, R. Herges, P. G. Jones, *Angew. Chem. Int. Ed. Engl.* **1997**, *36*, 1757–1760.
- [18] R. C. Haddon, *J. Am. Chem. Soc.* **1987**, *109*, 1676–1685.
- [19] R. C. Haddon, *J. Phys. Chem. A* **2001**, *105*, 4164–4165.
- [20] W. H. E. Schwarz, K. Ruedenberg, L. Mensching, *J. Am. Chem. Soc.* **1989**, *111*, 6926–6933.
- [21] L. Mensching, W. Von Niessen, P. Valtazanos, K. Ruedenberg, W. H. E. Schwarz, *J. Am. Chem. Soc.* **1989**, *111*, 6933–6941.
- [22] T. Nishiuchi, S. Uno, Y. Hirao, T. Kubo, *J. Org. Chem.* **2016**, *81*, 2106–2112.
- [23] R. F. W. Bader, *Acc. Chem. Res.* **1985**, *18*, 9–15.
- [24] A. D. Becke, K. E. Edgecombe, *J. Chem. Phys.* **1990**, *92*, 5397–5403.

- [25] S. Hayashi, K. Matsuiwa, M. Kitamoto, W. Nakanishi, *J. Phys. Chem. A* **2013**, *117*, 1804–1816.
- [26] D. Doehnert, J. Koutecky, *J. Am. Chem. Soc.* **1980**, *102*, 1789–1796.
- [27] M. J. Frisch, G. W. Trucks, H. B. Schlegel, G. E. Scuseria, M. A. Robb, J. R. Cheeseman, G. Scalmani, V. Barone, B. Mennucci, G. A. Petersson, H. Nakatsuji, M. Caricato, X. Li, H. P. Hratchian, A. F. Izmaylov, J. Bloino, G. Zheng, J. L. Sonnenberg, M. Hada, M. Ehara, K. Toyota, R. Fukuda, J. Hasegawa, M. Ishida, T. Nakajima, Y. Honda, O. Kitao, H. Nakai, T. Vreven, J. Montgomery, J. A., J. E. Peralta, F. Ogliaro, M. Bearpark, J. J. Heyd, E. Brothers, K. N. Kudin, V. N. Staroverov, R. Kobayashi, J. Normand, K. Raghavachari, A. Rendell, J. C. Burant, S. S. Iyengar, J. Tomasi, M. Cossi, N. Rega, J. M. Millam, M. Klene, J. E. Knox, J. B. Cross, V. Bakken, C. Adamo, J. Jaramillo, R. Gomperts, R. E. Stratmann, O. Yazyev, A. J. Austin, R. Cammi, C. Pomelli, J. W. Ochterski, R. L. Martin, K. Morokuma, V. G. Zakrzewski, G. A. Voth, P. Salvador, J. J. Dannenberg, S. Dapprich, A. D. Daniels, Ö. Farkas, J. B. Foresman, J. V. Ortiz, J. Cioslowski, D. J. Fox, **2013**, Gaussian, Inc., Wallingford CT.
- [28] J. M. Frisch, W. G. Trucks, B. H. Schlegel, E. G. Scuseria, A. M. Robb, R. J. Cheeseman, G. Scalmani, V. Barone, A. G. Petersson, H. Nakatsuji, X. Li, M. Caricato, V. A. Marenich, J. Bloino, G. B. Janesko, R. Gomperts, B. Mennucci, P. H. Hratchian, V. J. Ortiz, F. A. Izmaylov, L. J. Sonnenberg, D. Williams-Young, F. Ding, F. Lipparini, F. Egidi, J. Goings, B. Peng, A. Petrone, T. Henderson, D. Ranasinghe, G. V. Zakrzewski, J. Gao, N. Rega, G. Zheng, W. Liang, M. Hada, M. Ehara, K. Toyota, R. Fukuda, J. Hasegawa, M. Ishida, T. Nakajima, Y. Honda, O. Kitao, H. Nakai, T. Vreven, K. Throssell, A. J. Montgomery, Jr., E. J. Peralta, F. Ogliaro, J. M. Bearpark, J. J. Heyd, N. E. Brothers, N. K. Kudin, N. V. Staroverov, A. T. Keith, R. Kobayashi, J. Normand, K. Raghavachari, P. A. Rendell, C. J. Burant, S. S. Iyengar, J. Tomasi, M. Cossi, M. J. Millam, M. Klene, C. Adamo, R. Cammi, W. J. Ochterski, L. R. Martin, K. Morokuma, O. Farkas, B. J. Foresman, J. D. Fox, **2019**, Gaussian, Inc., Wallingford CT.
- [29] F. Neese, *WIREs Comput. Mol. Sci.* **2012**, *2*, 73–78.
- [30] F. Neese, *WIREs Comput. Mol. Sci.* **2018**, *8*, 4–9.
- [31] T. Lu, F. Chen, *J. Comput. Chem.* **2012**, *33*, 580–592.
- [32] E. D. Glendening, J. K. Badenhop, A. E. Reed, J. E. Carpenter, J. A. Bohmann, C. M. Morales, P. Karafiloglou, C. R. Landis, F. Weinhold, **2018**, Theoretical Chemistry Institute, University of Wisconsin, Madison, WI
- [33] J. M. McBride, *Tetrahedron* **1974**, *30*, 2009–2022.
- [34] L. M. Diamond, F. R. Knight, K. S. Athukorala Arachchige, R. A. M. Randall, M. Bühl, A. M. Z. Slawin, J. D. Woollins, *Eur. J. Inorg. Chem.* **2014**, 1512–1523.

Chapter 3

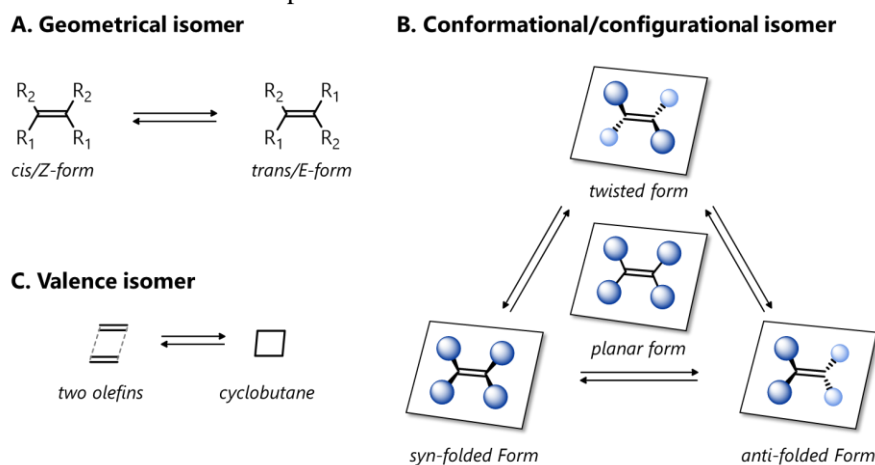
Discovery of Flexible Bonds Based on an Extremely Elongated C–C Single Bond

3-1. Introduction

Strained molecules such as sterically congested polycyclic aromatic hydrocarbons^[1–8] as well as cyclic π -conjugated compounds^[9–15] often exhibit unusual parameters, and thus have attracted much attention due to their potential applications. As described in chapter 2, the author demonstrated that spiro-DBCHT **1a-1c** has an unusual C–C single bond beyond 1.8 Å based on the core-shell strategy.^[16] Then, the author envisaged that such a “hyper covalent bond” should be weak enough to exhibit reversible expansion, contraction, formation, and scission, which could be visualized by X-ray analyses.

Here, C=C double bonds are known to show stimuli-responsive isomerization such as geometrical isomerization, conformational/configurational isomerization and valence isomerization (Scheme 1), which have been used for the development of functional materials and molecular machines, since it changes not only the molecular structure but also the physical properties.

Scheme 1. Isomerization processes of C=C double bond.



In this research, the author focuses on the DBCHT unit, which has been used to construct photoresponsive molecules based on overcrowded ethylenes through *syn/anti* configurational isomerization.^[17,18] Another aspect is a structurally fixed *cis*-stilbene moiety in the DBCHT unit, and thus the intramolecular [2+2] cycloaddition reaction could proceed as in DBCHT-dimer to produce a caged molecule based on a pericyclic reaction (Figure 1).^[19]

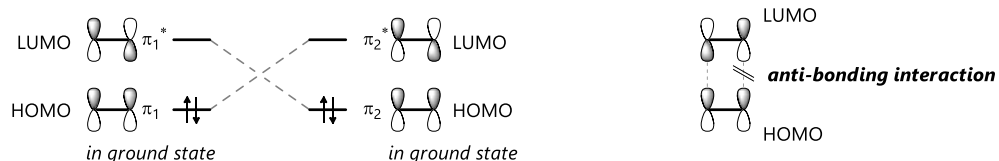
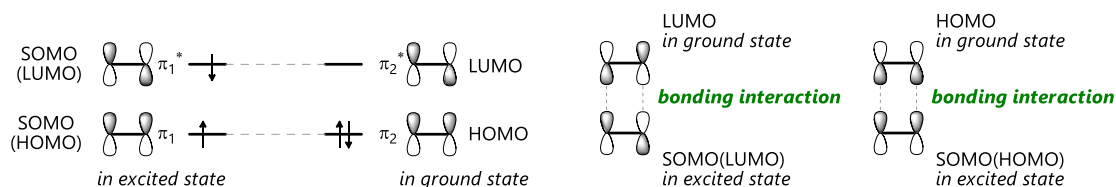
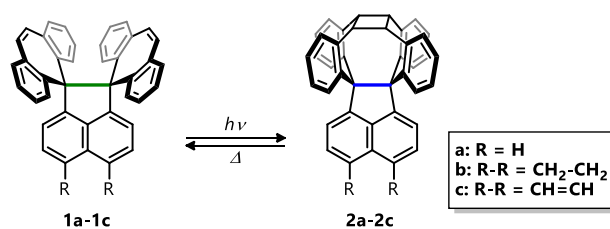
A. Thermal reaction (symmetry forbidden)**B. Photoreaction (photochemically allowed)**

Figure 1. Frontier orbital interaction of [2+2] cycloaddition reaction between C=C double bonds.

The latter reactivity is more interesting from a topochemical point of view, since the solid-state reaction would be applicable for stimuli-responsive systems toward potential applications such as photoswitching, optical recording, and sensing materials.^[20–28] By controlling the crystal packing structure, intermolecular [2+2] cyclization could proceed in a single-crystal-to-single-crystal (SCSC) manner upon photoirradiation, which has been realized by the aid of soft matter/lattices such as ionic crystals, metal–organic frameworks, and coordination polymers.^[29–34] Furthermore, only a few examples exhibit reversible SCSC thermal cleavage of the cyclobutane ring resulting from the SCSC photocycloaddition of two C=C bonds,^[30–32] and none of them are pure neutral organic molecules.

Since *cis*-stilbene moieties connected by an elongated C–C bond face to each other in the outer “shell”-structure of spiro-DBCHT **1a–1c**, as described in chapter 2, the author expects that a reversible SCSC [2+2] photocycloaddition and thermal cycloreversion could proceed in the pure hydrocarbon crystal (Scheme 2). Once a [2+2] photocycloaddition reaction occurs for the spiro-DBCHT **1a–1c**, changes not only in “shell” structures and physical properties but also in the bond length of the “core” C–C bond should be observed. This chapter describes how the reversible formation and scission of C–C bonds in a single crystal can be induced by external stimulation of light and heat, accompanied by reversible expansion and contraction of the elongated Csp^3 – Csp^3 bond and by a change of the HOMO level by ca. 1 eV.

Scheme 2. Structural change between spiro-DBCHT **1** and caged molecules **2**.



3-2. Results and Discussion

3-2-1. Intramolecular Photocyclization

According to the X-ray structures of **1a-1c**,^[16] two DBCHT units are well-overlapped due to π - π interaction with a C---C distance of 3.163(3)-3.357(4) Å between the vinylic carbons. Thus, the author first photoirradiated CHCl₃ solutions of **1a-1c** at around 365 nm, which is assigned to an absorption band of DBCHT units by time-dependent density functional theory (TD-DFT) calculations (Figure 2). As a result, [2+2] photocyclization proceeded quantitatively in all spiro-DBCHT **1a-1c** to produce caged molecules **2a-2c** with a cyclobutene ring, which was monitored by UV/Vis and NMR spectroscopies (Figures 3). Cleavage of the cyclobutane ring in **2a-2c** did not occur upon photoirradiation at any wavelength. Disappearance of *cis*-stilbene moieties results not only in a blue-shift and hypochromic shift of the absorption band, but also in switching of the major chromophores to the acenaphthene ring which is located far from the cyclobutane ring (Figure 2).

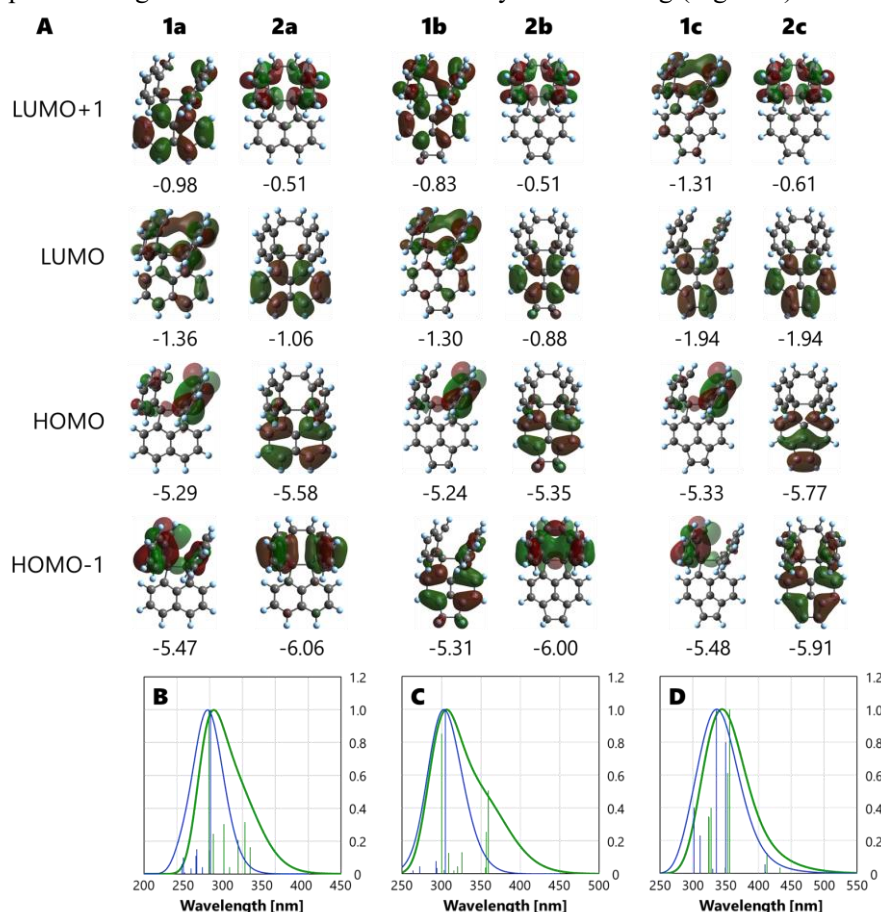


Figure 2. (A) Theoretically obtained Kohn-Sham orbitals (MOs) of the optimized structures by DFT calculations (B3LYP/6-31G*) for **1a-1c** and **2a-2c**. The values of energy level [eV] are shown under the profile of molecular orbitals. Simulated absorption spectra by TD-DFT calculations (B3LYP/6-31G*) of (B) **1a** and **2a**, (C) **1b** and **2b** and (D) **1c** and **2c**; green and blue lines correspond to **1a-1c** and **2a-2c**, respectively.

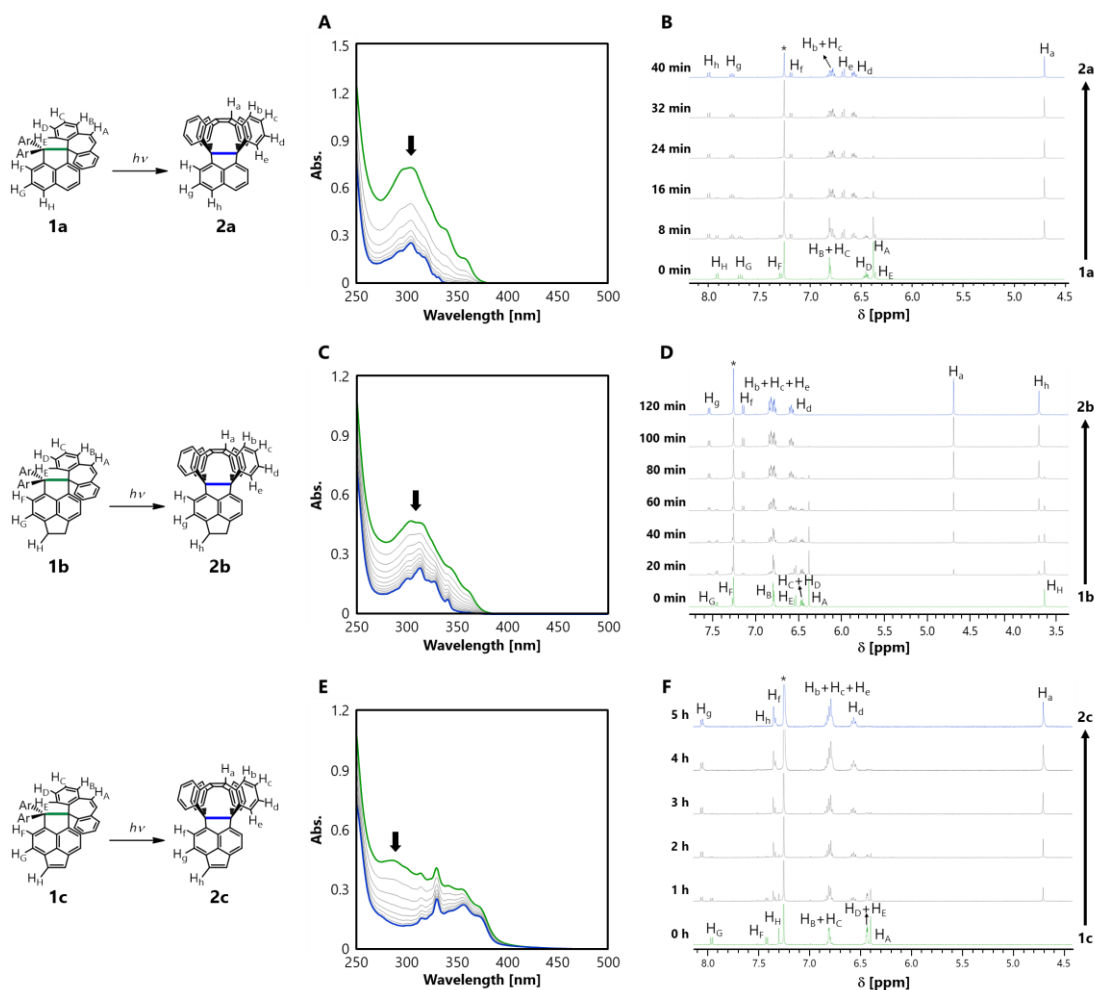


Figure 3. Changes in the UV/Vis spectrum of **1** (green) to **2** (blue) in CHCl_3 (A; **1a** to **2a**, C; **1b** to **2b**, E; **1c** to **2c**) and in the ^1H NMR spectrum of **1** (green) to **2** (blue) in CDCl_3 upon photoirradiation at 365 nm (monochromated light from 150 W Xe lamp, slit width: 10 nm, B; **1a** to **2a**, D; **1b** to **2b**, F; **1c** to **2c**). The residual proton signal of the solvent (CHCl_3 , $\delta=7.26$ ppm) is marked with an asterisk.

Photocyclization reaction proceeded in preparative scale to produce **2** from **1** in CHCl_3 quantitatively (Scheme 3). As expected, photoirradiation by using a LED lamp (375 nm) of a solid-state sample of **1a-1c** also underwent photocycloaddition reaction to **2a-2c** quantitatively. Caged molecule **2a-2c** gave high-quality single crystals suitable for X-ray diffraction measurement. X-ray analyses revealed that **2a-2c** adopt caged structures with a four-membered ring (Scheme 3). A remarkable point is that contraction of the central C–C single bond by as much as about 5%, from 1.720(2)-1.742(2), 1.773(3), and 1.7980(18) Å for spiro-DBCHT **1a**, **1b**, and **1c** to 1.676(6)-1.678(6), 1.7133(16), and 1.7129(19) Å for caged molecules **2a**, **2b**, and **2c**, respectively, was observed at 200 K (Table 1).

Scheme 3. Photoirradiation of **1a–1c** with a 375 nm light-emitting diode (yields are for the isolated product), and ORTEP drawings at 200 K of **1a–1c** and **2a–2c**.

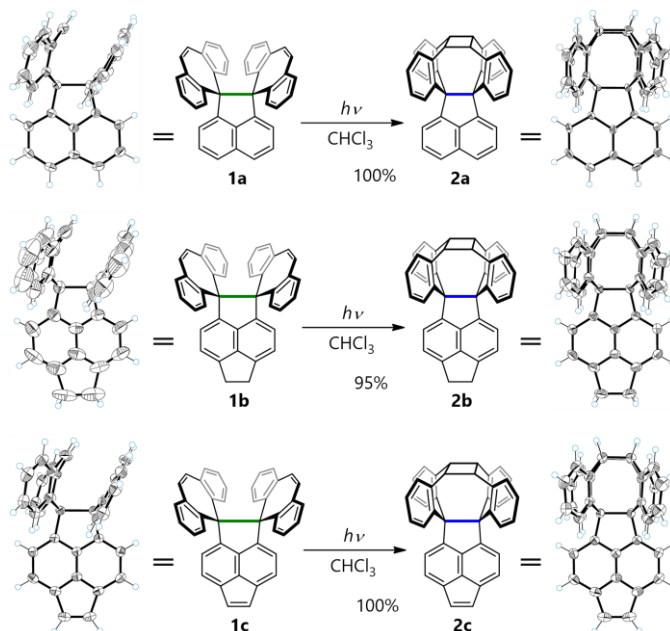


Table 1. Central C–C bond lengths and Raman shifts for **1a–1c** and **2a–2c** determined by X-ray analysis (at 200 K) and Raman spectroscopy (at 298 K) with single crystals. Theoretically obtained values are based on DFT calculations at the B3LYP/6-31G* level.

		1a	2a	1b	2b	1c	2c
C–C bond length (Å)	Expt.	1.720(2)-1.742(2)	1.676(6)-1.678(6)	1.773(3)	1.7133(16)	1.7980(18)	1.7129(19)
	Calcd.	1.769	1.698	1.826	1.734	1.835	1.737
Raman shift (cm⁻¹)	Expt.	650	653	582	646	587	648
	Calcd.	657	663	631	653	635	658

To verify the bonding nature of the contracted C–C single bond, the author investigated the stretching vibration of caged molecules **2a–2c** by Raman spectroscopy with single crystals at 298 K to attain direct information of the bond strength. Observed Raman shifts corresponding to the central C–C bond were 653, 646, and 648 cm⁻¹ for **2a**, **2b**, and **2c**, respectively, which are consistent with the simulated values (663, 653, and 658 cm⁻¹ without scaling and 637, 627 and 633 cm⁻¹ with a factor^[35] of 0.9613 at B3LYP/6-31G). These experimental values of **2a–2c** are approximately 11% greater than those for **1a–1c** (Table 1 and Figure 4). The estimated force constant (173.9 N m⁻¹) obtained as a second derivative of the energy to the bond length by DFT calculations (M06-2X/ 6-31G*) for **2c** is 1.6 times as large as that for **1c** (108.3 N m⁻¹) (Figure 5).

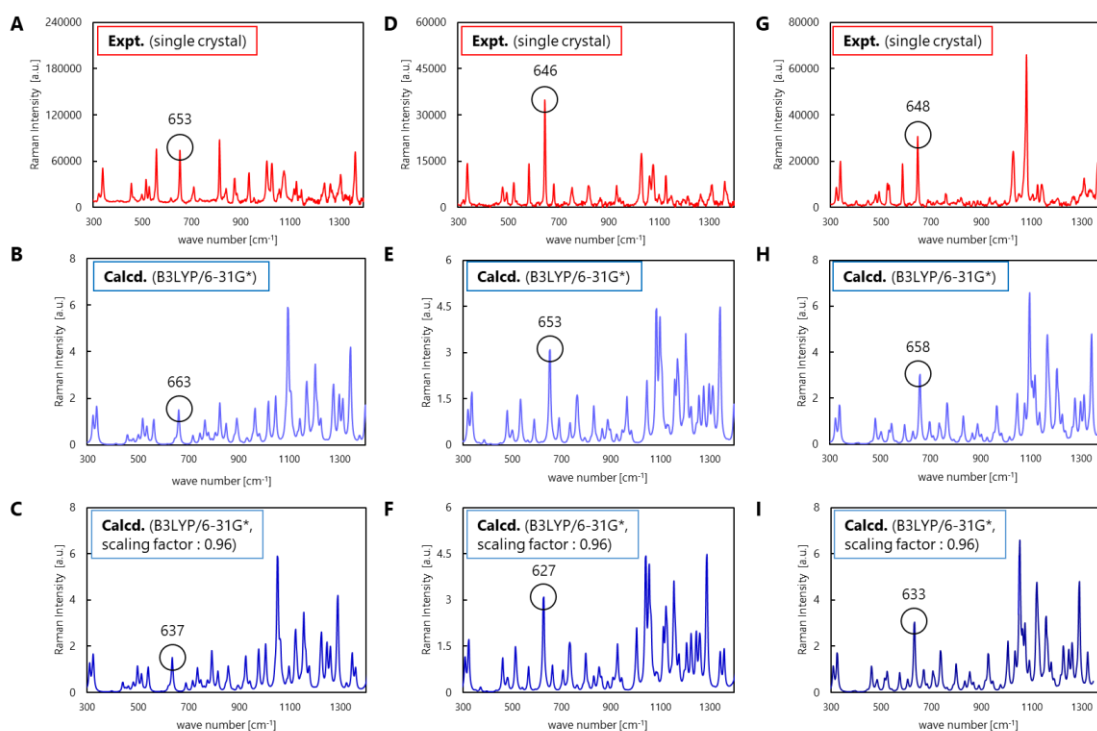


Figure 4. Raman spectra (red) measured by using a single crystal for (A) **1a**, (D) **1b** and (G) **1c** at 298 K. Simulated spectra predicted by DFT calculations at B3LYP/6-31G* level without scaling (light blue) for (B) **1a**, (E) **1b** and (H) **1c**, at B3LYP/6-31G* level under scaling (blue) for (C) **1a**, (F) **1b** and (I) **1c**.

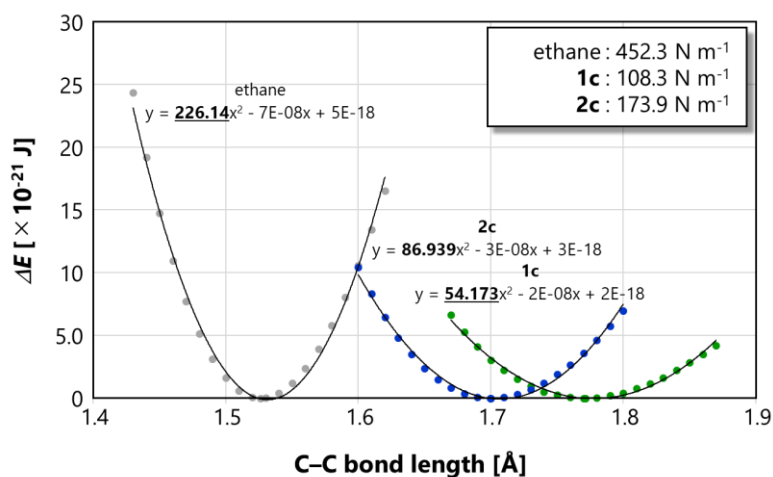


Figure 5. Potential curves for ethane (gray dots) **1c** (green dots) and **2c** (blue dots) calculated by varying the central C–C bond length in steps of 0.01 Å and by considering the most stable conformation (M06-2X/6-31G*).

While thermal isomerization of caged molecules **2a–2c** did not proceed in solution, long-bonded **1a–1c** were quantitatively regenerated by heating of caged molecules **2a–2c** in a solid state (Scheme 4, Figure 6). Although the reason is still unclear, the author supposes that thermal energy by heating was used not for cycloreversion reaction but for some kinds of molecular motion in solution of **2**, and/or caged molecules **2** may be thermodynamically more stable than spiro-DBCHT **1** in the solution state, since the predicted energy levels of **1** and **2** in a gaseous state are very close (*vide infra*).

Scheme 4. Thermal isomerization of **2a–2c** in a solid state.

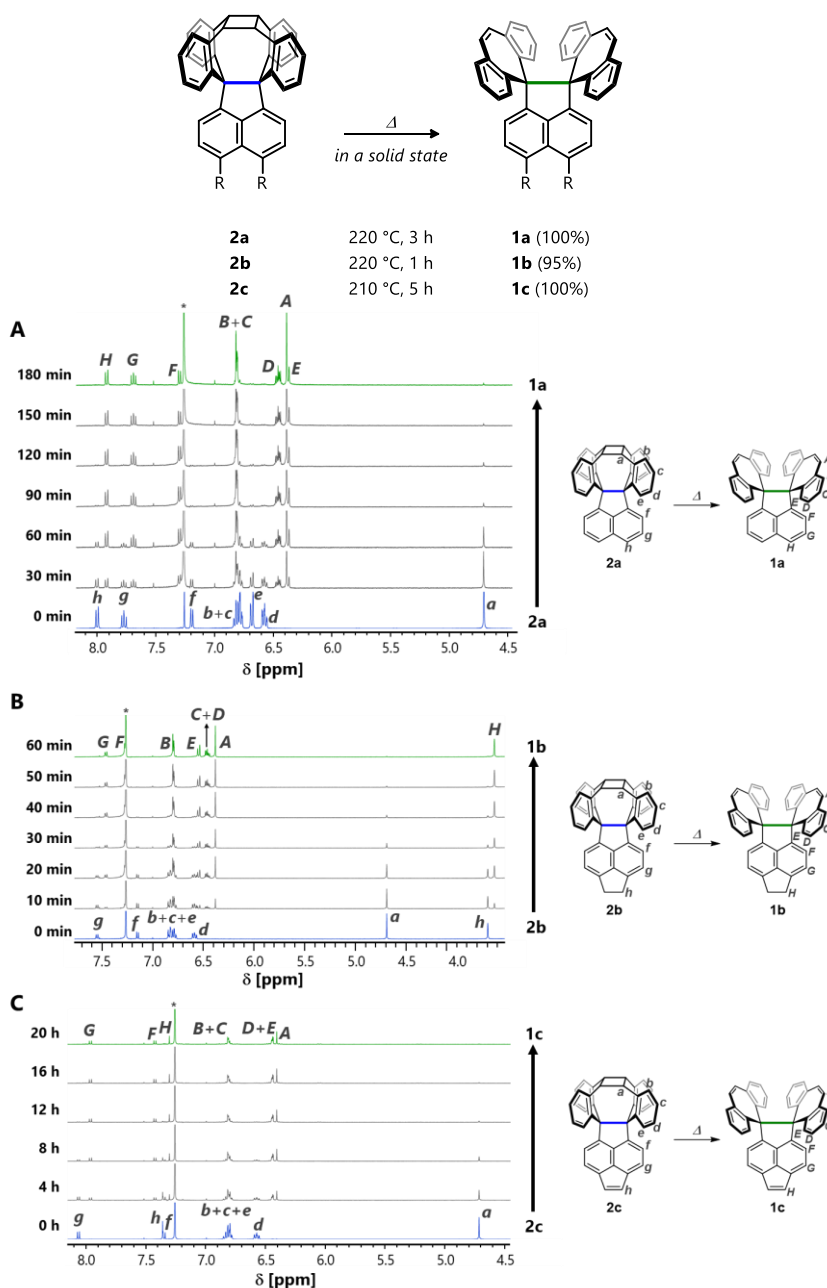


Figure 6. Thermal isomerization was monitored by ^1H NMR spectroscopy in CDCl_3 for (a) **2a**, (b) **2b**, and (c) **2c** upon heating at 493 K, 493 K, and 473 K, respectively, in a solid state. The residual proton signal of the solvent (CHCl_3 , $\delta = 7.26$ ppm) is marked with an asterisk.

3-2-2. Theoretical study

DFT calculations (B3LYP/6-31G*) were performed to obtain the energy level of each molecule (Scheme 5). The predicted energy levels of **1c** and **2c** in a gaseous state is almost the same. Although another reaction pathway (path B) could be considered for the cleavage of the cyclobutene ring, the potential isomer has much higher energy than **1c** and **2c**. Thus, such isomer with eight-membered rings does not a reasonable product of thermal reaction and was not observed by the thermal isomerization reaction of **2c** in both solid state and solution. In addition, NBO and AIM analyses indicated that the bond contraction from spiro-DBCHT **1** to caged molecules **2** induces the slight enhancement of the the values of *s*-character for **2c** are estimated to be 21.05 and 20.83 by using the atomic coordinates of the X-ray crystal structure obtained at 200 K, while those for **1c** are calculated to be 19.16 and 18.64. (Table 2).

Scheme 5. The optimized structures and relative energies of each state related to thermal isomerization of **2c** predicted by DFT calculations (B3LYP/6-31G*).

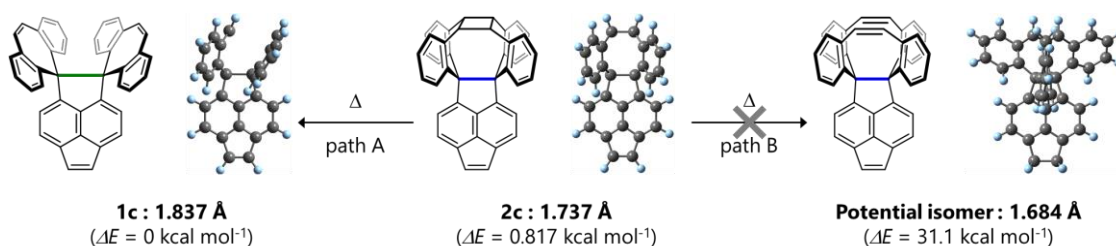


Table 2. (A) NBO and (B) AIM parameters for C1–C2 bond in **1a-1c** and **2a-2c** at the B3LYP-D3/6-311+G**. Atomic coordinates of crystal structures for **1a-1c** and **2a-2c** were used for calculations. Since the single crystals of **2a** was obtained as solvate with hexane molecules, X-ray analysis at 400 K was not performed.

A	200 K			400 K			200 K			400 K			
	1a	1b	1c	1a	1b	1c	2a	2b	2c	2a	2b	2c	
Bond length [Å]	1.742(2)	1.773(3)	1.7980(18)	1.746(3)	1.771(3)	1.806(2)	1.678(6)	1.7133(16)	1.7129(19)		1.722(2)	1.7146(19)	
Occupancy	1.919	1.912	1.910	1.919	1.912	1.908	1.929	1.923	1.923		1.922	1.927	
WBI	0.8604	0.8416	0.8345	0.8594	0.8427	0.8302	0.8858	0.8799	0.8775		0.8761	0.8787	
<i>s</i> character [%]	C1		20.40	19.47	19.16	20.36	19.55	18.83	22.24	21.10	21.05	20.84	20.83
	C2		20.05	19.15	18.64	19.92	19.22	18.43	21.24	21.02	20.83	20.74	21.14
NBO-energy [eV]	<i>bonding</i>		-11.65	-11.16	-11.12	-11.59	-11.65	-11.01	-12.38	-11.88	-12.04	-11.78	-12.04
	<i>anti-bonding</i>		5.551	5.491	4.922	5.852	5.551	4.816	7.129	6.621	6.447	6.453	6.405
B	200 K			400 K			200 K			400 K			
	1a	1b	1c	1a	1b	1c	2a	2b	2c	2a	2b	2c	
Bond length [Å]	1.742(2)	1.773(3)	1.7980(18)	1.746(3)	1.771(3)	1.806(2)	1.678(6)	1.7133(16)	1.7129(19)		1.722(2)	1.7146(19)	
Density of all electrons : ρ_b	0.1629	0.1538	0.1469	0.1616	0.1544	0.1444	0.1833	0.1721	0.1723		0.1691	0.1717	
Energy density : $H(r)$	-0.08810	-0.07893	-0.07234	-0.08682	-0.07958	-0.07013	-0.1109	-0.09803	-0.09823		-0.09484	-0.09761	
Laplacian of electron density : $\nabla^2 \rho$	-0.2105	-0.1825	-0.1625	-0.2066	-0.1845	-0.1555	-0.2805	-0.2424	-0.2425		-0.2324	-0.2407	
Electron localization function (ELF)	0.9392	0.9354	0.9319	0.9387	0.9357	0.9303	0.9453	0.9434	0.9431		0.9423	0.9430	
Localized orbital locator (LOL)	0.7972	0.7920	0.7872	0.7966	0.7923	0.7851	0.8061	0.8033	0.8029		0.8017	0.8027	
Ellipticity of electron density ϵ	0.01822	0.01302	0.01073	0.01751	0.01301	0.01054	0.01649	0.009943	0.009495		0.009828	0.009177	

3-2-3. Single-Crystal-to-Single-Crystal Transformation

By considering the similarity of the crystal packing and lattice parameters of **1b** and **2b**, the author envisaged that both the photocyclization of **1b** and the thermal cycloreversion of **2b** would proceed in a single-crystalline state. When a single crystal of **1b** was photoirradiated at its absorption end ($\lambda > 390$ nm) so that the light can be penetrated into the deep inside of the crystal for 10 h, caged molecule **2b** was generated with maintaining single-crystallinity, and the proportion of **2b** was as high as 45% as determined by a single-crystal X-ray analysis at 200 K by using disorder analysis. This transformation is accompanied by contraction of the central C–C bond from 1.773(3) to 1.738(3) Å (Figure 7A, 7C). After photoirradiation of **1b** for 60 h, valence isomerization to **2b** was completed while maintaining single-crystallinity, where the contracted bond length [1.7118(15) Å] is essentially the same as that [1.7133(16) Å] in the recrystallized sample of **2b**.

In addition, upon heating of a single crystal of **2b** at 493 K for 10 min, thermal cleavage of the cyclobutane ring proceeded in 18% yield, and thermal isomerization proceeded completely after heating for 60 min, which was followed by single-crystal X-ray diffraction at 300 K (Figure 7B, 7C). The reason for the difference temperature of X-ray analyses is related to the fact that **1b** undergoes a phase transition of the crystal at lower temperature. As a result of the ring opening of cyclobutane, the central C–C bond was certainly expanded to the original value [1.777(3) Å], which is in good agreement with that [1.772(3) Å] in the recrystallized sample of **1b**, thanks to the outstanding stability of the long-bonded compound **1b** at high temperature. These results show that reversible SCSC transformation occurred between **1b** and **2b**, accompanied by unprecedented expansion and contraction of the elongated C–C bond. Although single-crystallinity was not maintained for the pairs **1a/2a** and **1c/2c**, quantitative [2+2] photocyclization and thermal cleavage of the cyclobutane ring were also achieved in the solid state.

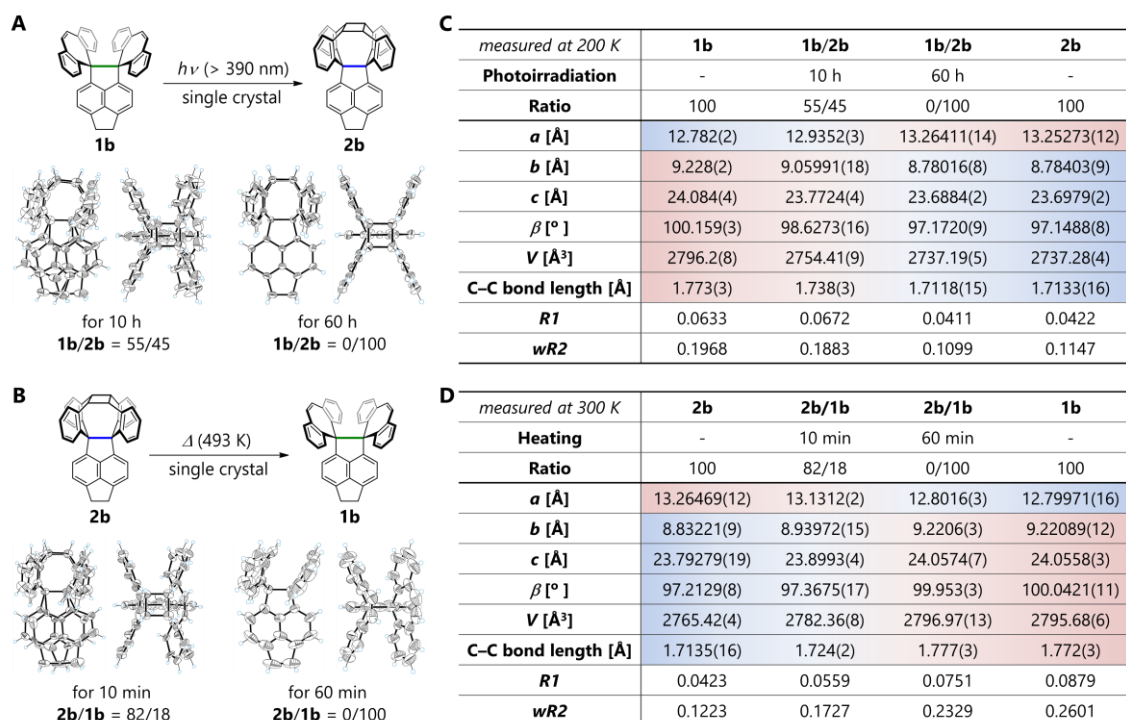


Figure 7. (A) Upon photoirradiation of a single crystal of **1b** with $\lambda > 390$ nm for 10 and 60 h, the SCSC photocycloaddition reaction proceeded in respective yields of 45 and 100%, which were determined by single-crystal X-ray analysis at 200 K. (B) When a single crystal of **2b** was heated at 493 K for 10 and 60 min, SCSC thermal cycloreversion proceeded in respective yields of 18% and 100%, which were determined by single-crystal X-ray analysis at 300 K. Thermal ellipsoids are shown at the 30% probability level for intermediates and the 50% probability level for completely converted samples. (C,D) The crystallographic data for **1b** and **2b** are summarized in the table.

3-2-4. Redox Behavior

To date, dynamic redox (*dyrex*) systems have been studied based on HPE skeleton,^[36,37] in which neutral electron donors and corresponding dications can be interconvertible upon two-electron transfer. During their interconversion, they show a reversible structural change such as C–C bond formation/cleavage, accompanied by a drastic color change (electrochromism). As a result of a dynamic change in structures, the oxidation potential of the neutral states and the reduction potential of the oxidation states are largely separated, so that they exhibit high electrochemical bistability. Based on such electrochemical behaviors, *dyrex* systems are very useful from the viewpoint of making molecular devices controlled by electric potential.

As presumed by an *s-cis*-type 1,2-diphenylethane model, the σ^+ -orbital of the central C–C bond can interact with the π^+ -orbital on two units of π -electron systems (through-bond interaction; TBI), which could make new orbitals (*i.e.*, $\sigma^+\pi^+$ and $\sigma^-\pi^+$, Figure 8). As a result, the energy level of $\sigma^-\pi^+$ orbital can be higher than that of π^- orbital (original HOMO). By considering that the overlapping between Csp^3 orbitals should be depleted, an expansion of the central C–C single bond would raise the σ^+ level. The closeness of σ^+ and π^+ level could cause a greater energy splitting between $\sigma^+\pi^+$ and $\sigma^-\pi^+$ orbitals, which results in raising the HOMO level. Therefore, TBI in HPEs plays an important role to modify the MO level that determines their electron-donating properties.

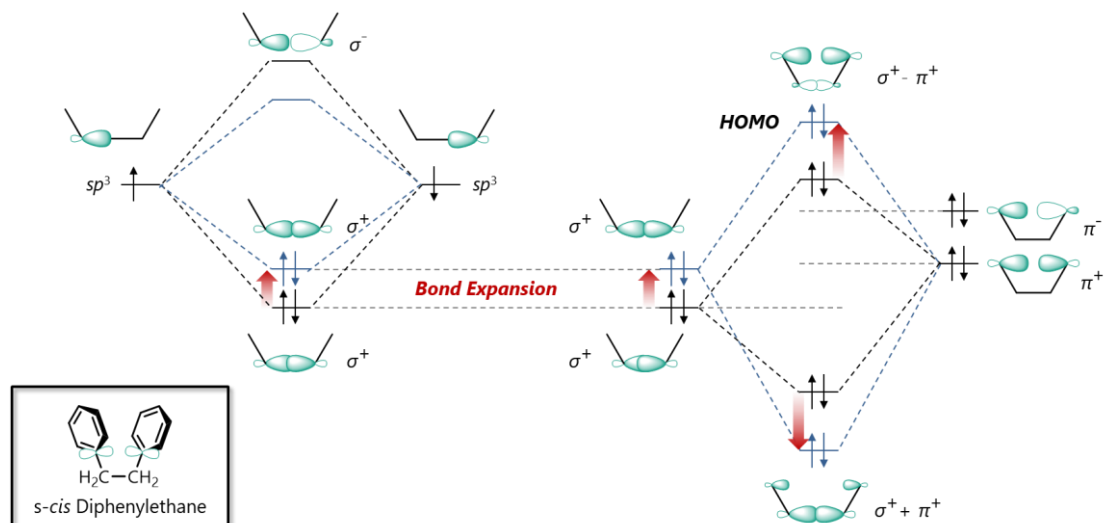


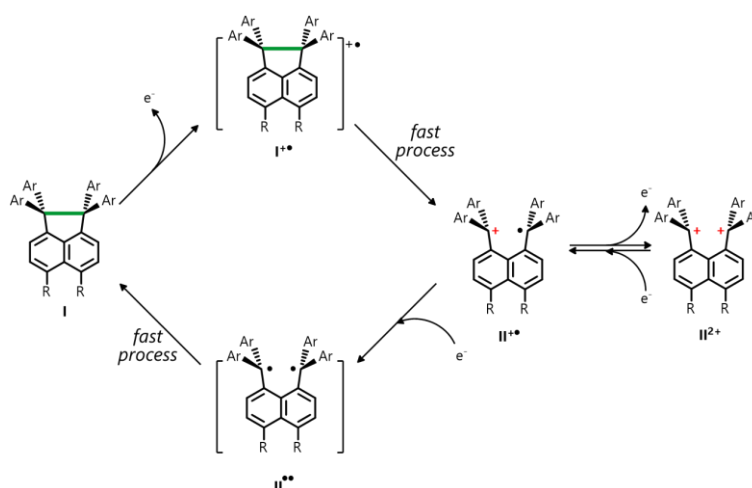
Figure 8. Bond expansion raises the HOMO level via TBI in the diphenylethane model.

HPE-type compound **I**,^[38–41] some of which have been shown to have a longer C–C bond (>1.60 Å) than the standard (1.54 Å), is representative members of *dyrex* systems. As shown in Scheme 6, upon two-electron oxidation of HPE derivatives **I**, C–C bond cleavage occurs to generate bond dissociated dications **II**²⁺, which undergo two-electron reduction to regenerate HPEs **I**. In the voltammograms, both one-wave two-electron oxidation and reduction peaks were observed without any other peaks,

whose mechanism was previously proposed.^[39,42]

In the oxidation processes of σ -bonded donors **I**, cation radicals **I**^{•+} generated by one-electron oxidation would immediately convert to more stable cation radicals **II**^{•+} because of rapid bond cleavage. Since the oxidation potential of cation radicals **II**^{•+} is much less positive than that of σ -bonded species **I**, cation radicals **II**^{•+} preferentially undergo oxidation, and thus the steady-state concentration of both cation radicals **I**^{•+} and **II**^{•+} would be negligible in the oxidation process. On the other hand, a stepwise reduction process could be observed because reduction potentials of two cationic sites in **II**²⁺ would be marginally separated due to an electronic interaction of the two triarylmethylium units. However, the steady-state concentration of both cation radicals **II**^{•+} and diradicals **II**^{••} would also be negligible because of disproportionation of **II**^{•+} into **II**^{••}/**II**²⁺ as well as fast bond formation in **II**^{••}. Therefore, one-wave two-electron redox waves could be apparently observed.

Scheme 6. Redox mechanism in *dyrex* systems.



Based on such background, the author has investigated redox behavior of **1a-1c** and **2a-2c** with a much longer C–C bond. The redox potentials of spiro-DBCHT **1a-1c** and caged molecules **2a-2c** were measured by cyclic voltammetry in CH₂Cl₂ at ambient temperature (Figure 9A). While two electron oxidation occurs at lower potentials for the former with an expanded bond (E^{ox}/V vs. SCE: +0.93 for **1a**, +0.65 for **1b**, and +0.57 and +0.69 for **1c**), one-wave two-electron oxidation peaks appeared at much higher potentials for the latter with a contracted bond (E^{ox}/V : +1.59 for **2a**, +1.36 for **2b**, and +1.66 for **2c**) (Figure 9A, 9D). Especially in **1c/2c**, the author found the largest difference in potential of about 1.1 eV before and after photocyclization. This change can be explained as follows: (i) the through-bond interaction that causes an increasing in the HOMO level would be maximized by expansion of the C–C single bond (Figure 10)^[41,43] and (ii) the coefficients in HOMO are located on the DBCHT unit and the elongated σ -bond in **1**, whereas the coefficients are located on the acenaphthene, pyracene, or dihydropyracylene skeleton in **2** based on DFT calculations (Figures 2).

On the other hand, two-electron reduction peaks were found in the far cathodic region due to cleavage of the elongated C–C bond to give 3^{2+} or 4 (*dyrex* behavior). It should be noted that reduction peaks in the voltammograms of **1** and **2** appear at almost the same potentials, indicating that the two-electron oxidation of caged molecules **2** could induce not only scission of the central C–C bond but also cleavage of cyclobutane ring.

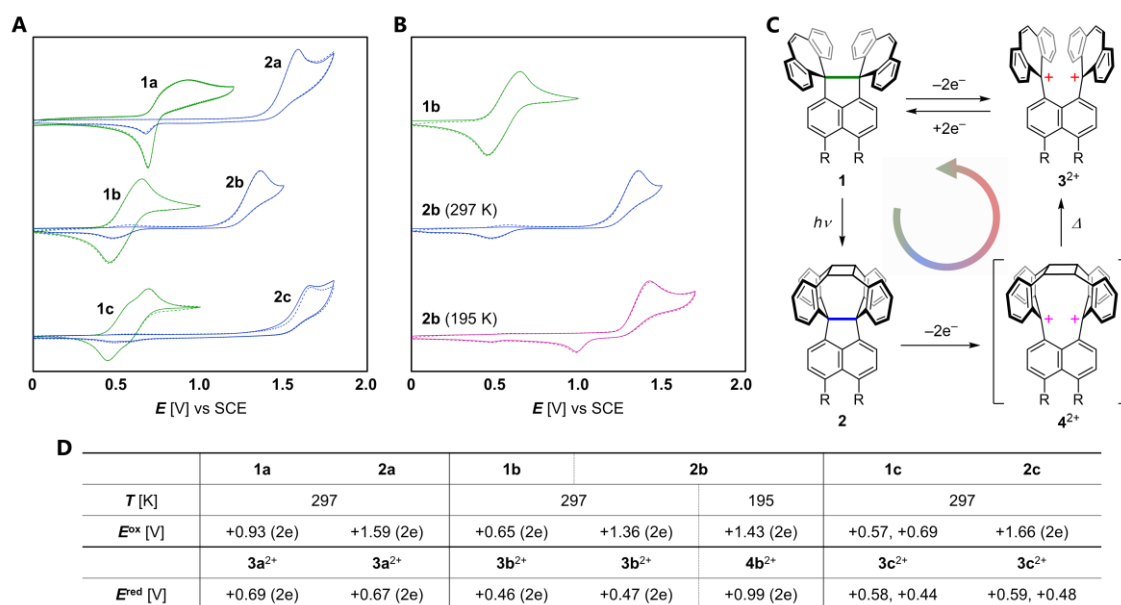


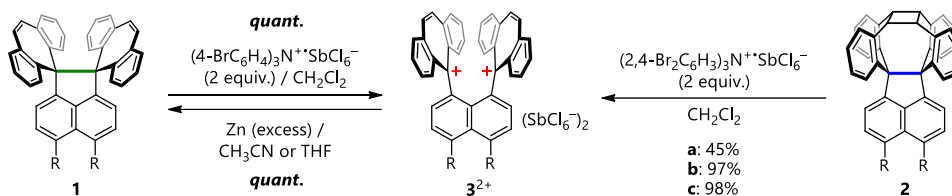
Figure 9. Cyclic voltammograms of (A) **1** and **2** at 297 K and (B) **1b**, **2b** (at 297 K), and **2b** (at 195 K) in CH_2Cl_2 containing 0.1 M Bu_4NBF_4 as a supporting electrolyte (scan rate 0.1 V s^{-1} , Pt electrode). The second cycles are shown by a dotted line. (C) Mechanism of redox interconversion. (D) Redox potentials are summarized, and peak potentials are shown as E^{ox} and E^{red} . (a: $\text{R}=\text{H}$; b: $\text{R},\text{R}=\text{CH}_2\text{-CH}_2$; c: $\text{R},\text{R}=\text{CH}=\text{CH}$)

To gain further insight into the mechanism of three-bond scission in the oxidation of **2**, the author conducted cyclic voltammetry at 195 K in CH_2Cl_2 using **2b**. As shown in Figure 9B-9D, another reduction peak appeared at a less cathodic region (E^{red}/V : +0.99), which is far different from that in the reduction of $3b^{2+}$ (E^{red}/V : +0.46), and thus caged dication $4b^{2+}$ was generated by the oxidation of **2b** through scission of the central C–C bond at low temperature, whereas thermal cleavage of the cyclobutane ring of $4b^{2+}$ produces bond-dissociated dication $3b^{2+}$ at room temperature.

Based on the voltammetric analysis, deeply colored dications $3a^{2+}$ - $3c^{2+}$ were successfully isolated as stable $(\text{SbCl}_6^-)_2$ salts by treatment of spiro-DBCHT **1a-1c** with two equivalents of $(4\text{-BrC}_6\text{H}_4)_3\text{N}^+\text{SbCl}_6^-$ in CH_2Cl_2 , due to stabilization of the dibenzotropylium units (Scheme 6, Figure 10). Although formation of the same dication from caged molecules **2** was demonstrated by the electrochemical oxidation of **1b/2b** and **1c/2c** (Figure 11), **2a-2c** with lower HOMO levels need a stronger oxidant $(2,4\text{-Br}_2\text{C}_6\text{H}_3)_3\text{N}^+\text{SbCl}_6^-$ in CH_2Cl_2 to give the same dications $3a^{2+}$ - $3c^{2+}$ (Scheme 7). Thus, completely selective oxidation of **1b** in a 1:1 mixture of **1b** and **2b** was achieved by using (4-

$\text{BrC}_6\text{H}_4)_3\text{N}^+\text{SbCl}_6^-$ (Scheme 8). This means that spiro-DBCHT **1** can be protected against oxidation by photoconversion into caged molecules **2** with a lower HOMO level.

Scheme 7. Chemical oxidation of **1a-1c** and **2a-2c** and reduction of **3a²⁺-3c²⁺**.



Scheme 8. Selective oxidation of the mixture of **1b:2b** (1:1).

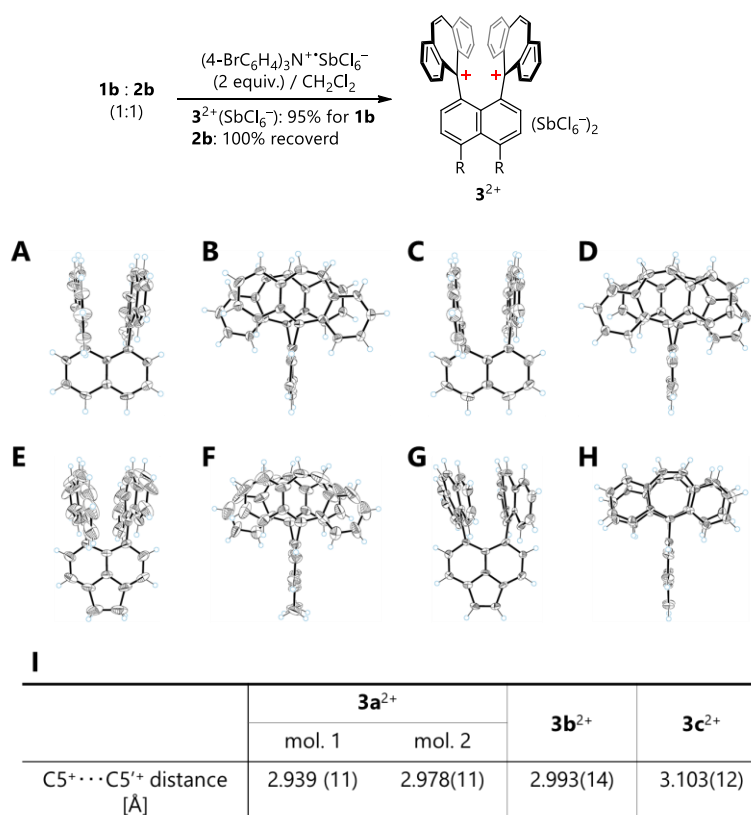


Figure 10. ORTEP drawings of (A) mol. 1 and (B) mol. 2 of **2a²⁺(SbCl₆)₂**, (C) **2b²⁺(SbCl₆)₂** and (D) **2c²⁺(SbCl₆)₂**. There are two crystallographically independent molecules (mol. 1 and mol. 2) in **2a²⁺(SbCl₆)₂**. Solvent molecules and counterions are omitted for clarity. Thermal ellipsoids are shown at the 50% probability level. (I) The distance between cationic centers (C5⁺...C5⁺ atoms) on the X-ray structure for **2a²⁺-2c²⁺**.

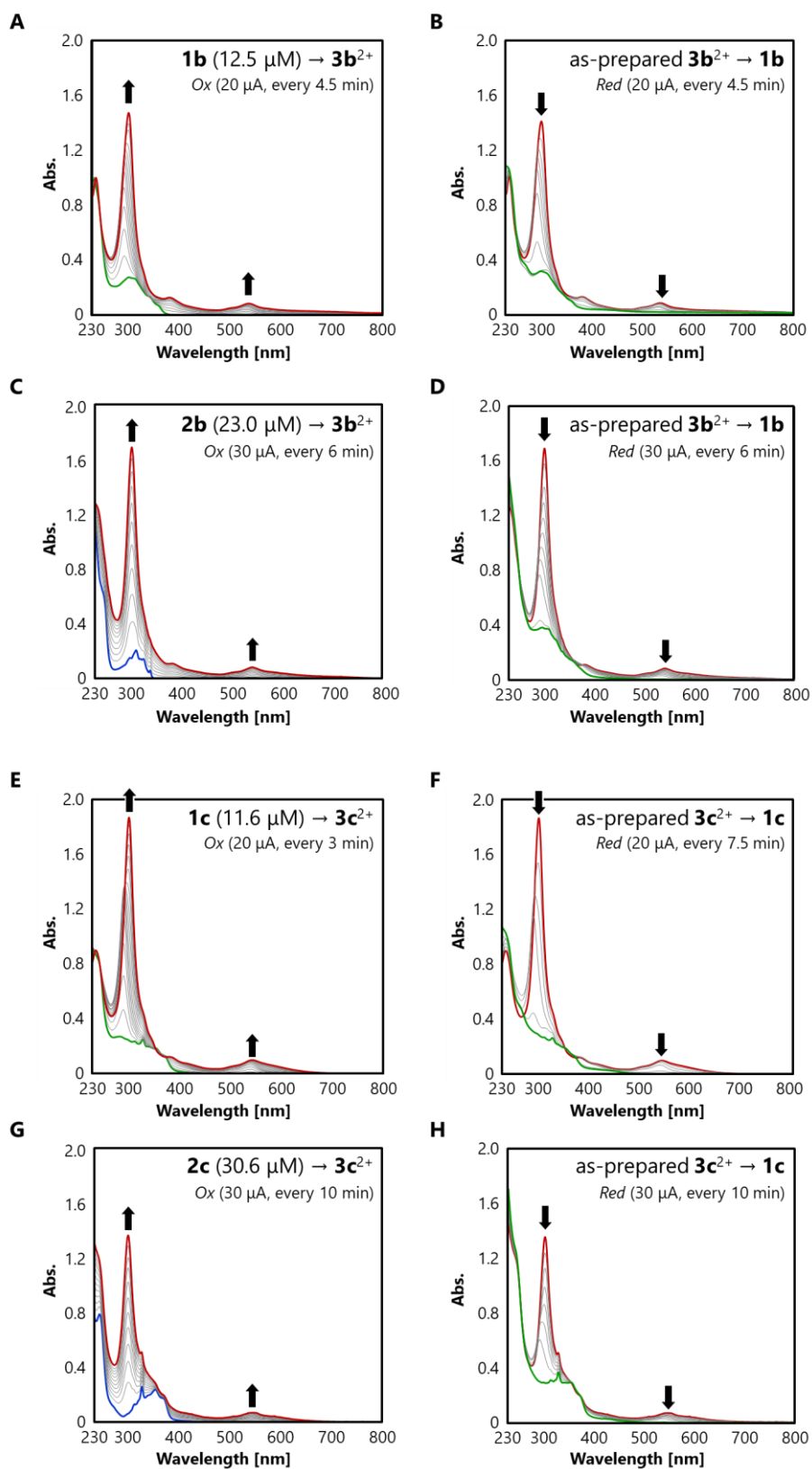


Figure 11. Changes in the UV/Vis spectra of **1b/2b** and **1c/2c** upon constant-current electrochemical oxidation and as-prepared $3b^{2+}$ and $3c^{2+}$ upon constant-current electrochemical reduction in CH_2Cl_2 containing 0.05 M Bu_4NBF_4 as a supporting electrolyte.

The author then considered that both spiro-DBCHT **1** and caged molecules **2** could react with an oxidant to produce dication $\mathbf{3}^{2+}$ in a solid state. When **1b** was subjected to grinding with two equivalents of blue-colored $(4\text{-BrC}_6\text{H}_4)_3\text{N}^+\text{SbCl}_6^-$, the color changed to deep purple with the formation of dicationic dye $\mathbf{3b}^{2+}$, which was confirmed by the appearance of characteristic IR absorptions assigned to $\mathbf{3b}^{2+}(\text{SbCl}_6^-)_2$ (e.g. 1601 and 1385 cm^{-1}) and the resulting amine (e.g. 1486 and 1311 cm^{-1}) (Figure 12A, 12D). Moreover, grinding of **2b** with two equivalents of green-colored $(2,4\text{-Br}_2\text{C}_6\text{H}_3)_3\text{N}^+\text{SbCl}_6^-$ smoothly led to the formation of a deep purple powder of dication salt $\mathbf{3b}^{2+}(\text{SbCl}_6^-)_2$, where three-bond scission proceeded in a solid state (Figure 12B, 12E). Additionally, upon grinding of $\mathbf{3b}^{2+}(\text{SbCl}_6^-)_2$ with an excess amount of Zn powder, $\mathbf{3b}^{2+}$ underwent two-electron reduction to give long bonded **1b** (Figure 12C, 12F). This is the first example of flexible C–C bond exhibiting the reversible expansion, contraction, formation, and scission of a $\text{Csp}^3\text{--Csp}^3$ single bond in a simple organic compound, especially in a pure hydrocarbon.

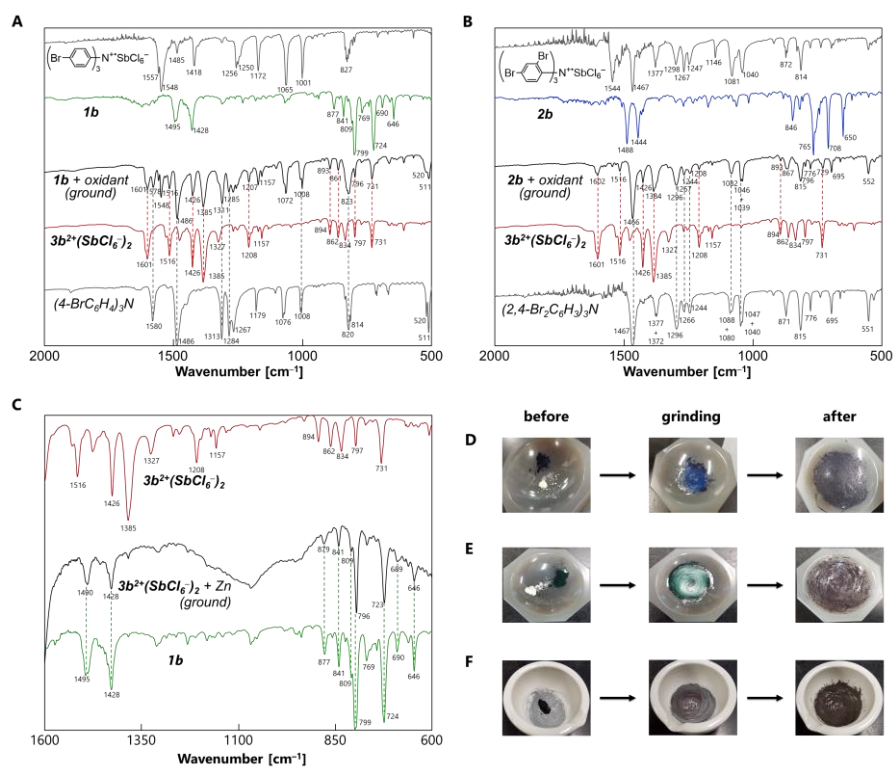
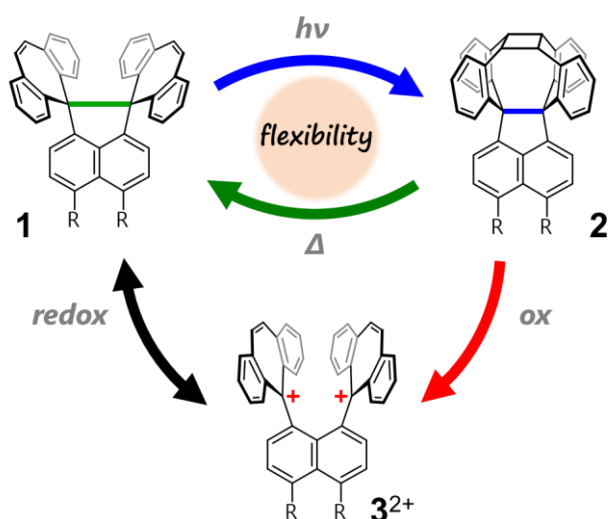


Figure 12. (A) Solid-state oxidation of **1b** with two equivalents of $(4\text{-BrC}_6\text{H}_4)_3\text{N}^+\text{SbCl}_6^-$ was confirmed by IR spectroscopy. (B) Solid-state oxidation of **2b** with two equivalents of $(2,4\text{-Br}_2\text{C}_6\text{H}_3)_3\text{N}^+\text{SbCl}_6^-$ as a stronger oxidant was confirmed by IR spectroscopy. (C) Solid-state reduction of $\mathbf{3b}^{2+}(\text{SbCl}_6^-)_2$ with an excess amount of Zn powder was confirmed by IR spectroscopy. Photographs showing mechano-oxidation of (D) **1b** with $(4\text{-BrC}_6\text{H}_4)_3\text{N}^+\text{SbCl}_6^-$ and (E) **2b** with $(2,4\text{-Br}_2\text{C}_6\text{H}_3)_3\text{N}^+\text{SbCl}_6^-$, and (F) mechano-reduction of $\mathbf{3b}^{2+}(\text{SbCl}_6^-)_2$ with an excess amount of Zn powder.

3-3. Conclusion

The author has demonstrated that photo- and thermal isomerization between spiro-DBCHT **1** and caged molecules **2** proceeded quantitatively in a solid state, where the reversible formation and scission of two C–C bonds were accompanied by expansion and contraction of the central C–C bond. Since formation of the cyclobutane ring and contraction of the C–C bond induce lowering of the HOMO level through an efficient TBI, oxidative properties can be deactivated/activated by light/heat. Caged molecules **2** generated by the photoirradiation of spiro-DBCHT **1** undergo two-electron oxidation to transiently produce bond-dissociated dication 4^{2+} followed by thermal cleavage of the cyclobutane ring to give stable dication 3^{2+} . An elongated C–C bond was reformed by two-electron reduction of dication 3^{2+} , resulting in the formation of original spiro-DBCHT **1**. Notably, all of these processes can proceed in a solid state. This study in this chapter provides a new perspective on C–C bonds that exhibit reversible expansion, contraction, formation, and scission. Thus, hydrocarbons that contain a “flexible” C–C bond could be promising candidates for the development of functional materials, whose crystals, films, or polymers can respond to the external stimuli such as light and heat with anisotropic expansion and contraction of the matter as well as reversible switching of oxidative properties.

Scheme 9. Graphical summary of this chapter.



3-4. Experimental Section

General Procedures

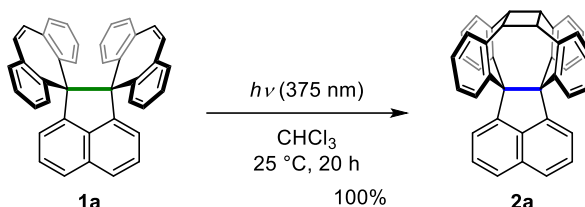
All reactions were carried out under an argon atmosphere. All commercially available compounds were used without further purification unless otherwise indicated. Dry CH₃CN was obtained by distillation from CaH₂ prior to use. Column chromatography was performed on silica gel 60N (KANTO KAGAKU, spherical neutral) of particle size 40–50 μm or Wakogel[®] 60N (neutral) of particle size 38–100 μm. ¹H and ¹³C NMR spectra were recorded on a BRUKER Ascend[™] 400 (¹H/400 MHz and ¹³C/100 MHz) spectrometer. IR spectra were measured as a KBr pellet on a JEOL JIR-WINSPEC100 FT/IR spectrophotometer. Mass spectra were recorded on a JMS-T100GCV spectrometer in FD mode by Dr. Eri Fukushi and Mr. Yusuke Takata (GC-MS & NMR Laboratory, Research Faculty of Agriculture, Hokkaido University). Melting points were measured on a Yamato MP-21 and are uncorrected. UV/Vis spectra were recorded on a Hitachi U-3500 spectrophotometer. Fluorescence spectra were measured on a Hitachi F-7000 spectrofluorometer. Fluorescence quantum yields were determined by using 9,10-diphenylanthracene ($\Phi_F = 0.97$) as an external standard.^[44] For photoisomerization reaction, the Hitachi F-7000 spectrofluorometer was used for UV/Vis and NMR monitoring, and a Contec black light PW-UV943H-04 [375 nm light-emitting diode (LED)] and an Ushiospax SX-UID501XAMQ light source device with a CORNING COLOR FILTER (No. 3-73) were used on a preparative scale and on a single crystal, respectively. The analysis of Raman spectroscopy was carried out with inVia Reflex at the OPEN FACILITY, Hokkaido University Sousei Hall. Redox potentials (E^{ox} and E^{red}) were measured by cyclic voltammetry in dry CH₂Cl₂ containing 0.1 M Bu₄NBF₄ as a supporting electrolyte. All of the values shown in the text are in E/V vs. SCE measured at the scan rate of 0.1 V·s⁻¹. Pt electrodes were used as the working (disk) and counter electrodes. The working electrode was polished using a water suspension of aluminum oxide (0.05 μm) before use. DFT calculations were performed with the Gaussian 16W program package.^[45] Version 3.8 of the Multiwfn software^[46] was used for topological analysis of the electron density that is obtained by DFT calculations. The NBO analyses were performed with the Version 7.0 of the NBO^[47] which was implemented in the Gaussian 16W program. The atomic coordinates were obtained from crystal structures of **1a-1c** and **2a-2c** at each temperature and the wave function was calculated at B3LYP-D3/6-311+G** for AIM and NBO analyses.

Preparation

- Preparation of caged molecules **2a-2c**

Caged molecule **2a**

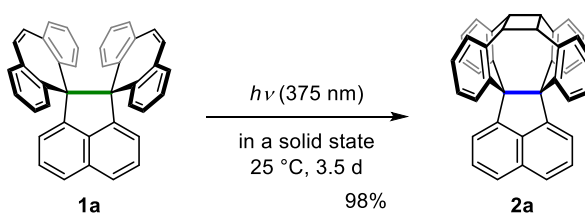
Photoisomerization of **1a** in solution:



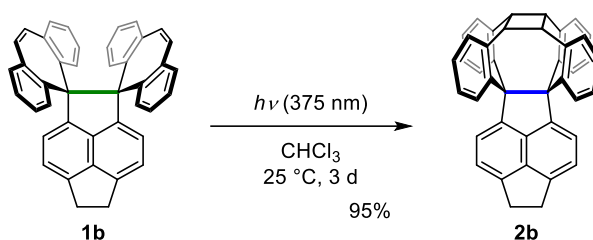
A solution of **1a** (246 mg, 485 μmol) in CHCl₃ (100 mL) was photoirradiated with a 375 nm LED at 25 °C for 20 h, and then the solution was evaporated under reduced pressure. The residue was dissolved in CH₂Cl₂, and the resulting solution was filtered through a silica gel pad. The filtrate was concentrated under reduced pressure and dried *in vacuo* to give **2a** (245 mg) as a white solid in 100% yield.

mp: same as **1a** [245-249 °C (decomp.)]^[16] because of thermal isomerization from **2a** to **1a**; ¹H NMR (CDCl₃): δ 8.00 (d, $J = 8.1$ Hz, 2H), 7.78 (dd, $J = 7.1$ Hz, 8.1 Hz, 2H), 7.19 (d, $J = 7.1$ Hz, 2H), 6.84-6.76 (m, 8H), 6.68 (dd, $J = 0.9$ Hz, 8.2 Hz, 4H), 6.57 (ddd, $J = 2.0$ Hz, 6.9 Hz, 8.2 Hz, 4H), 4.71 (s, 4H); ¹³C NMR (CD₂Cl₂): δ 148.79, 143.72, 139.51, 137.10, 132.28, 131.69, 131.56, 127.90, 127.73, 127.06, 125.35, 123.65, 76.61, 47.76; IR (KBr): 3054, 3023, 2941, 1487, 1444, 1364, 1298, 1268, 1175, 1066, 1016, 817, 792, 764, 742, 711, 650, 590 cm⁻¹; LRMS (FD): m/z (%) 508.25 (10), 507.25 (45), 506.25 (M⁺, bp); HRMS (FD) m/z : [M]⁺ calcd. for C₄₀H₂₈, 506.20345; found, 506.20320; UV/Vis (CH₂Cl₂): $\lambda_{\text{max}}/\text{nm}$ ($\epsilon/\text{L mol}^{-1} \text{ cm}^{-1}$) 291 (5900), 303 (7400), 312 (5150), 317 (4500), 330 (800); UV/Vis (CHCl₃): 291 (5930), 303 (7550), 312 (5450), 317 (4880), 331 (1080); Fluorescence (CHCl₃, $\lambda_{\text{ex}} = 300$ nm): $\lambda_{\text{em}}/\text{nm}$ (Φ_{F}) 340, 350 (0.11).

Photoisomerization of **1a** in a solid state:

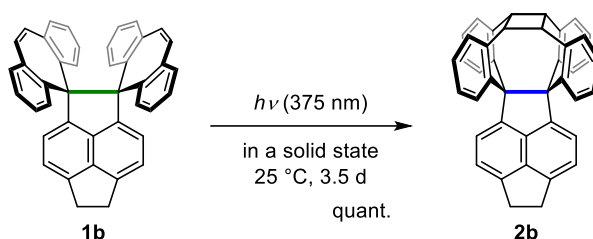


A solid of **1a** (4.0 mg, 7.90 μmol) was photoirradiated with a 375 nm LED at 25 °C for 3.5 d to give **2a** (3.9 mg) as a white solid in 98% yield.

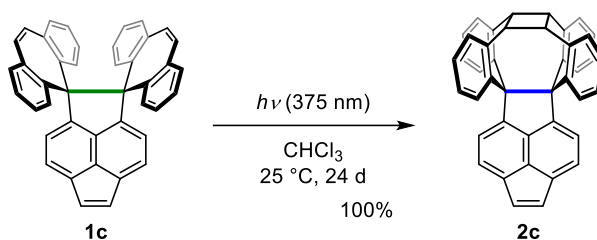
Caged molecule 2bPhotoisomerization of **1b** in solution:

A solution of **1b** (52.8 mg, 99.1 μmol) in CHCl₃ (15 mL) was photoirradiated with a 375 nm LED at 25 °C for 3 d, and then the solution was evaporated under reduced pressure. The residue was dissolved in CH₂Cl₂, and the resulting solution was filtered through a silica gel pad. The filtrate was concentrated under reduced pressure and dried *in vacuo* to give **2b** (50.2 mg) as a white solid in 95% yield.

mp: same as **1b** [250-260 °C (decomp.)]^[16] because of thermal isomerization from **2b** to **1b**; ¹H NMR (CDCl₃): δ 7.55 (d, $J = 7.0$ Hz, 2H), 7.15 (d, $J = 7.0$ Hz, 2H), 6.84-6.76 (m, 12H), 6.58 (ddd, $J = 2.0$ Hz, 7.1 Hz, 8.5 Hz, 4H), 4.71 (s, 4H), 3.70 (s, 4H); ¹³C NMR (CDCl₃): δ 143.49, 143.35, 143.39, 139.30, 139.18, 135.73, 131.67, 131.59, 128.86, 127.14, 125.54, 120.55, 80.30, 47.85, 31.98; IR (KBr): 3052, 3015, 2934, 1488, 1444, 1299, 1268, 1230, 1173, 1063, 1016, 943, 881, 846, 818, 806, 765, 733, 708, 650, 643, 616, 551 cm⁻¹; LRMS (FD): m/z (%) 534.27 (12), 533.27 (50), 532.26 (M⁺, bp); HRMS (FD) m/z : [M]⁺ calcd. for C₄₂H₂₈, 532.21910; found, 532.21988; UV/Vis (CH₂Cl₂): λ_{max}/nm ($\epsilon/L \text{ mol}^{-1} \text{ cm}^{-1}$) 298 (6870), 310 (9400), 318 (6430), 325 (6400), 338 (2370); UV/Vis (CHCl₃): 298 (6950), 310 (9550), 318 (6730), 325 (6800), 338 (2780); Fluorescence (CHCl₃, $\lambda_{\text{ex}} = 300$ nm): λ_{em}/nm (Φ_{F}) 347, 354 (0.01).

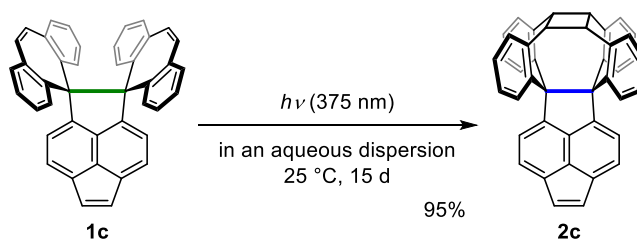
Photoisomerization of **1b** in a solid state:

A solid of **1b** (9.7 mg, 18.2 μmol) was photoirradiated with a 375 nm LED at 25 °C for 3.5 d to give **2b** (9.8 mg) as a white solid in quantitative yield.

Caged molecule 2cPhotoisomerization of 1c in solution:

A solution of **1c** (155 mg, 292 μmol) in CHCl₃ (100 mL) was photoirradiated with a 375 nm LED at 25 °C for 24 d, and then the solution was evaporated under reduced pressure. The residue was purified by silica gel column chromatography (hexane/CH₂Cl₂ = 5) to give **2c** (155 mg) as a pale yellow solid in 100% yield.

mp: same as **1c** [250-258 °C (decomp.)]^[16] because of thermal isomerization from **2c** to **1c**; ¹H NMR (CDCl₃): δ 8.07 (d, J = 7.1 Hz, 2H), 7.36 (s, 2H), 7.35 (d, J = 7.1 Hz, 2H), 6.85-6.78 (m, 12H), 6.57 (ddd, J = 2.0 Hz, 6.9 Hz, 8.5 Hz, 4H), 4.71 (s, 4H); ¹³C NMR (CDCl₃): δ 150.57, 142.65, 139.30, 136.27, 132.60, 131.78, 131.36, 129.25, 128.83, 127.38, 127.21, 126.36, 125.64, 81.27, 47.76; IR (KBr): 3053, 3024, 2939, 1625, 1596, 1488, 1468, 1443, 1417, 1364, 1173, 1081, 955, 846, 765, 726, 707, 671, 650, 615 cm⁻¹; LRMS (FD) m/z (%): 532.25 (13), 531.25 (46), 530.25 (M⁺, bp); HRMS (FD) m/z : [M]⁺ calcd. for C₄₂H₂₆, 530.20345; found, 530.20410; UV/Vis (CH₂Cl₂): $\lambda_{\text{max}}/\text{nm}$ ($\epsilon/\text{L mol}^{-1} \text{cm}^{-1}$) 314 (3800), 329 (8250), 340 (6200), 355 (7850), 370 (5780); UV/Vis (CHCl₃): 314 (4120), 329 (8440), 340 (6380), 356 (8060), 372 (6060); Fluorescence (CHCl₃, λ_{ex} = 300 nm): $\lambda_{\text{em}}/\text{nm}$ (Φ_{F}) 347, 364, 385 (0.004).

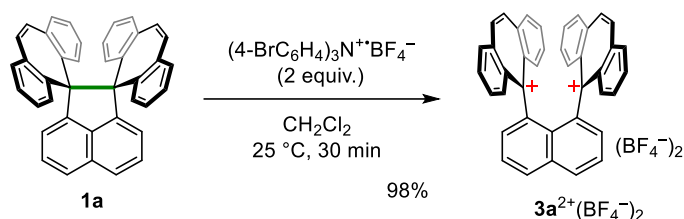
Photoisomerization of 1c in a solid state:

An aqueous dispersion of **1c** (8.5 mg, 16.0 μmol) in water (6 mL) was photoirradiated with a 375 nm LED at 25 °C for 15 d, and then filtered to give **2c** (8.4 mg) as a pale yellow solid in 95% yield (NMR).

- Preparation of dication $3a^{2+}$ - $3c^{2+}$

Dicationic salt $3a^{2+}(\text{BF}_4^-)_2$

Oxidation of **1a** in solution:

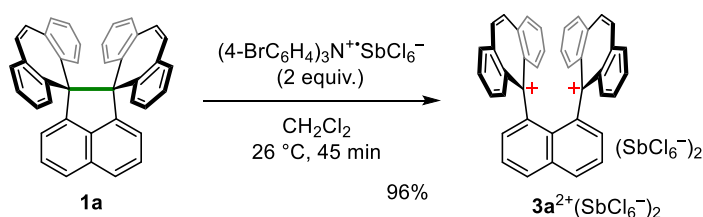


To a solution of **1a** (40.5 mg, 79.9 μmol) in dry CH_2Cl_2 (5 mL) was added tris(4-bromophenyl)aminium tetrafluoroborate (90.9 mg, 160 μmol) at 25 $^\circ\text{C}$ to generate a deep purple solution, and the mixture was stirred at 25 $^\circ\text{C}$ for 30 min. The addition of dry Et_2O led to precipitation of the dication salt. The precipitates were collected, washed with dry Et_2O three times, and dried *in vacuo* to give $3a^{2+}(\text{BF}_4^-)_2$ (53.2 mg) as a deep purple powder in 98% yield.

mp: 213-216 $^\circ\text{C}$ (decomp.); ^1H NMR (CD_3CN): δ 8.75 (dd, $J = 1.2, 8.4$ Hz, 2H), 8.70 (s, 4H), 8.38 (dd, $J = 1.4, 8.1$ Hz, 4H), 8.24 (ddd, $J = 1.1, 6.9, 8.1$ Hz, 4H), 8.03 (dd, $J = 7.1, 8.4$ Hz, 2H), 7.83 (d, $J = 1.1, 8.3$ Hz, 4H), 7.53 (ddd, $J = 1.4, 6.9, 8.3$ Hz, 4H), 7.47 (dd, $J = 1.2, 7.1$ Hz, 2H); ^{13}C NMR (CD_3CN): δ 179.44, 146.01, 145.29, 141.32, 138.78, 138.72, 136.83, 136.60, 135.83, 134.86, 132.87, 132.40, 130.61, 126.79; IR (KBr): 3059, 2360, 1603, 1519, 1478, 1427, 1385, 1331, 1197, 1055, 899, 855, 799, 733 cm^{-1} ; LRMS (FD) m/z (%): 508.17 (11), 507.17 (45), 506.17 (M^+ , bp); HRMS (FD) m/z : $[\text{M}]^+$ calcd. for $\text{C}_{40}\text{H}_{26}$, 506.20345; found, 506.20484; UV/Vis (CH_2Cl_2): $\lambda_{\text{max}}/\text{nm}$ ($\epsilon/\text{L mol}^{-1} \text{cm}^{-1}$) 302 (78300), 382 (5730), 540 (3400).

Dicationic salt $3a^{2+}(\text{SbCl}_6^-)_2$

Oxidation of **1a** in solution:

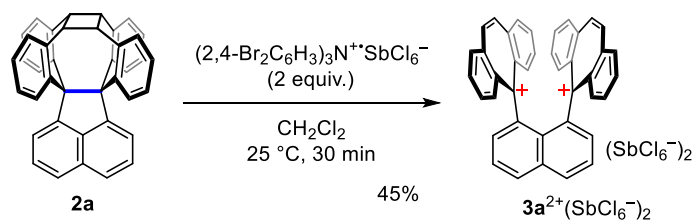


To a solution of **1a** (20.0 mg, 39.4 μmol) in dry CH_2Cl_2 (2 mL) was added tris(4-bromophenyl)aminium hexachloroantimonate (64.0 mg, 78.3 μmol) at 0 $^\circ\text{C}$ to generate a deep purple solution, and the mixture was stirred at 26 $^\circ\text{C}$ for 45 min. The addition of dry Et_2O led to precipitation of the dication salt. The precipitates were collected, washed with dry Et_2O three times, and dried *in vacuo* to give $3a^{2+}(\text{SbCl}_6^-)_2$ (44.4 mg) as a deep purple powder in 96% yield.

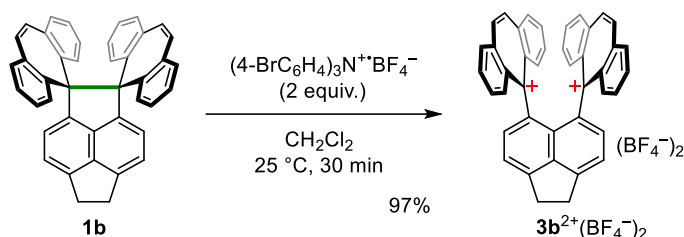
mp: 192-195 $^\circ\text{C}$ (decomp.); ^1H NMR (CD_3CN containing 10 vol% TFAA): δ 8.76 (dd, $J = 1.2, 8.4$ Hz, 2H), 8.69 (s, 4H), 8.38 (dd, $J = 1.4, 8.1$ Hz, 4H), 8.26 (ddd, $J = 1.1, 6.9, 8.1$ Hz, 4H), 8.05 (dd, $J = 7.1, 8.4$ Hz, 2H), 7.84 (d, $J = 1.1, 8.3$ Hz, 4H), 7.55 (ddd, $J = 1.4, 6.9, 8.3$ Hz, 4H), 7.49 (dd, $J = 1.2,$

7.1 Hz, 2H); IR (KBr): 3062, 2927, 1607, 1600, 1530, 1516, 1474, 1425, 1384, 1329, 1262, 1196, 1171, 1133, 1046, 1009, 895, 855, 834, 816, 801, 787, 769, 734 cm^{-1} ; LRMS (FD) m/z (%): 576.21 (6), 543.24 (6), 542.24 (18), 541.24 (22), 540.23 (43), 508.27 (11), 507.27 (44), 506.27 (M^+ , bp); HRMS (FD) m/z : [M] $^+$ calcd. for $\text{C}_{40}\text{H}_{26}$, 506.20345; found, 506.20228.

Oxidation of **2a** in solution:

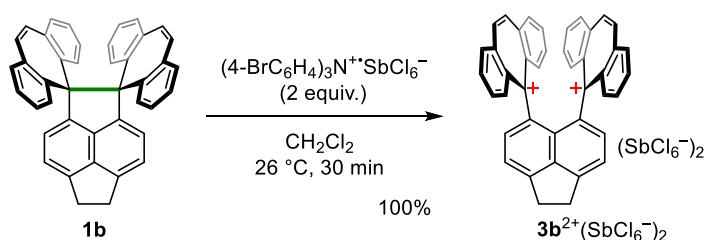


To a solution of **2a** (8.5 mg, 16.8 μmol) in dry CH_2Cl_2 (2 mL) was added tris(2,4-dibromophenyl)aminium hexachloroantimonate (35.3 mg, 33.5 μmol) at 25 $^\circ\text{C}$ to generate a deep purple solution, and the mixture was stirred at 25 $^\circ\text{C}$ for 30 min. The addition of dry Et_2O led to precipitation of the dication salt. The precipitates were collected, washed with dry Et_2O three times, and dried *in vacuo* to give **3a** $^{2+}(\text{SbCl}_6^-)_2$ (8.8 mg) as a deep purple powder in 45% yield.

Dicationic salt $3b^{2+}(BF_4^-)_2$ Oxidation of **1b** in solution:

To a solution of **1b** (53.6 mg, 101 μmol) in dry CH_2Cl_2 (5 mL) was added tris(4-bromophenyl)aminium tetrafluoroborate (115 mg, 201 μmol) at 25 $^\circ\text{C}$ to generate a deep purple solution, and the mixture was stirred at 25 $^\circ\text{C}$ for 30 min. The addition of dry Et_2O led to precipitation of the dication salt. The precipitates were collected, washed with dry Et_2O three times, and dried *in vacuo* to give $3b^{2+}(\text{BF}_4^-)_2$ (69.5 mg) as a deep purple powder in 97% yield.

Mp: > 300 $^\circ\text{C}$; $^1\text{H NMR}$ (CD_3CN): δ 8.72 (s, 4H), 8.33 (dd, $J = 1.5, 8.1$ Hz, 4H), 8.17 (ddd, $J = 1.0, 7.0, 8.1$ Hz, 4H), 7.97 (dd, $J = 1.0, 8.9$ Hz, 4H), 7.86 (d, $J = 7.2$ Hz, 2H), 7.57 (ddd, $J = 1.5, 7.0, 8.9$ Hz, 4H), 7.44 (d, $J = 7.2$ Hz, 2H), 3.91 (s, 4H); $^{13}\text{C NMR}$ (CD_3CN): δ 180.66, 152.00, 145.52, 145.40, 141.45, 140.49, 139.37, 138.66, 136.32, 134.29, 134.17, 132.74, 129.60, 120.81, 31.11; IR (KBr): 3059, 2927, 2360, 1601, 1516, 1478, 1385, 1329, 1208, 1053, 896, 862, 838, 798, 732 cm^{-1} ; LRMS (FD) m/z (%): 551.18 (7), 550.18 (15), 534.20 (11), 533.19 (46), 532.19 (M^+ , bp), 531.18 (8), 530.18 (17); HRMS (FD) m/z : [M] $^+$ calcd. for $\text{C}_{42}\text{H}_{28}$, 532.21910; found, 532.21750; UV/Vis (CH_2Cl_2): $\lambda_{\text{max}}/\text{nm}$ ($\epsilon/\text{L mol}^{-1} \text{cm}^{-1}$) 302 (114000), 380 (8310), 536 (5510).

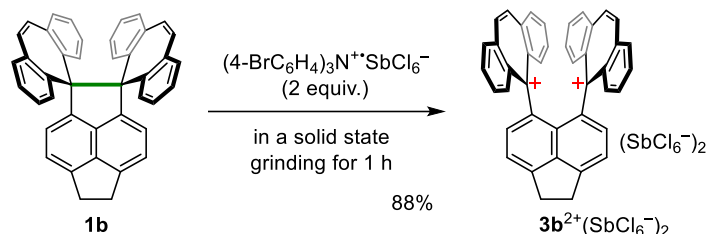
Dicationic salt $3b^{2+}(\text{SbCl}_6^-)_2$ Oxidation of **1b** in solution:

To a solution of **1b** (100 mg, 188 μmol) in dry CH_2Cl_2 (8 mL) was added tris(4-bromophenyl)aminium hexachloroantimonate (307 mg, 376 μmol) at 25 $^\circ\text{C}$ to generate a deep purple solution, and the mixture was stirred at 25 $^\circ\text{C}$ for 30 min. The addition of dry Et_2O led to precipitation of the dication salt. The precipitates were collected, washed with dry Et_2O three times, and dried *in vacuo* to give $3b^{2+}(\text{SbCl}_6^-)_2$ (226 mg) as a deep purple powder in 100% yield.

mp: 181-182 $^\circ\text{C}$; $^1\text{H NMR}$ (CD_3CN containing 10 vol% TFAA): δ 8.70 (s, 4H), 8.32 (dd, $J = 1.5, 8.1$ Hz, 4H), 8.18 (ddd, $J = 1.0, 7.0, 8.1$ Hz, 4H), 7.99 (dd, $J = 1.0, 8.9$ Hz, 4H), 7.87 (d, $J = 7.2$ Hz, 2H), 7.59 (ddd, $J = 1.5, 7.0, 8.9$ Hz, 4H), 7.45 (d, $J = 7.2$ Hz, 2H), 3.91 (s, 4H); IR (KBr): 3174, 3107, 2927, 2360, 1601, 1529, 1516, 1476, 1426, 1385, 1327, 1268, 1253, 1208, 1172, 1157, 1132, 1077, 1044, 1007, 894, 862, 834, 797, 771, 731 cm^{-1} ; LRMS (FD) m/z (%): 602.22 (26), 600.22 (39), 568.26 (30), 567.26 (35), 566.25 (74), 533.29 (43), 532.29 (M^+ , bp), 530.27 (26); HRMS (FD) m/z : [M] $^+$

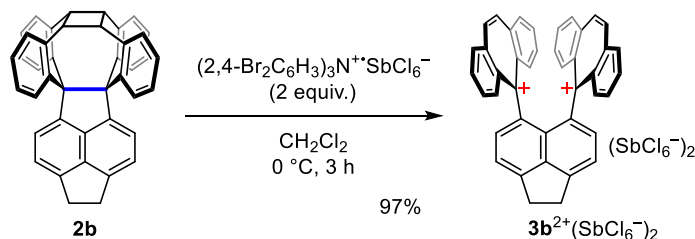
calcd. for $C_{42}H_{28}$, 532.21910, found, 532.22009.

Oxidation of **1b** in a solid state:



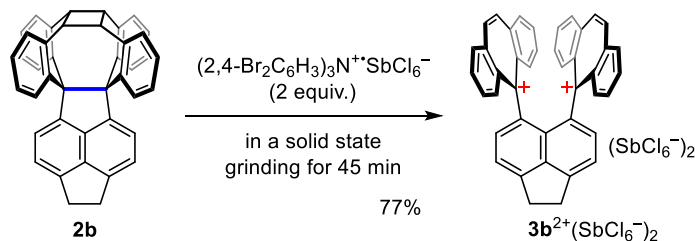
A mixture of **1b** (50.4 mg, 94.6 μmol) and tris(4-bromophenyl)aminium hexachloroantimonate (154 mg, 188 μmol) was ground for 1 h at 25 $^\circ\text{C}$ to generate a deep purple solid. The resulting powder was collected, washed with dry Et_2O three times, and dried *in vacuo* to give $\mathbf{3b}^{2+}(\text{SbCl}_6^-)_2$ (100 mg) as a deep purple powder in 88% yield.

Oxidation of **2b** in solution:

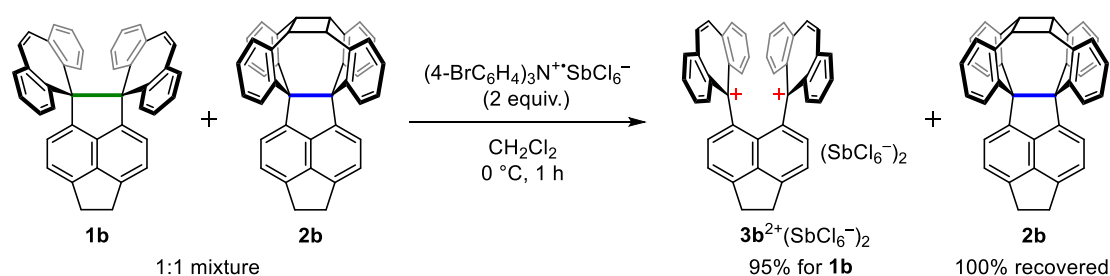


To a solution of **2b** (20.5 mg, 38.5 μmol) in dry CH_2Cl_2 (3 mL) was added tris(2,4-dibromophenyl)aminium hexachloroantimonate (81.2 mg, 77.1 μmol) at 0 $^\circ\text{C}$ to generate a deep purple solution, and the mixture was stirred at 0 $^\circ\text{C}$ for 3 h. The addition of dry Et_2O led to precipitation of the dication salt. The precipitates were collected, washed with dry Et_2O three times, and dried *in vacuo* to give $\mathbf{3b}^{2+}(\text{SbCl}_6^-)_2$ (45.0 mg) as a deep purple powder in 97% yield.

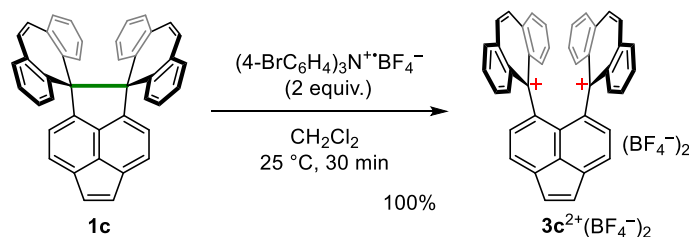
Oxidation of **2b** in a solid state:



A mixture of **2b** (49.2 mg, 92.4 μmol) and tris(2,4-dibromophenyl)aminium hexachloroantimonate (194 mg, 184 μmol) was ground for 45 min at 25 $^\circ\text{C}$ to generate a deep purple solid. The resulting powder was collected, washed with dry Et_2O three times, and dried *in vacuo* to give $\mathbf{3b}^{2+}(\text{SbCl}_6^-)_2$ (84.6 mg) as a deep purple powder in 77% yield.

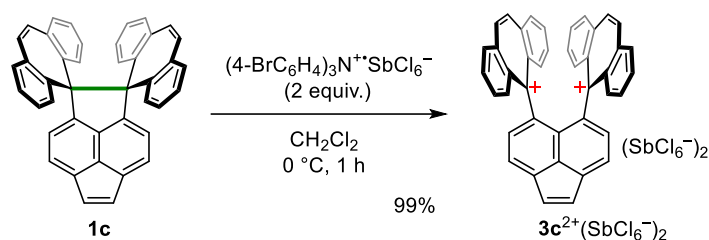
Selective oxidation of **1b** in a mixture of **1b** and **2b**:

To a solution of mixture of **1b** (49.1 mg, 92.2 μmol) and **2b** (49.2 mg, 92.4 μmol) in dry CH_2Cl_2 (4 mL) was added tris(4-bromophenyl)ammonium hexachloroantimonate (151 mg, 184 μmol) at 0 $^\circ\text{C}$, and the mixture was stirred for 1 h. The addition of dry Et_2O led to precipitation of the dication salt. The supernatant solution was removed by decantation. Then, the residue was suspended in dry CH_2Cl_2 , and the supernatant solution was removed by decantation. These procedures were repeated 3 times. The resulting residue was dried *in vacuo* to give **3b²⁺(SbCl₆⁻)₂** (105 mg) as a deep purple powder in 95% yield for **1b**. On the other hand, the combined filtrate was evaporated under reduced pressure. The residue was purified by silica gel column chromatography (hexane to CH_2Cl_2) to recover **2b** (49.2 mg) as a white solid in 100% yield for **2b**.

Dicationic salt **3c²⁺(BF₄⁻)₂**Oxidation of **1c** in solution:

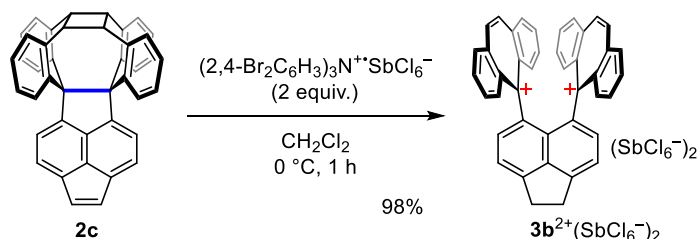
To a solution of **1c** (40.2 mg, 75.8 μmol) in dry CH_2Cl_2 (5 mL) was added tris(4-bromophenyl)ammonium tetrafluoroborate (86.1 mg, 151 μmol) at 25 $^\circ\text{C}$ to generate a deep purple solution, and the mixture was stirred at 25 $^\circ\text{C}$ for 30 min. The addition of dry Et_2O led to precipitation of the dication salt. The precipitates were collected, washed with dry Et_2O three times, and dried *in vacuo* to give **3c²⁺(BF₄⁻)₂** (53.7 mg) as a deep purple powder in 100% yield.

Mp: > 300 $^\circ\text{C}$; ^1H NMR (CD_3CN containing 10 vol% TFA-*d*): δ 8.76 (s, 4H), 8.36 (dd, $J = 1.2, 8.0$ Hz, 4H), 8.19 (ddd, $J = 1.1, 6.9, 8.0$ Hz, 4H), 8.17 (d, $J = 7.0$ Hz, 2H), 8.06 (brd, $J = 8.8$ Hz, 4H), 7.58 (s, 2H), 7.57 (ddd, $J = 1.2, 6.9, 8.8$ Hz, 4H), 7.51 (d, $J = 7.0$ Hz, 2H); ^{13}C NMR (CD_3CN containing 10 vol% TFA-*d*): δ 179.38, 146.01, 145.53, 143.74, 141.79, 139.53, 138.57, 137.66, 136.64, 134.77, 133.66, 132.48, 129.87, 127.15, 125.40; IR (KBr): 3059, 2360, 2343, 1604, 1516, 1478, 1427, 1385, 1331, 1197, 1055, 899, 855, 840, 799, 775, 733 cm^{-1} ; LRMS (FD) m/z (%): 566.15 (8), 549.17 (6), 548.16 (13), 546.16 (5), 532.18 (12), 531.18 (46), 530.17 (M^+ , bp); HRMS (FD) m/z : [M]⁺ calcd. for $\text{C}_{42}\text{H}_{26}$, 530.20345; found, 530.20405; UV/Vis (CH_2Cl_2): $\lambda_{\text{max}}/\text{nm}$ ($\epsilon/\text{L mol}^{-1} \text{cm}^{-1}$) 302 (82400), 384 (7740), 542 (5630).

Dicationic salt $3c^{2+}(\text{SbCl}_6^-)_2$ Oxidation of **1c** in solution:

To a solution of **1c** (20.1 mg, 37.9 μmol) in dry CH_2Cl_2 (2 mL) was added tris(4-bromophenyl)aminium hexachloroantimonate (61.6 mg, 75.4 μmol) at 0 $^\circ\text{C}$ to generate a deep purple solution, and the mixture was stirred at 0 $^\circ\text{C}$ for 1 h. The addition of dry Et_2O led to precipitation of the dication salt. The precipitates were collected, washed with dry Et_2O three times, and dried *in vacuo* to give $3c^{2+}(\text{SbCl}_6^-)_2$ (45.0 mg) as a deep purple powder in 99% yield.

mp: 190-195 $^\circ\text{C}$; $^1\text{H NMR}$ (CD_3CN containing 10 vol% TFAA): δ 8.74 (s, 4H), 8.37 (brd, $J = 7.8$ Hz, 4H), 8.22-8.19 (m, 6H), 8.06 (brd, $J = 8.8$ Hz, 4H), 7.60-7.56 (m, 6H), 7.52 (d, $J = 7.0$ Hz, 2H); IR (KBr): 3081, 1666, 1660, 1602, 1530, 1515, 1504, 1495, 1480, 1463, 1453, 1427, 1387, 1357, 1331, 1265, 1209, 1197, 1172, 1158, 1132, 1094, 1044, 939, 893, 865, 834, 796, 780, 773, 731, 675, 642, 608 cm^{-1} ; LRMS (FD) m/z (%): 600.20 (23), 599.21 (26), 598.20 (26), 566.24 (18), 565.24 (23), 564.24 (44), 547.27 (13), 546.27 (31), 532.28 (13), 531.28 (51), 530.27 (M^+ , bp); HRMS (FD) m/z : [M] $^+$ calcd. for $\text{C}_{42}\text{H}_{26}$, 530.20345; found, 530.20437.

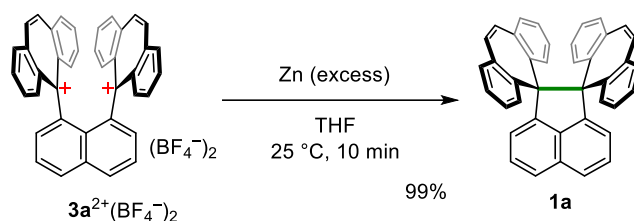
Oxidation of **2c** in solution:

To a solution of **2c** (10.4 mg, 19.6 μmol) in dry CH_2Cl_2 (1.0 mL) was added tris(2,4-dibromophenyl)aminium hexachloroantimonate (41.2 mg, 39.1 μmol) at 0 $^\circ\text{C}$ to generate a deep purple solution, and the mixture was stirred at 0 $^\circ\text{C}$ for 1 h. The addition of dry Et_2O led to precipitation of the dication salt. The precipitates were collected, washed with dry Et_2O three times, and dried *in vacuo* to give $3b^{2+}(\text{SbCl}_6^-)_2$ (23.1 mg) as a deep purple powder in 98% yield.

• Preparation of spiro-DBCHT **1a-1c**

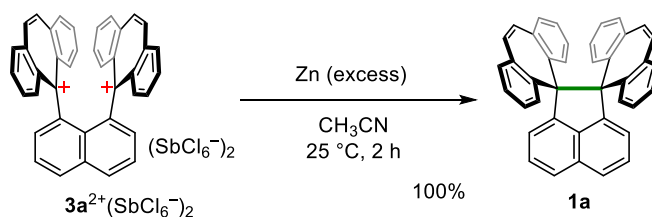
Spiro-DBCHT 1a

Reduction of $3a^{2+}(BF_4^-)_2$ in solution:



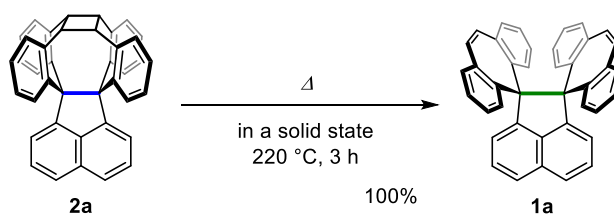
To a solution of $3a^{2+}(BF_4^-)_2$ (30.0 mg, 44.1 μmol) in dry THF (2 mL) was added activated zinc powder (434 mg, 6.64 mmol) at 25 $^\circ\text{C}$. The mixture was stirred for 10 min, and then diluted with water. The whole mixture was extracted with CHCl_3 three times. The combined organic layers were washed with water and brine, and dried over anhydrous MgSO_4 . After filtration through a silica gel pad, the solvent was concentrated under reduced pressure and dried *in vacuo* to give **1a** (22.2 mg) as a white solid in 99% yield.

Reduction of $3a^{2+}(\text{SbCl}_6^-)_2$ in solution:

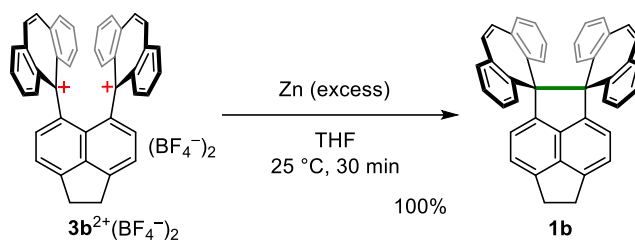


To a solution of $3a^{2+}(\text{SbCl}_6^-)_2$ (104 mg, 88.2 μmol) in dry CH_3CN (4 mL) was added activated zinc powder (865 mg, 13.2 mmol) at 25 $^\circ\text{C}$ in the dark. The mixture was stirred for 2 h in the dark, and then diluted with water. The whole mixture was extracted with CHCl_3 three times. The combined organic layers were washed with water and brine, and dried over anhydrous MgSO_4 . After filtration, the solvent was concentrated under reduced pressure and dried *in vacuo* to give **1a** (44.5 mg) as a white solid in 100% yield.

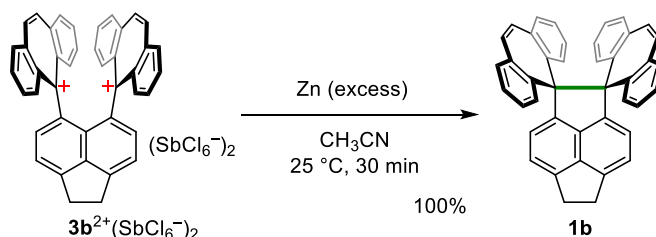
Thermal isomerization of **2a** in a solid state:



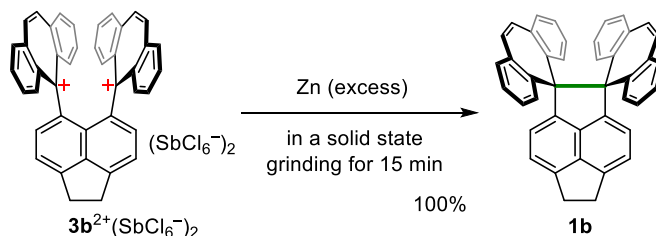
A solid of **2a** (1.6 mg, 3.16 μmol) was heated at 220 $^\circ\text{C}$ for 3 h to give **1a** (1.6 mg) as a white solid in 100% yield.

Spiro-DBCHT 1bReduction of $3b^{2+}(BF_4^-)_2$ in solution:

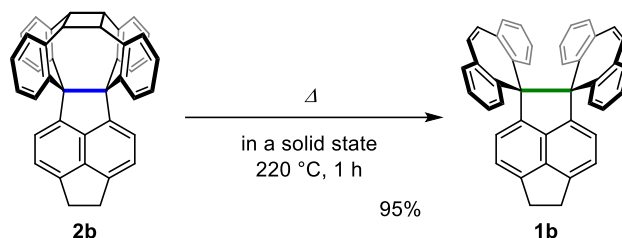
To a solution of $3b^{2+}(BF_4^-)_2$ (54.4 mg, 44.1 μmol) in dry THF (4 mL) was added activated zinc powder (756 mg, 11.6 mmol) at 25 $^\circ\text{C}$. The mixture was stirred for 30 min, and then diluted with water. The whole mixture was extracted with CHCl_3 three times. The combined organic layers were washed with water and brine, and dried over anhydrous MgSO_4 . After filtration through a silica gel pad, the solvent was concentrated under reduced pressure and dried *in vacuo* to give **1b** (40.9 mg) as a white solid in 100% yield.

Reduction of $3b^{2+}(\text{SbCl}_6^-)_2$ in solution:

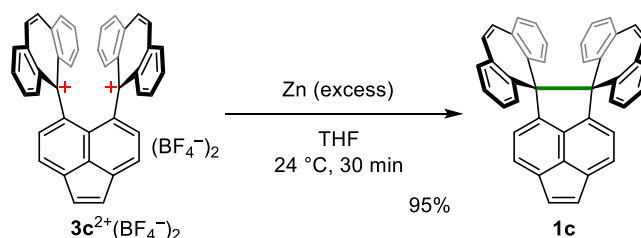
To a solution of $3b^{2+}(\text{SbCl}_6^-)_2$ (116 mg, 96.9 μmol) in dry CH_3CN (4 mL) was added activated zinc powder (974 mg, 14.9 mmol) at 25 $^\circ\text{C}$. The mixture was stirred for 30 min, and then diluted with water. The whole mixture was extracted with CHCl_3 three times. The combined organic layers were washed with water and brine, and dried over anhydrous MgSO_4 . After filtration, the solvent was concentrated under reduced pressure and dried *in vacuo* to give **1b** (51.4 mg) as a white solid in 100% yield.

Reduction of $3b^{2+}(\text{SbCl}_6^-)_2$ in a solid state:

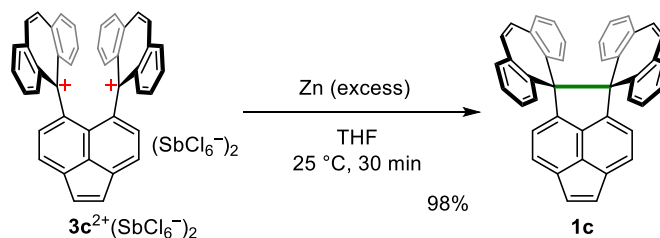
A mixture of $3b^{2+}(\text{SbCl}_6^-)_2$ (100 mg, 83.4 μmol) and activated zinc powder (1.09 g, 16.6 mmol) was ground for 15 min at 25 $^\circ\text{C}$. The resulting powder was dissolved in CHCl_3 , and then the resulting suspension was filtered through filter paper. The filtrate was washed with water and brine, and dried over anhydrous MgSO_4 . After filtration through a silica gel pad, the solvent was evaporated and dried *in vacuo* to give **1b** (44.3 mg) as a white solid in 100% yield.

Thermal isomerization of **2b** in a solid state:

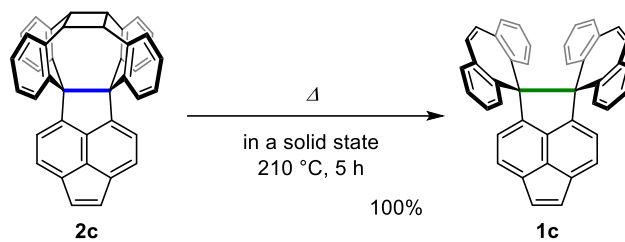
A solid of **2b** (2.1 mg, 3.94 μmol) was heated at 220 $^\circ\text{C}$ for 1 h to give **1b** (2.0 mg) as a white solid in 95% yield.

Spiro-DBCHT 1cReduction of $3\text{c}^{2+}(\text{BF}_4^-)_2$ in solution:

To a solution of $3\text{c}^{2+}(\text{BF}_4^-)_2$ (20.7 mg, 29.4 μmol) in dry THF (2 mL) was added activated zinc powder (288 mg, 4.40 mmol) at 24 $^\circ\text{C}$. The mixture was stirred for 30 min, and then diluted with water. The whole mixture was extracted with CHCl_3 three times. The combined organic layers were washed with water and brine, and dried over anhydrous MgSO_4 . After filtration through a silica gel pad, the solvent was concentrated under reduced pressure and dried *in vacuo* to give **1c** (14.8 mg) as a yellow solid in 95% yield.

Reduction of $3\text{c}^{2+}(\text{SbCl}_6^-)_2$ in solution:

To a solution of $3\text{c}^{2+}(\text{SbCl}_6^-)_2$ (19.1 mg, 15.9 μmol) in dry THF (2 mL) was added activated zinc powder (157 mg, 2.39 mmol) at 25 $^\circ\text{C}$. The mixture was stirred for 30 min, and then diluted with water. The whole mixture was extracted with CHCl_3 three times. The combined organic layers were washed with water and brine, and dried over anhydrous MgSO_4 . After filtration through a silica gel pad, the solvent was concentrated under reduced pressure and dried *in vacuo* to give **1c** (8.2 mg) as a yellow solid in 98% yield.

Thermal isomerization of **2c** in a solid state:

A solid of **2c** (3.1 mg, 5.84 μmol) was heated at 210 °C for 5 h to give **1c** (3.1 mg) as a yellow solid in 100% yield.

X-ray analyses

Data were collected with a Rigaku Mercury 70 diffractometer (Mo-K α radiation, $\lambda = 0.71075 \text{ \AA}$) for dications or a Rigaku XtaLAB Synergy (Cu-K α radiation, $\lambda = 1.54184 \text{ \AA}$) for others. The structure was solved by the direct method (SIR2004) and ShelXT (Sheldrick) for dications and others, respectively, and refined by the full-matrix least-squares method on F^2 with anisotropic temperature factors for non-hydrogen atoms. All the hydrogen atoms were located at the calculated positions and refined with riding. A Rigaku CrystalStructure crystallographic software package and Olex2^[48] were used for all calculations for dications and others, respectively.

Crystal data for 1a: CCDC 1586191 (at 120 K), 1586192 (at 160 K), 1567390 (at 200 K), 1567391 (at 240 K), 1567392 (at 280 K), 1567393 (at 320 K), 1567394 (at 360 K), 1567395 (at 400 K)^[16]

Crystal data for 1b: CCDC 1567396 (200 K), 1567397 (at 240 K), 1567398 (at 280 K), 1567399 (at 320 K), 1567400 (at 360 K), 1567401 (at 400 K)^[16]

at 300 K (CCDC 2005623)

Crystals, colorless block, $0.8 \times 0.4 \times 0.2 \text{ mm}^3$, were obtained by recrystallization from CHCl₃/hexane
Crystal Data for C₄₂H₂₈ ($M=532.64 \text{ g/mol}$): monoclinic, space group $P2_1/c$ (#14), $a = 12.79971(16) \text{ \AA}$, $b = 9.22089(12) \text{ \AA}$, $c = 24.0558(3) \text{ \AA}$, $\beta = 100.0421(11)^\circ$, $V = 2795.68(6) \text{ \AA}^3$, $Z = 4$, $T = 300 \text{ K}$, μ (CuK α) = 0.543 mm^{-1} , $D_{calc} = 1.265 \text{ g/cm}^3$, 18751 reflections measured ($7.014^\circ \leq 2\theta \leq 151.596^\circ$), 5646 unique ($R_{int} = 0.0447$, $R_{sigma} = 0.0314$) which were used in all calculations. The final R_1 was 0.0879 ($I > 2 \sigma(I)$) and wR_2 was 0.2601 (all data).

Crystal data for 1c: CCDC 1586193 (100 K), 1586194 (120 K), 1586195 (160 K), 1567402 (200 K), 1567403 (240 K), 1567404 (280 K), 1567405 (320 K), 1567406 (360 K), 1567407 (400 K)^[16]

Crystal data for 2a·0.5CH₂Cl₂: Crystals, colorless plate, $0.6 \times 0.2 \times 0.05 \text{ mm}^3$, were obtained by recrystallization from CH₂Cl₂/hexane

at 100 K (CCDC 2005624)

Crystal Data for C_{40.5}H₂₇Cl ($M=549.07 \text{ g/mol}$): monoclinic, space group $P2_1$ (#4), $a = 10.57274(8) \text{ \AA}$, $b = 29.7730(2) \text{ \AA}$, $c = 8.67995(7) \text{ \AA}$, $\beta = 104.9856(8)^\circ$, $V = 2639.37(4) \text{ \AA}^3$, $Z = 4$, $T = 100 \text{ K}$, μ (CuK α) = 1.500 mm^{-1} , $D_{calc} = 1.382 \text{ g/cm}^3$, 18866 reflections measured ($5.936^\circ \leq 2\theta \leq 151.872^\circ$), 9715 unique ($R_{int} = 0.0534$, $R_{sigma} = 0.0501$) which were used in all calculations. The final R_1 was 0.0528 ($I > 2 \sigma(I)$) and wR_2 was 0.1606 (all data). Solvent mask procedure was used for the analysis.

at 200 K (CCDC 2005625)

Crystal Data for C_{40.5}H₂₇Cl ($M=549.07 \text{ g/mol}$): monoclinic, space group $P2_1$ (#4), $a = 10.61353(10) \text{ \AA}$, $b = 29.8550(2) \text{ \AA}$, $c = 8.72432(7) \text{ \AA}$, $\beta = 104.9965(8)^\circ$, $V = 2670.30(4) \text{ \AA}^3$, $Z =$

4, $T = 200$ K, μ (CuK α) = 1.483 mm⁻¹, $D_{calc} = 1.366$ g/cm³, 18712 reflections measured ($5.92^\circ \leq 2\theta \leq 151.402^\circ$), 9078 unique ($R_{int} = 0.0390$, $R_{sigma} = 0.0403$) which were used in all calculations. The final R_1 was 0.0529 ($I > 2 \sigma(I)$) and wR_2 was 0.1620 (all data).

at 300 K (CCDC 2005626)

Crystal Data for C_{40.5}H₂₇Cl ($M = 549.07$ g/mol): monoclinic, space group $P2_1/c$ (#14), $a = 10.66505(11)$ Å, $b = 29.9399(3)$ Å, $c = 8.77371(8)$ Å, $\beta = 105.0238(9)^\circ$, $V = 2705.77(5)$ Å³, $Z = 4$, $T = 300$ K, μ (CuK α) = 1.463 mm⁻¹, $D_{calc} = 1.348$ g/cm³, 19356 reflections measured ($5.904^\circ \leq 2\theta \leq 151.35^\circ$), 5481 unique ($R_{int} = 0.0301$, $R_{sigma} = 0.0257$) which were used in all calculations. The final R_1 was 0.0429 ($I > 2 \sigma(I)$) and wR_2 was 0.1235 (all data). Solvent mask procedure was used for the analysis.

Crystal data for 2b: Crystals, colorless plate, $0.6 \times 0.2 \times 0.01$ mm³, were obtained by recrystallization from CHCl₃/hexane

100 K (CCDC 2005627)

Crystal Data for C₄₂H₂₈ ($M = 532.64$ g/mol): monoclinic, space group $P2_1/c$ (#14), $a = 13.25388(13)$ Å, $b = 8.74148(10)$ Å, $c = 23.6015(2)$ Å, $\beta = 97.1751(8)^\circ$, $V = 2713.02(5)$ Å³, $Z = 4$, $T = 100$ K, μ (CuK α) = 0.559 mm⁻¹, $D_{calc} = 1.304$ g/cm³, 19174 reflections measured ($6.722^\circ \leq 2\theta \leq 151.564^\circ$), 5451 unique ($R_{int} = 0.0286$, $R_{sigma} = 0.0244$) which were used in all calculations. The final R_1 was 0.0416 ($I > 2 \sigma(I)$) and wR_2 was 0.1087 (all data).

at 200 K (CCDC 2005628)

Crystal Data for C₄₂H₂₈ ($M = 532.64$ g/mol): monoclinic, space group $P2_1/c$ (#14), $a = 13.25273(12)$ Å, $b = 8.78403(9)$ Å, $c = 23.6979(2)$ Å, $\beta = 97.1488(8)^\circ$, $V = 2737.28(4)$ Å³, $Z = 4$, $T = 200$ K, μ (CuK α) = 0.554 mm⁻¹, $D_{calc} = 1.292$ g/cm³, 18497 reflections measured ($6.722^\circ \leq 2\theta \leq 151.798^\circ$), 5485 unique ($R_{int} = 0.0248$, $R_{sigma} = 0.0224$) which were used in all calculations. The final R_1 was 0.0422 ($I > 2 \sigma(I)$) and wR_2 was 0.1147 (all data).

at 300 K (CCDC 2005629)

Crystal Data for C₄₂H₂₈ ($M = 532.64$ g/mol): monoclinic, space group $P2_1/c$ (#14), $a = 13.26469(12)$ Å, $b = 8.83221(9)$ Å, $c = 23.79279(19)$ Å, $\beta = 97.2129(8)^\circ$, $V = 2765.42(4)$ Å³, $Z = 4$, $T = 300$ K, μ (CuK α) = 0.549 mm⁻¹, $D_{calc} = 1.279$ g/cm³, 19896 reflections measured ($6.716^\circ \leq 2\theta \leq 151.63^\circ$), 5525 unique ($R_{int} = 0.0254$, $R_{sigma} = 0.0245$) which were used in all calculations. The final R_1 was 0.0423 ($I > 2 \sigma(I)$) and wR_2 was 0.1223 (all data).

at 400 K (CCDC 2005630)

Crystal Data for C₄₂H₂₈ ($M = 532.64$ g/mol): monoclinic, space group $P2_1/c$ (#14), $a = 13.3028(8)$ Å, $b = 8.9258(6)$ Å, $c = 23.8898(17)$ Å, $\beta = 97.369(7)^\circ$, $V = 2813.2(3)$ Å³, $Z = 4$, $T = 400$ K, μ (CuK α) = 0.539 mm⁻¹, $D_{calc} = 1.258$ g/cm³, 14819 reflections measured ($6.7^\circ \leq 2\theta \leq 151.576^\circ$), 5620 unique ($R_{int} = 0.0636$, $R_{sigma} = 0.0585$) which were used in all calculations. The

final R_1 was 0.0940 ($I > 2 \sigma(I)$) and wR_2 was 0.2884 (all data).

Crystal data of 2c: Crystals, yellow plate, $0.3 \times 0.3 \times 0.03 \text{ mm}^3$, were obtained by recrystallization from $\text{CH}_2\text{Cl}_2/\text{hexane}$

100 K (CCDC 2005631)

Crystal Data for $\text{C}_{42}\text{H}_{26}$ ($M=530.63 \text{ g/mol}$): monoclinic, space group $P2_1/n$ (#14), $a = 10.0184(2) \text{ \AA}$, $b = 17.6572(3) \text{ \AA}$, $c = 15.6318(3) \text{ \AA}$, $\beta = 106.398(2)^\circ$, $V = 2652.73(9) \text{ \AA}^3$, $Z = 4$, $T = 100 \text{ K}$, μ (CuK α) = 0.572 mm^{-1} , $D_{\text{calc}} = 1.329 \text{ g/cm}^3$, 17007 reflections measured ($7.734^\circ \leq 2\theta \leq 151.748^\circ$), 5342 unique ($R_{\text{int}} = 0.0347$, $R_{\text{sigma}} = 0.0293$) which were used in all calculations. The final R_1 was 0.0543 ($I > 2 \sigma(I)$) and wR_2 was 0.1503 (all data).

at 200 K (CCDC 2005632)

Crystal Data for $\text{C}_{42}\text{H}_{26}$ ($M=530.63 \text{ g/mol}$): monoclinic, space group $P2_1/n$ (#14), $a = 10.02597(16) \text{ \AA}$, $b = 17.7295(2) \text{ \AA}$, $c = 15.7006(3) \text{ \AA}$, $\beta = 106.5276(17)^\circ$, $V = 2675.56(7) \text{ \AA}^3$, $Z = 4$, $T = 200 \text{ K}$, μ (CuK α) = 0.567 mm^{-1} , $D_{\text{calc}} = 1.317 \text{ g/cm}^3$, 16695 reflections measured ($7.704^\circ \leq 2\theta \leq 151.728^\circ$), 5397 unique ($R_{\text{int}} = 0.0468$, $R_{\text{sigma}} = 0.0337$) which were used in all calculations. The final R_1 was 0.0597 ($I > 2 \sigma(I)$) and wR_2 was 0.1655 (all data).

at 300 K (CCDC 2005633)

Crystal Data for $\text{C}_{42}\text{H}_{26}$ ($M=530.63 \text{ g/mol}$): monoclinic, space group $P2_1/n$ (#14), $a = 10.03723(15) \text{ \AA}$, $b = 17.8005(2) \text{ \AA}$, $c = 15.7928(2) \text{ \AA}$, $\beta = 106.6931(15)^\circ$, $V = 2702.74(7) \text{ \AA}^3$, $Z = 4$, $T = 300 \text{ K}$, μ (CuK α) = 0.561 mm^{-1} , $D_{\text{calc}} = 1.304 \text{ g/cm}^3$, 18421 reflections measured ($7.67^\circ \leq 2\theta \leq 151.552^\circ$), 5430 unique ($R_{\text{int}} = 0.0311$, $R_{\text{sigma}} = 0.0242$) which were used in all calculations. The final R_1 was 0.0464 ($I > 2 \sigma(I)$) and wR_2 was 0.1285 (all data).

at 400 K (CCDC 2005634)

Crystal Data for $\text{C}_{42}\text{H}_{26}$ ($M=530.63 \text{ g/mol}$): monoclinic, space group $P2_1/n$ (#14), $a = 10.0545(2) \text{ \AA}$, $b = 17.8873(3) \text{ \AA}$, $c = 15.8817(3) \text{ \AA}$, $\beta = 106.890(2)^\circ$, $V = 2733.10(9) \text{ \AA}^3$, $Z = 4$, $T = 400 \text{ K}$, μ (CuK α) = 0.555 mm^{-1} , $D_{\text{calc}} = 1.290 \text{ g/cm}^3$, 16746 reflections measured ($7.634^\circ \leq 2\theta \leq 152.658^\circ$), 5509 unique ($R_{\text{int}} = 0.0346$, $R_{\text{sigma}} = 0.0268$) which were used in all calculations. The final R_1 was 0.0512 ($I > 2 \sigma(I)$) and wR_2 was 0.1477 (all data).

Crystal data for $3\text{a}^{2+}(\text{SbCl}_6^-)_2 \cdot \text{CH}_3\text{CN}$: Crystals, purple plate, $0.4 \times 0.1 \times 0.02 \text{ mm}^3$, were obtained by recrystallization from $\text{CH}_3\text{CN}/\text{Et}_2\text{O}$.

Crystal Data for $\text{C}_{42}\text{H}_{29}\text{Cl}_{12}\text{NSb}_2$ ($M=1216.63 \text{ g/mol}$): monoclinic, space group $P2_1/c$ (#14), $a = 28.596(8) \text{ \AA}$, $b = 13.285(4) \text{ \AA}$, $c = 27.746(8) \text{ \AA}$, $\beta = 118.185(5)^\circ$, $V = 9291(5) \text{ \AA}^3$, $Z = 8$, $T = 150 \text{ K}$, μ (MoK α) = 1.8827 mm^{-1} , $D_{\text{calc}} = 1.739 \text{ g/cm}^3$, 33560 reflections measured ($2\theta_{\text{max}} = 55.0^\circ$), 17935 unique ($R_{\text{int}} = 0.0484$) which were used in all calculations. The final R_1 was 0.0600 ($I > 2\sigma(I)$) and wR_2 was 0.1878 (all data). CCDC 2005635

Crystal data for $3\text{b}^{2+}(\text{SbCl}_6^-)_2$: Crystals, purple needle, $0.3 \times 0.05 \times 0.05 \text{ mm}^3$, were obtained by

recrystallization from CH₃CN/Et₂O.

Crystal Data for C₄₂H₂₈Cl₁₂Sb₂ (*M* = 1201.62 g/mol): orthorhombic, space group *Pbcn* (#60), *a* = 10.220(2) Å, *b* = 24.166(5) Å, *c* = 18.191(4) Å, *V* = 4493(2) Å³, *Z* = 4, *T* = 150 K, μ (MoK α) = 1.9449 mm⁻¹, *D*_{calc} = 1.776 g/cm³, 23381 reflections measured ($2\theta_{\max}$ = 55.0°), 4396 unique (*R*_{int} = 0.1164) which were used in all calculations. The final *R*₁ was 0.0851 (*I* > 2 σ (*I*)) and *wR*₂ was 0.2275 (all data). CCDC 2005636

Crystal data for 3c²⁺(SbCl⁶⁻)₂ · 0.5C₄H₁₀O: Crystals, purple plate, 0.6 × 0.1 × 0.02 mm³, were obtained by recrystallization from CH₃CN/Et₂O.

Crystal Data for C₄₄H₃₁Cl₁₂O_{0.50}Sb₂ (*M* = 1236.66 g/mol): triclinic, space group *P* $\bar{1}$ (#2), *a* = 12.055(7) Å, *b* = 13.961(6) Å, *c* = 14.973(8) Å, α = 73.66(3)°, β = 78.70(3)°, γ = 71.47(3)°, *V* = 2277(2) Å³, *Z* = 2, *T* = 150 K, μ (MoK α) = 1.9223 mm⁻¹, *D*_{calc} = 1.804 g/cm³, 16595 reflections measured ($2\theta_{\max}$ = 55.1°), 8772 unique (*R*_{int} = 0.0423) which were used in all calculations. The final *R*₁ was 0.0562 (*I* > 2 σ (*I*)) and *wR*₂ was 0.1524 (all data). CCDC 2005637

SCSC photocyclization of 1b with λ > 390 nm

Photoirradiation for 10 h, measured at 200 K (1b/2b = 55/45).

Crystals, colorless block, 0.4 × 0.2 × 0.2 mm³, were obtained by recrystallization from CHCl₃/hexane, which was used for photoreaction in a glass tube [Xe lamp with corning color filter (No. 3-73)].

Crystal Data for C₄₂H₂₈ (*M* = 532.64 g/mol): monoclinic, space group *P*2₁/*c* (#14), *a* = 12.9352(3) Å, *b* = 9.05991(18) Å, *c* = 23.7724(4) Å, β = 98.6273(16)°, *V* = 2754.41(9) Å³, *Z* = 4, *T* = 200 K, μ (CuK α) = 0.551 mm⁻¹, *D*_{calc} = 1.284 g/cm³, 16829 reflections measured (6.912° ≤ 2θ ≤ 151.766°), 5575 unique (*R*_{int} = 0.0179, *R*_{sigma} = 0.0179) which were used in all calculations. The final *R*₁ was 0.0672 (*I* > 2 σ (*I*)) and *wR*₂ was 0.1883 (all data). CCDC 2005638

Photoirradiation for 60 h, measured at 200 K (1b/2b = 0/100).

Crystals, colorless block, 0.6 × 0.3 × 0.15 mm³, were obtained by recrystallization from CHCl₃/hexane, which was used for photoreaction in a glass tube [Xe lamp with corning color filter (No. 3-73)].

Crystal Data for C₄₂H₂₈ (*M* = 532.64 g/mol): monoclinic, space group *P*2₁/*c* (#14), *a* = 13.26411(14) Å, *b* = 8.78016(8) Å, *c* = 23.6884(2) Å, β = 97.1720(9)°, *V* = 2737.19(5) Å³, *Z* = 4, *T* = 200 K, μ (CuK α) = 0.554 mm⁻¹, *D*_{calc} = 1.293 g/cm³, 17430 reflections measured (6.716° ≤ 2θ ≤ 151.468°), 5530 unique (*R*_{int} = 0.0239, *R*_{sigma} = 0.0230) which were used in all calculations. The final *R*₁ was 0.0411 (*I* > 2 σ (*I*)) and *wR*₂ was 0.1099 (all data). CCDC 2005639

SCSC thermal isomerization from 2b upon heating at 493 K

Heating for 10 min, measured at 300 K (2b/1b = 82/18).

Crystals, colorless plate, 0.8 × 0.2 × 0.05 mm³, were obtained by recrystallization from CHCl₃/hexane, which was used for thermal reaction in a glass tube.

Crystal Data for C₄₂H₂₈ (*M* = 532.64 g/mol): monoclinic, space group *P*2₁/*c* (#14), *a* = 13.1312(2) Å, *b* = 8.93972(15) Å, *c* = 23.8993(4) Å, β = 97.3675(17)°, *V* = 2782.36(8) Å³, *Z* = 4, *T* = 300 K, μ (CuK α) = 0.545 mm⁻¹, *D*_{calc} = 1.272 g/cm³, 17631 reflections measured (6.788° ≤ 2θ ≤

151.838°), 5621 unique ($R_{\text{int}} = 0.0337$, $R_{\text{sigma}} = 0.0322$) which were used in all calculations. The final R_1 was 0.0559 ($I > 2\sigma(I)$) and wR_2 was 0.1727 (all data). CCDC 2005640

Heating for 60 min, measured at 300 K ($2b/1b = 0/100$).

Crystals, colorless plate, $0.3 \times 0.05 \times 0.02 \text{ mm}^3$, were obtained by recrystallization from $\text{CHCl}_3/\text{hexane}$, which was used for thermal reaction in a glass tube.

Crystal Data for $\text{C}_{42}\text{H}_{28}$ ($M = 532.64 \text{ g/mol}$): monoclinic, space group $P2_1/c$ (#14), $a = 12.8016(3) \text{ \AA}$, $b = 9.2206(3) \text{ \AA}$, $c = 24.0574(7) \text{ \AA}$, $\beta = 99.953(3)^\circ$, $V = 2796.97(13) \text{ \AA}^3$, $Z = 4$, $T = 300 \text{ K}$, $\mu (\text{CuK}\alpha) = 0.543 \text{ mm}^{-1}$, $D_{\text{calc}} = 1.265 \text{ g/cm}^3$, 16555 reflections measured ($7.01^\circ \leq 2\theta \leq 151.956^\circ$), 5627 unique ($R_{\text{int}} = 0.0262$, $R_{\text{sigma}} = 0.0258$) which were used in all calculations. The final R_1 was 0.0751 ($I > 2\sigma(I)$) and wR_2 was 0.2329 (all data). CCDC 200564

3-5. References

- [1] M. A. Majewski, M. Stępień, *Angew. Chem. Int. Ed.* **2019**, *58*, 86–116.
- [2] M. Saito, H. Shinokubo, H. Sakurai, *Mater. Chem. Front.* **2018**, *2*, 635–661.
- [3] S. H. Pun, Q. Miao, *Acc. Chem. Res.* **2018**, *51*, 1630–1642.
- [4] T. Hosokawa, Y. Takahashi, T. Matsushima, S. Watanabe, S. Kikkawa, I. Azumaya, A. Tsurusaki, K. Kamikawa, *J. Am. Chem. Soc.* **2017**, *139*, 18512–18521.
- [5] P. Hu, T. S. Heng, A. Osuka, W. Zeng, C. Chi, J. Ding, J. Siegel, H. Phan, Q. Wang, T. Y. Gopalakrishna, J. Wu, T. Tanaka, *Chem. Sci.* **2018**, *9*, 5100–5105.
- [6] Y. Nakakuki, T. Hirose, K. Matsuda, *J. Am. Chem. Soc.* **2018**, *140*, 15461–15469.
- [7] Y. Xiao, J. T. Mague, R. H. Schmehl, F. M. Haque, R. A. Pascal, *Angew. Chem. Int. Ed.* **2019**, *58*, 2831–2833.
- [8] Y. Hu, G. M. Paternò, X.-Y. Wang, X.-C. Wang, M. Guizzardi, Q. Chen, D. Schollmeyer, X.-Y. Cao, G. Cerullo, F. Scotognella, K. Müllen, A. Narita, *J. Am. Chem. Soc.* **2019**, *141*, 12797–12803.
- [9] G. Povie, Y. Segawa, T. Nishihara, Y. Miyauchi, K. Itami, *Science* **2017**, *356*, 172–175.
- [10] K. Y. Cheung, S. Gui, C. Deng, H. Liang, Z. Xia, Z. Liu, L. Chi, Q. Miao, *Chem* **2019**, *5*, 838–847.
- [11] Y. Segawa, M. Kuwayama, Y. Hijikata, M. Fushimi, T. Nishihara, J. Pirillo, J. Shirasaki, N. Kubota, K. Itami, *Science* **2019**, *365*, 272–276.
- [12] Y. Ni, T. Y. Gopalakrishna, H. Phan, T. Kim, T. S. Heng, Y. Han, T. Tao, J. Ding, D. Kim, J. Wu, *Nat. Chem.* **2020**, *12*, 242–248.
- [13] M. Rickhaus, M. Jirasek, L. Tejerina, H. Gotfredsen, M. D. Peeks, R. Haver, H.-W. Jiang, T. D. W. Claridge, H. L. Anderson, *Nat. Chem.* **2020**, *12*, 236–241.
- [14] T. Mio, K. Ikemoto, S. Sato, H. Isobe, *Angew. Chem. Int. Ed.* **2020**, *59*, 6567–6571.
- [15] T. A. Schaub, E. A. Prantl, J. Kohn, M. Bursch, C. R. Marshall, E. J. Leonhardt, T. C. Lovell, L. N. Zakharov, C. K. Brozek, S. R. Waldvogel, S. Grimme, R. Jasti, *J. Am. Chem. Soc.* **2020**, *142*, 8763–8775.
- [16] Y. Ishigaki, T. Shimajiri, T. Takeda, R. Katoono, T. Suzuki, *Chem* **2018**, *4*, 795–806.
- [17] J. Luo, K. Song, F. L. Gu, Q. Miao, *Chem. Sci.* **2011**, *2*, 2029–2034.
- [18] Y. Ishigaki, Y. Hayashi, T. Suzuki, *J. Am. Chem. Soc.* **2019**, *141*, 18293–18300.
- [19] M. Pillekamp, W. Alachraf, I. M. Oppel, G. Dyker, *J. Org. Chem.* **2009**, *74*, 8355–8358.
- [20] B. L. Feringa, *J. Org. Chem.* **2007**, *72*, 6635–6652.
- [21] M. Irie, T. Fukaminato, K. Matsuda, S. Kobatake, *Chem. Rev.* **2014**, *114*, 12174–12277.
- [22] V. García-López, D. Liu, J. M. Tour, *Chem. Rev.* **2020**, *120*, 79–124.
- [23] M. Baroncini, S. Silvi, A. Credi, *Chem. Rev.* **2020**, *120*, 200–268.

- [24] P. Ravat, T. Šolomek, D. Häussinger, O. Blacque, M. Juriček, *J. Am. Chem. Soc.* **2018**, *140*, 10839–10847.
- [25] C. L. Fleming, S. Li, M. Grøtli, J. Andréasson, *J. Am. Chem. Soc.* **2018**, *140*, 14069–14072.
- [26] T. Yang, Y. Wang, X. Liu, G. Li, W. Che, D. Zhu, Z. Su, M. R. Bryce, *Chem. Commun.* **2019**, *55*, 14582–14585.
- [27] P. Lentès, E. Stadler, F. Röhricht, A. Brahms, J. Gröbner, F. D. Sönnichsen, G. Gescheidt, R. Herges, *J. Am. Chem. Soc.* **2019**, *141*, 13592–13600.
- [28] N.-Y. Li, J.-M. Chen, X.-Y. Tang, G.-P. Zhang, D. Liu, *Chem. Commun.* **2020**, *56*, 1984–1987.
- [29] K. Novak, V. Enkelmann, G. Wegner, K. B. Wagener, *Angew. Chem. Int. Ed. Engl.* **1993**, *32*, 1614–1616.
- [30] G. K. Kole, T. Kojima, M. Kawano, J. J. Vittal, *Angew. Chem. Int. Ed.* **2014**, *53*, 2143–2146.
- [31] N. Y. Li, D. Liu, B. F. Abrahams, J. P. Lang, *Chem. Commun.* **2018**, *54*, 5831–5834.
- [32] G. Pahari, B. Bhattacharya, C. M. Reddy, D. Ghoshal, *Chem. Commun.* **2019**, *55*, 12515–12518.
- [33] I. E. Claassens, L. J. Barbour, D. A. Haynes, *J. Am. Chem. Soc.* **2019**, *141*, 11425–11429.
- [34] J. Zhang, J. Li, X. Feng, M. Kong, Z.-B. Hu, Y.-X. Zheng, Y. Song, *Chem. Commun.* **2019**, *55*, 12873–12876.
- [35] M. W. Wong, *Chem. Phys. Lett.* **1996**, *256*, 391–399.
- [36] T. Suzuki, E. Ohta, H. Kawai, K. Fujiwara, T. Fukushima, *Synlett* **2007**, 851–869.
- [37] T. Suzuki, H. Tamaoki, J. Nishida, H. Higuchi, T. Iwai, Y. Ishigaki, K. Hanada, R. Katoono, H. Kawai, K. Fujiwara, T. Fukushima, *Organic Redox Systems: Synthesis, Properties, and Applications*, Wiley, Hoboken, Chap. 2, Pp. 13-37, **2015**.
- [38] T. Suzuki, J. Nishida, T. Tsuji, *Angew. Chem. Int. Ed. Engl.* **1997**, *36*, 1329–1331.
- [39] T. Suzuki, J. Nishida, T. Tsuji, *Chem. Commun.* **1998**, 2193–2194.
- [40] T. Suzuki, K. Ono, J. Nishida, H. Takahashi, T. Tsuji, *J. Org. Chem.* **2000**, *65*, 4944–4948.
- [41] Y. Ishigaki, Y. Hayashi, K. Sugawara, T. Shimajiri, W. Nojo, R. Katoono, T. Suzuki, *Molecules* **2017**, *22*, 1900.
- [42] T. Suzuki, Y. Ishigaki, T. Iwai, H. Kawai, K. Fujiwara, H. Ikeda, Y. Kano, K. Mizuno, *Chem. - A Eur. J.* **2009**, *15*, 9434–9441.
- [43] R. Hoffmann, *Acc. Chem. Res.* **1971**, *4*, 1–9.
- [44] K. Suzuki, A. Kobayashi, S. Kaneko, K. Takehira, T. Yoshihara, H. Ishida, Y. Shiina, S. Oishi, S. Tobita, *Phys. Chem. Chem. Phys.* **2009**, *11*, 9850.
- [45] J. M. Frisch, W. G. Trucks, B. H. Schlegel, E. G. Scuseria, A. M. Robb, R. J. Cheeseman, G. Scalmani, V. Barone, A. G. Petersson, H. Nakatsuji, X. Li, M. Caricato, V. A. Marenich, J. Bloino, G. B. Janesko, R. Gomperts, B. Mennucci, P. H. Hratchian, V. J. Ortiz, F. A. Izmaylov, L. J. Sonnenberg, D. Williams-Young, F. Ding, F. Lipparini, F. Egidi, J. Goings, B. Peng, A. Petrone, T. Henderson, D. Ranasinghe, G. V. Zakrzewski, J. Gao, N. Rega, G. Zheng, W. Liang,

- M. Hada, M. Ehara, K. Toyota, R. Fukuda, J. Hasegawa, M. Ishida, T. Nakajima, Y. Honda, O. Kitao, H. Nakai, T. Vreven, K. Throssell, A. J. Montgomery, Jr., E. J. Peralta, F. Ogliaro, J. M. Bearpark, J. J. Heyd, N. E. Brothers, N. K. Kudin, N. V. Staroverov, A. T. Keith, R. Kobayashi, J. Normand, K. Raghavachari, P. A. Rendell, C. J. Burant, S. S. Iyengar, J. Tomasi, M. Cossi, M. J. Millam, M. Klene, C. Adamo, R. Cammi, W. J. Ochterski, L. R. Martin, K. Morokuma, O. Farkas, B. J. Foresman, J. D. Fox, **2019**, Gaussian, Inc., Wallingford CT.
- [46] T. Lu, F. Chen, *J. Comput. Chem.* **2012**, *33*, 580–592.
- [47] E. D. Glendening, J. K. Badenhoop, A. E. Reed, J. E. Carpenter, J. A. Bohmann, C. M. Morales, P. Karafiloglou, C. R. Landis, F. Weinhold, **2018**, Theoretical Chemistry Institute, University of Wisconsin, Madison, WI.
- [48] O. V. Dolomanov, L. J. Bourhis, R. J. Gildea, J. A. K. Howard, H. Puschmann, *J. Appl. Crystallogr.* **2009**, *42*, 339–341.

Acknowledgement

This work has been carried out under the direction of Associate Professor Dr. Yusuke Ishigaki (Department of Chemistry, Faculty of Science, Hokkaido University). The author pays his heartfelt respects and gratitude to Associate Professor Ishigaki for his consistent guidance, suggestion, valuable discussions, encouragement, and so much help throughout the course of this work.

The author would like to express the deepest appreciation to Professor Dr. Takanori Suzuki (Department of Chemistry, Faculty of Science, Hokkaido University) for his kind guidance, valuable discussions and so much help throughout the course of this work. He taught the author the basics of the way to study

The author deeply grateful to Assistant Professor Dr. Ryo Katoono (Department of Chemistry, Faculty of Science, Hokkaido University) for his kind guidance, valuable discussion and so much help throughout the course of this work.

The author would like to thank Prof. Dr. Tetsuya Taketsugu, Prof. Dr. Keiji Tanino, Prof. Dr. Takeshi Ohkuma for their valuable suggestions and discussions.

The author expresses sincere thanks to Dr. Yasuto Uchimura and Dr. Yuto Sakano for their guidance and valuable discussions throughout the course of this work.

The author expresses sincere thanks to Dr. Yu Ozawa, Dr. Rina Takahashi and Dr. Kanami Sugiyama for their valuable discussions throughout the course of this work.

The author is really thankful to Dr. Eri Fukushi and Mr. Yusuke Takada (GC-MS & NMR Laboratory, Graduate School of Agriculture, Hokkaido University) for the measurement of mass.

The author wish to express special thanks to Prof. Dr. G. Dan Pantoş and all the members of his laboratory for their hospitable support, heartfelt guidance and valuable suggestions during my stay in Bath, UK.

The author gives a special thanks to Mr. Yuki Saito, Mr. Satoshi Okamoto, Dr. Wataru Nojo, Dr. Yuse Kuriyama, Mr. Keisuke Sugimoto, Mr. Kazuki Sakamoto and other members in Suzuki Laboratory from the bottom of his heart for their valuable discussions and giving his invaluable time.

The author is in acknowledgement of Research Fellowship of the Japan Society for the Promotion of Science (JSPS) for Young Scientists for Financial Support.

Finally, the author would like to express his deep, sincere and endless gratitude to his family, Yoshifumi Shimajiri, Michiyo Shimajiri and Kentaro Shimajiri for their continuous help and encouragement.

本研究にあたり、多くの先生方および友人の皆様に支えられ、有機化学第一研究室にて、化学を楽しむ機会と環境を授かりましたことに深く感謝します。

最後に、28年間私を育て、温かく見守り、支えてくれた家族に心から感謝します。

Takuya Shimajiri

Graduate School of Chemical Science and Engineering

Hokkaido University

2022

